

# Habilitationsschrift

## 3D-techniques in Materials Science

Eingereicht von Dipl.-Ing. Dr. mont. Jürgen Stampfl  
and der Fakultät für Maschinenbau  
der TU Wien  
zum Zwecke der Erlangung der Lehrbefugnis  
für das Fach Werkstoffwissenschaften

Wien, im März 2004

---

# Contents

<b>1</b>	<b>Preface</b>	<b>1</b>
1.1	Contributions of the author . . . . .	1
1.2	Achievements of the habilitation . . . . .	2
<b>I</b>	<b>Introduction</b>	<b>5</b>
<b>2</b>	<b>3D-scanning</b>	<b>7</b>
2.1	Stereoscopic electron microscopy . . . . .	7
2.1.1	Principle . . . . .	7
2.1.2	Image processing . . . . .	8
2.2	3D scanning in fracture mechanics . . . . .	10
2.3	Orientation image microscopy . . . . .	11
2.4	References . . . . .	11
<b>3</b>	<b>3D-shaping</b>	<b>15</b>
3.1	Stereolithography . . . . .	15
3.1.1	Stereolithography for microsystems . . . . .	18
3.1.1.1	Systems based on pixel arrays (DLP - digital light processing) . . . . .	19
3.1.1.2	Miniaturized SLA systems . . . . .	21
3.1.1.3	Two-photon processes . . . . .	22
3.1.2	Materials for stereolithography . . . . .	23
3.1.3	Objet Quadra . . . . .	25

3.2	Selective Laser Sintering (SLS) . . . . .	25
3.3	3D Printing . . . . .	30
3.4	Systems based on the deposition of thermoplastics . . . . .	31
3.4.1	Fused Deposition Modeling (FDM) . . . . .	31
3.4.2	ModelMaker Series . . . . .	32
3.4.3	MultiJet Modeling . . . . .	33
3.5	CNC Machining, Shape deposition Manufacturing . . . . .	33
3.6	Laminated Object Manufacturing (LOM) . . . . .	36
3.7	System selection . . . . .	37
3.8	References . . . . .	41
<b>4</b>	<b>RP of cellular solids</b>	<b>47</b>
4.1	Cellular structures for photonic crystals . . . . .	47
4.2	Cellular materials for biomedical applications . . . . .	48
4.2.1	Requirements for RP processes . . . . .	48
4.2.2	Applications . . . . .	52
4.3	References . . . . .	53
<b>II</b>	<b>Original papers</b>	<b>57</b>
<b>5</b>	<b>The Separation of the Fracture Energy in Metallic Materials</b>	<b>59</b>
	<i>International Journal of Fracture</i> 101(4):321-345, 2000	
5.1	Introduction . . . . .	60
5.2	A Brief Literature Survey . . . . .	61
5.2.1	The definition of the total crack growth resistance . . . . .	61
5.2.2	Some previous ideas on the separation of fracture energies . . . . .	62
5.3	The Total Plastic Strain Energy for Fracture and its Components . . . . .	64
5.3.1	The different plastic strain energy terms . . . . .	64

5.3.2	A general outline for determining the energy terms . . . . .	64
5.4	Materials and Specimens . . . . .	65
5.5	An Indirect Procedure to Separate Fracture Energies . . . . .	66
5.5.1	Single specimen tests . . . . .	66
5.5.1.1	A single specimen technique for measuring the total crack growth resistance . . . . .	66
5.5.1.2	Test results of the plain-sided specimens . . . . .	67
5.5.1.3	Test results of the side-grooved specimens . . . . .	68
5.5.2	A multi-specimen test on the steel V-720 . . . . .	68
5.5.3	The influence of specimen thickness . . . . .	69
5.5.4	Fracture surface analysis on the steel A 905 . . . . .	72
5.5.5	The separation of the fracture energies . . . . .	72
5.5.5.1	General remarks . . . . .	72
5.5.5.2	Discussion of the results . . . . .	73
5.6	The Estimate of Fracture Energies from Fracture Surface Analyses . . . . .	76
5.6.1	Stereophotogrammetry . . . . .	76
5.6.2	The plane strain fracture surface energy . . . . .	76
5.6.3	The direct determination of $R_{\text{flat}}$ . . . . .	79
5.6.4	The determination of the local fracture toughness . . . . .	81
5.7	Final Discussion and Summary . . . . .	82
5.8	References . . . . .	83
5.9	Some Remarks on the Reversibility of Fracture Energies . . . . .	86
5.10	The Relation between R and COA . . . . .	86
<b>6</b>	<b>Electro-discharge machining of mesoscopic parts with electroplated copper and hot-pressed silver tungsten electrodes</b>	<b>89</b>
	<i>Journal of Micromechanics and Microengineering</i> , 10:1-6, 2000	
6.1	Introduction . . . . .	89
6.2	Preparation of silicon molds . . . . .	91

6.3	Electroplating . . . . .	92
6.4	Hot-pressing of metal powder . . . . .	93
6.5	Electro discharge machining . . . . .	96
6.6	Conclusions . . . . .	98
6.7	References . . . . .	98
<b>7</b>	<b>Rapid Prototyping and Manufacturing by Gelcasting of Metallic and Ceramic Slurries</b>	<b>101</b>
	<i>Materials Science and Engineering A334:187-192, 2002</i>	
7.1	Introduction . . . . .	101
7.2	Mold SDM . . . . .	102
7.3	Gelcasting . . . . .	102
7.3.1	Slurries . . . . .	103
7.3.2	Microstructure . . . . .	105
7.3.3	Micromachined molds . . . . .	106
7.4	Mechanical properties . . . . .	108
7.5	Conclusion . . . . .	110
7.6	References . . . . .	110
<b>8</b>	<b>Cellular solids beyond the apparent density - an experimental assessment of mechanical properties</b>	<b>113</b>
	<i>Advanced Engineering Materials, 6:134-138, 2004</i>	
8.1	Introduction . . . . .	113
8.2	Motivation . . . . .	115
8.3	Experimental Method . . . . .	115
8.4	Discussion . . . . .	119
8.5	References . . . . .	120
<b>9</b>	<b>Water soluble, photocurable resins for rapid prototyping applications</b>	<b>123</b>
9.1	Introduction . . . . .	123

---

9.2	Moulding techniques . . . . .	125
9.3	Sacrificial photopolymers . . . . .	126
9.4	Conclusion . . . . .	129
9.5	References . . . . .	130
<b>10</b>	<b>Abbreviations</b>	<b>131</b>
	<b>Index</b>	<b>133</b>



This text is a collection of 5 reviewed publications, accompanied by 3 chapters describing the utilized techniques and giving an overview of envisaged applications: Chap. 2 (page 7) is a brief summary about stereoscopic techniques in scanning electron microscopy. Chap. 3 (page 15) is a review about commercially available RP (rapid prototyping) processes. Special emphasis has been put on collecting available technical specifications in order to set up system selection charts (see Sec. 3.7).

Chap. 4 (page 47) is mainly a literature review of the use of RP to fabricate cellular structures for biomedical and opto-electronical applications.

## 1.1 Contributions of the author

---

The remaining chapters are reprints of original publications. These publications are the output of teams which the author has worked with. The individual contributions to these publications need to be clarified:

- **J. Stampfl**, O. Kolednik, The separation of the fracture energy in metallic materials, *International Journal of Fracture*, 101(4).321-345, 2000  
(Chapter 5 on page 59):  
The first author has done nearly all measurements presented in this work, parts of the text were written by him.
- **J. Stampfl**, R. Leitgeb, Y.-L- Chen, F. Prinz, Electro-discharge machining of mesoscopic parts with electroplated copper and hot-pressed silver tungsten electrodes, *Journal of Micromechanics and Microengineering*, 10:1-6, 2000  
(Chapter 6 on page 89):  
The text was mainly written by J. Stampfl, and he also provided a large fraction of the experimental data.
- **J. Stampfl**, H.C. Liu, S.W. Nam, K. Sakamoto, H. Tsuru, S. Kang, A. G. Cooper, A. Nickel, F. B. Prinz, Rapid prototyping and manufacturing by gelcasting of metallic and ceramic slurries, *Materials Science and Engineering A334*:187-192, 2002  
(Chapter 7 on page 101):

J. Stampfl has done significant parts of the experimental work presented in this publication. The text was mostly written by him.

- A.Wöß, **J. Stampfl**, P. Fratzl, Cellular solids beyond the apparent density - an experimental assessment of mechanical properties, *Adv. Engng. Mat*, 6:134-138, 2004

(Chapter 8 on page 113):

J. Stampfl originated the project whose outcome is presented in this publication. He contributed parts of the text and of the experimental work.

- **J. Stampfl**, A. Wöß, S. Seidler, H. Fouad, A. Pisaipan, F. Schwager, R. Liska, Water soluble, photocurable resins for rapid prototyping applications, *Macromolecular Symposia*, in print 2004

(Chapter 9 on page 123):

The first author contributed the text related to rapid prototyping. The photocurable resins developed and described by LISKA and SCHWAGER served as input for fabricating RP parts. Some of the ideas which serve as basis for this work were originally developed during projects described in Chapter 7.

## 1.2 Achievements of the habilitation

---

The work whose outcome is presented in this habilitation is thematically aligned along the process chain depicted in Fig. 1.1, with a strong emphasis on using these techniques for applications in materials science. In early stages of the product development cycle, a mechanical engineer follows the route sketched in Fig. 1.1: Using **3D-scanning** or **CAD**-software, a computer model of the desired structure is made. This model serves as input for a rapid prototyping (RP) system which is able to fabricate a physical part (**3D-shaping**). In many cases the RP-machine is not able to directly shape the desired material. That is why an additional process step (**3D-copying**) might be necessary in order to obtain the final part in a more advanced target material. This process chain is well established in mechanical engineering. *The main goal of this habilitation is to adapt these processes to gain a deeper understanding of advanced materials.*

- **3D-scanning**: Scanning electron microscopy (SEM) is a commonly used standard technique in materials science which is used to gain topographical, structural and chemical information of a wide range of materials. Using stereoscopic techniques in combination with image processing, a SEM can easily be modified to gain quantitative information about topography and/or deformation properties of a specific specimen. In a cooperative effort between materials and computer scientists, a system was developed which is able to deliver such 3D-information about (mostly metallic) samples. In Chap. 5 it is shown how such a system can be utilized in fracture mechanics. The main goal of this work was to measure fracture energies locally (analyzing the local deformations on the fracture surface) and compare these values with the globally dissipated energy. In Tab. 5.1 on page 75 it is shown, that the globally measured value  $W_{pl,tot}$  corresponds well with the sum of the local values  $\sum W_{pl,est}$ .

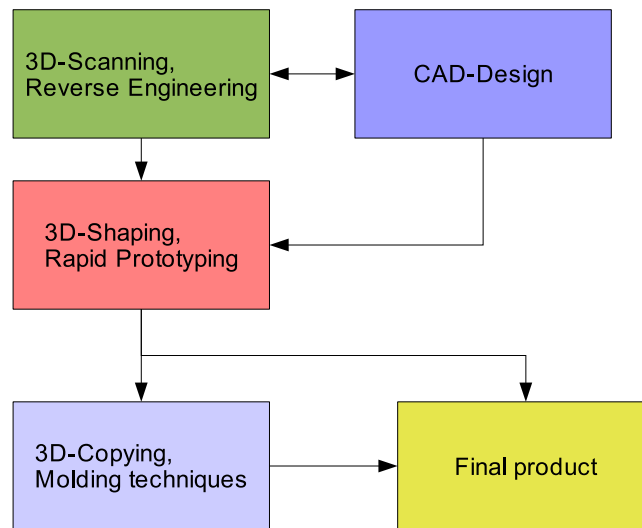


**Figure 1.1:** Process chain for using 3D-techniques in engineering.

- **3D-shaping:** RP is currently mostly used for fabricating physical prototypes in the product development cycle. In this field, RP is competing with traditional manufacturing methods like CNC machining. Parameters like shape accuracy and surface quality are the most critical in these types of applications. Besides these already traditional approaches for RP, there is a growing number of applications (for instance in biomedical engineering) where parts with very high geometric complexity are required. Chap. 8 on page 113 gives an example of such applications: Cellular structures with defined internal as well as external geometry are impossible to fabricate with conventional manufacturing techniques. RP is a suitable manufacturing technique for such structures, and their investigation will increase the understanding of functional as well as structural properties of such material-structures.

Besides increasing shape-complexity, there is a growing demand for parts shaped on the micro-scale. Chap. 6 on page 89 gives an example of how microscopic parts can be shaped with lithographic techniques in combination with electroplating and hot-pressing. The target applications for such techniques lie mainly in the field of tooling.

- **3D-copying:** Advanced moulding techniques allow the fabrication of prototypes in a wide variety of different materials. Materials which cannot be shaped directly by RP are only accessible via moulding. In Chap. 7 on page 101 it is shown how engineering ceramics like silicon nitride can be shaped using RP. In this case high-temperature ceramics were required, and the focus of the investigations was on obtaining good mechanical properties as well as excellent shape accuracy. Chap. 9 on page 123 describes, how water soluble resins can be shaped with stereolithography. Such water soluble parts can serve as sacrificial moulds for thermally sensitive materials, which are, for instance, required in biomedical applications.



# **Part I**

## **Introduction**



3D-scanning is a widely used technique in mechanical engineering. Main applications include geometric quality control and reverse engineering of physical models which need to be digitized for further processing of the digital model. 3D-scanning applications in materials science are usually based on microscopic techniques, and the available methods for revealing topographical information on the microscopic level can be grouped in two categories:

- **Tactile** methods like scanning probe or scanning tunnel microscopy examine the specimen using a sharp tip. From the behaviour of the tip (tunneling current, deflection, ...) the topography of the sample can be reconstructed. Besides studying the topography, it is also possible to gain information about the magnetic and optical properties of the examined surface [2.1]. The big advantage of scanning probe techniques is their unsurpassed lateral and vertical resolution, reaching into atomic scales. Problems arise if the surface is very rough or contains undercut regions, since the tip has to reach all regions of interest.
- **Non-tactile** methods use an optical or electron-optical beam to probe the specimen surface. Among the optical methods confocal scanning microscopy [2.2, 2.3] and white-light-interference microscopy [2.4, 2.5] have found widespread applications. The lateral resolution for both methods is limited by the utilized wavelength and can be estimated to be larger than 300 nm. The vertical resolution limit is around 200 nm for confocal and <10 nm for white light interference microscopy. SEM systems can also be adapted to analyze topographical information, and mainly stereoscopic techniques are used in this context.

The following section is a modified version of the review on stereoscopic SEM-techniques published in [2.6].

## 2.1 Stereoscopic electron microscopy

---

### 2.1.1 Principle

In conventional scanning electron microscopy (SEM) the information about the topography of the specimen is revealed through the variation of shading which is caused

mainly by the variation of the surface normal relative to the position of the detector and the incident electron beam. The three-dimensional impression of SEM pictures gives a qualitative information about the surface topography. In order to get a quantitative topographic information, stereoscopic techniques have been developed [2.7–2.10]. Stereoscopic techniques are based on taking at least two images from different view-points. Depending on the height of the observed structure (see Fig. 2.1), the projection of an object point  $P_1$  (respectively  $P_2$ ) on the image plane moves a certain distance during tilting. This distance (parallax) is then a measure for the original height of the object. The challenge is to identify so called homologue points in the two image pairs. Homologue points are the projection of the same object point in the two images.

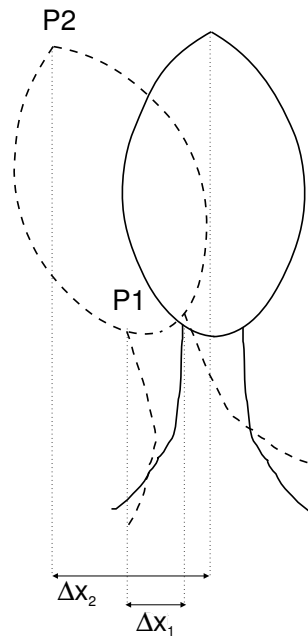


**Figure 2.1:** Tilting of a specimen causes parallaxes  $\Delta X_1$  and  $\Delta X_2$  depending on the height of the points  $P_1$  and  $P_2$ .

The equipment which was used for the evaluation of stereoscopic image pairs was initially comparable to systems which were utilized in remote sensing. The fact that the manual or semi-automatic analysis of these image pairs turned out to be very labor-intensive, prevented the use of such techniques for investigations on a routine basis.

### 2.1.2 Image processing

With the development of systems based on image processing, the evaluation of stereo-images could be automated [2.11–2.14]. With these image processing capabilities, topographic information for several thousand points per image can be generated.

After taking an initial image at an angle of  $0^\circ$  (Fig. 2.2 a), the specimen is tilted by approximately  $10^\circ$  (Fig. 2.2 b) and another image is taken. (The tilt angle is chosen according to the elevation differences on the surface. The higher the height differences are in relation to the observed specimen width, the lower the tilt angle should be.) The

analyzing software marks homologue points in the digital images by matching the gray values or image features between rectangular sub-regions in the two images. 20,000 to 30,000 homologue points are commonly found in conventional SEM images consisting of 1,024x768 pixels.

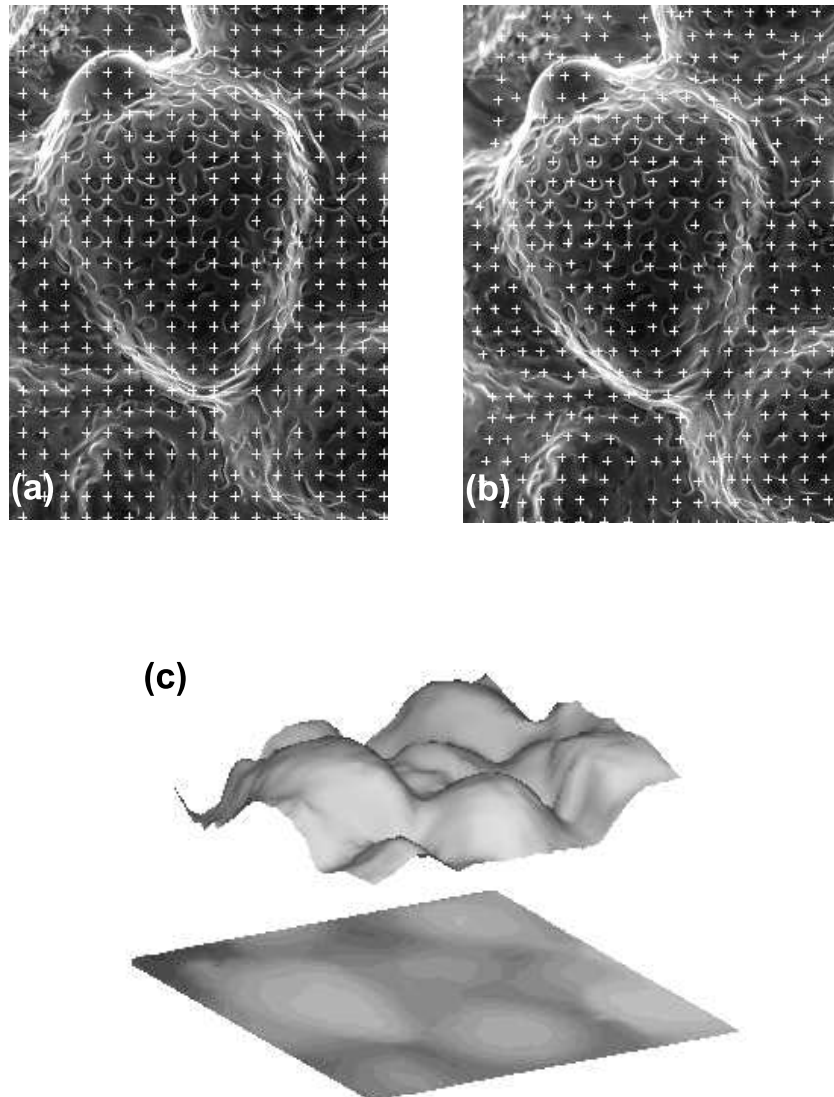


**Figure 2.2:** After taking two SEM images at a tilt angle of  $0^\circ$  (a) and  $10^\circ$  (b), homologue points in each image are marked with a cross. From the parallax between these points, a digital elevation model (c) of the surface can be calculated.

In Fig. 2.2 it can be seen that a regular grid of points in image (a) is no longer a regular grid (b) after the object has been tilted. From this deviation (or parallax) between the two images the topographic information can be calculated. The accuracy of the digital elevation model depends on the quality of the images, the accuracy of the image parameters (tilt angle, magnification), and the accuracy of matching algorithm. A test revealed a matching accuracy of  $\pm 0.05$  pixels [2.15].

As will be shown in the following section, a detailed information about the three-dimensional surface topography leads to numerous applications in materials science.

## 2.2 3D scanning in fracture mechanics

---

SEM-stereophotogrammetry is a very suitable method for quantitative analyses of fracture surfaces [2.16, 2.17]. The main advantages compared to other available methods are the high accuracy at arbitrary magnifications, the high depth of focus of the scanning electron microscope (SEM), and the possibility to find corresponding regions on both fracture surfaces which is important for many applications.

Local features of the fracture surface can be analyzed using SEM, and the locally measured data can be correlated to the global crack growth behavior of the specimen. For instance, from the striation width [2.18] the crack growth rate in fatigue can be determined; the dimple height of microductile fracture surfaces can be used to estimate the fracture toughness [2.19, 2.20]. Moreover, different roughness parameters or the fractal dimension have been determined to quantify the nature of fracture surfaces [2.16, 2.17, 2.21].

In Sec. 5.6 on page 76 it is shown, how stereoscopic SEM in combination with automated image processing can be used to measure dissipated fracture energy on a local level. The principal idea behind this evaluation can be described as follows:

The total plastic energy  $W_{pl,tot}$  dissipated by a fracture mechanics specimen can be divided into the following components (see Eq. 5.2 on page 64):

$$W_{pl,tot} = W_{pl,i} + W_{pl,flat} + W_{pl,slant} + W_{pl,lat}, \quad (2.1)$$

where

$$W_{pl,flat} = W_{pl,sub} + W_{pl,surf}. \quad (2.2)$$

$W_{pl,tot}$ , the sum of all local contributions, is obtained as result of the fracture mechanics test. The experimental data for the local analysis of fracture energies are fracture mechanical data on one side and topographical information (obtained from stereoscopic SEM images) on the other side.  $W_{pl,i}$  is the energy consumed until fracture initiation and can be obtained from the topography of the fracture surface by analyzing the crack opening displacement  $COD_i$  (see Sec. 5.10 on page 86).  $W_{pl,sub}$ , the energy dissipated under the fracture surface, can be obtained from measuring the crack opening angle  $COA$  (see Sec. 5.6.3 on page 79) and  $W_{pl,surf}$  (the energy required for plastically deforming the fracture surface) can be measured from analyzing void maps of the fracture surface (see Sec. 5.6.2 on page 76). This means that  $W_{pl,flat}$  (the energy stored in mid-section regions of the fracture specimen) is accessible by analyzing the fracture surface topography. The remaining local terms in Eq. 2.1 can be obtained from analyzing the results of the fracture mechanical test in more detail (e.g. by comparing side-grooved and plain-sided specimens, or by comparing specimens with varying thickness).

In order to obtain reliable results about the local plastic deformations occurring during

fracture, it is always necessary to examine both halves of the fractured sample. The knowledge about the topography of one specimen half is not enough to measure local deformations since a “mountain” on one specimen half can be compensated by a “valley” on the other half. In Fig. 5.8 on page 78 two corresponding fracture surfaces are depicted which serve as basis for evaluating fracture mechanical parameters like the crack tip opening displacement *CTOD*.

## 2.3 Orientation image microscopy

---

From electron backscatter diffraction (EBSD) patterns, the crystal structure and orientation can be deduced [2.22, 2.23]. The accuracy of the orientation measurement is better than  $1^\circ$ , and the spatial resolution is given as  $0.2\ \mu\text{m}$ . The information about the local crystal orientation can be used to explore the orientation relationship between neighboring grains, or between the metal matrix and second phases [2.24].

A technique called the crystallographic fractometry was developed for the investigation of cleavage fracture surfaces [2.25]: Stereophotogrammetry is used to measure the orientation of a cleavage plane in space; electron backscatter diffraction yields the crystallographic orientation of the considered crystal. The combination of the two results leads to the crystallographic indices of the cleavage plane and the crystallographic indices of certain directions on the plane [2.25–2.27].

Orientation imaging microscopy (OIM) permits both the automatic positioning of the electron beam in the SEM and the automatic analysis of the diffraction pattern [2.28, 2.29]. Approximately 3,000 orientation measurements can be analyzed per hour; for example, 12 hours are necessary for analyzing an area of  $200 \times 200\ \mu\text{m}$  in steps of  $1\ \mu\text{m}$ . Orientation image microscopy (OIM) analyses are applied in [2.30, 2.31] to measure the crystallographic grain orientation before and after the deformation steps within the same area where the local strains have been determined. For each grain, the local in-plane strains and the local rotation angle of the crystal are combined to estimate the slip systems that are locally active. In addition to the automatic local deformation measurements, OIM is applied for an effective characterization of the evolution of the material microstructure at the same deformation stages. The combination yields an almost complete metal plasticity description of the deformation process.

## 2.4 References

---

- 2.1 R. Wiesendanger. *Scanning Probe Microscopy and Spectroscopy*. Cambridge University Press, Cambridge, 1994.
- 2.2 U. Wendt, H. Blumenauer, and J. Ude. Konfokale Laserrastermikroskopie zur Fraktometrie von Feinkornbaustählen. In M. Kurz and M. Pohl, editors, *Prakt. Metallogr. Sonderbd*, volume 27, pages 185–188, 1995.
- 2.3 U. Wendt and M. Kästner. Konfokale Laserrastermikroskopie und Topometrie. In H. Vethers, editor, *Rastermikroskopie in der Materialprüfung*, Vorträge der 17.

- Tagung, pages 173–178. DVM, 1996.
- 2.4 J.C. Wyant. White light interferometry. In *Holography: A Tribute to Yuri Denisyuk and Emmet Leith*, volume 4737 of *Proceedings of SPIE - The International Society for Optical Engineering*, pages 98–107. SPIE, 2002.
- 2.5 M. Maurer and F. Mücklich. Quantifizierung von lokalem Materialabtrag mittels Weißlichtinterferometrie. *Prakt. Met. Sonderband*, 30:287–292, 1999.
- 2.6 J. Stampfl, A. Wöß, O. Kolednik, and P. Fratzl. Object reconstruction and object construction: applications in materials science. *Recent Res. Devel. Applied Phys*, 5:89–106, 2002.
- 2.7 M.v. Ardenne. Über ein Universal-Elektronenmikroskop für Hellfeld-, Dunkelfeld und Stereobildbetrieb. *Z. Physik*, 115:339–368, 1940.
- 2.8 J. G. Helmcke. Theorie und Praxis der elektronenmikroskopischen Stereoaufnahmen - Methoden zur Tiefenausmessung elektronenmikroskopischer Objekte und Forderungen an ein photogrammetrisches Auswertegerät. *Optik*, 12:253–273, 1955.
- 2.9 G. S. Lane. The application of stereographic techniques to the scanning electron microscope. *J. Scientific Instruments (J. Phys. E)*, 2(2):565–569, 1969.
- 2.10 A. Boyde. Quantitative photogrammetric analysis and qualitative stereoscopic analysis of SEM images. *J. Microscopy*, 98(3):452–471, 1973.
- 2.11 T. Takano, H. Sumiyoshi, and C. Masuda. Algorithm for three-dimensional analysis of cleavage facets and its application for brittle fracture surface of steels. *ISIJ International*, 30:552–558, 1990.
- 2.12 J. Stampfl, S. Scherer, M. Gruber, and O. Kolednik. Reconstruction of surface topographies by scanning electron microscopy for application in fracture research. *Applied Physics A*, A63:341–346, 1996.
- 2.13 J. Stampfl, S. Scherer, M. Berchthaler, M. Gruber, and O. Kolednik. Determination of the fracture toughness by automatic image processing. *Int. J. Frac.*, 78:35–44, 1996.
- 2.14 S. Scherer and O. Kolednik. A new system for automatic surface analysis in SEM. *Microscopy and Analysis*, 70:15–17, 2001.
- 2.15 A. Tatschl and O. Kolednik. A new tool for the experimental characterization of micro-plasticity. *Materials Science and Engineering A*, 339(1-2):265–280, 2003.
- 2.16 H.E. Exner and M. Fripan. Quantitative assessment of three-dimensional roughness, anisotropy and angular distributions of fracture surfaces by stereometry. *Journal of Microscopy*, 139:161–178, 1985.
- 2.17 E.E. Underwood and K. Banerjee. Fractal analysis of fracture surfaces. In *Metals Handbook*, volume 12, pages 211–215. ASM International, Metals Park, Ohio, USA, 1987.

- 2.18 A.J. Krasowsky and V.A. Stepanenko. A quantitative stereoscopic fractographic study of the mechanism of fatigue crack propagation in steel. *International Journal of Fracture*, 15:203–215, 1979.
- 2.19 O. Kolednik. Ein Beitrag zur Stereophotogrammetrie mit dem Rasterelektronenmikroskop. *Praktische Metallographie*, 18:562–573, 1981.
- 2.20 O. Kolednik and H.P. Stüwe. Abschätzung der Reißfähigkeit eines duktilen Werkstoffes aus der Gestalt der Bruchfläche. *Zeitschrift für Metallkunde*, 73:219–223, 1982.
- 2.21 O. Kolednik, S. Scherer, P. Schwarzböck, and P. Werth. Quantitative fractography by means of a new digital image analysis system. In M. Fuentes and M. Elices, editors, *Fracture Mechanics: Applications and Challenges*, Proc. of ECF 13, page Paper 1U.60. Elsevier, Amsterdam, 2000.
- 2.22 D.J. Dingley, M. Longden, J. Weinbren, and J. Alderman. On-line analysis of electron backscatter diffraction patterns, texture analysis of polysilicon. *Scanning Microscopy*, 1:451–456, 1987.
- 2.23 D.J. Dingley and V. Randle. Microtexture determination by electron backscatter diffraction. *Journal of Materials Science*, 27:4545–4566, 1992.
- 2.24 V. Randle and D. Dingley. Measurement of boundary plane inclination in a scanning electron microscope. *Scripta metallurgica*, 23:1565–1570, 1989.
- 2.25 C.O.A. Semprinoschnig, J. Stampfl, R. Pippan, and O. Kolednik. A new powerful tool for surveying cleavage fracture surfaces. *Fatigue & Fracture of Engineering Materials and Structures*, 20:1541–1550, 1997.
- 2.26 T. Hebesberger, R. Pippan, O. Kolednik, C.O.A. Semprinoschnig, and H. Clemens. Crystallographic fractometry: A new method of fracture surface analysis applied on TiAl fracture surfaces. *Praktische Metallographie*, 37(6):301–314, 2001.
- 2.27 P.A. Davies and V. Randle. Combined application of electron backscatter diffraction and stereo-photogrammetry in fractography studies. *J. Microsc. - Oxford*, 204:29–38, 2001.
- 2.28 K. Kunze, S.I. Wright, B.L. Adams, and D.J. Dingley. Advances in automatic EBSP single orientation measurements. *Textures and Microstructures*, 20:41–54, 1993.
- 2.29 B.L. Adams, S.I. Wright, and K. Kunze. Orientation imaging microscopy: The emergence of a new microscopy. *Metallurgical Transactions*, 24a:819–831, 1993.
- 2.30 A. Tatschl, C.Motz, R.Pippan, and O.Kolednik. The characterization of crystal plasticity by orientation image microscopy and local deformation experiments. In B. Jouffrey and J. Svejcar, editors, *Microstructural Investigation and Analysis*, volume 4 of *Proc. EUROMAT*, pages 151–156. Wiley VCH Publisher, Weinheim, Germany, 2000.

- 2.31 A. Tatschl and O. Kolednik. On the experimental characterization of crystal plasticity in poly-crystals. *Materials Science and Engineering A*, 342(1-2):152–168, 2003.

---

In this section the most commonly used Rapid Prototyping techniques are described. The goal of this chapter is to give an overview of available processes. The advantages and drawbacks of the individual systems serve as basis for selecting the appropriate technique for the application described in Chap. 6 to 9.

A common characteristic of all currently available RP techniques is the fact that they are based on layered manufacturing: A part model is sliced into manufacturable layers and by stacking up these layers automatically, a complex shape can be obtained. Most currently used RP systems are based on additive techniques (see Fig. 3.1). Additive techniques can further be subdivided regarding the feedstock material (liquid, powders, sheets) which is used for part deposition. In Fig. 3.1 a taxonomy of widely used RP techniques is depicted, adapted from classifications made by PHAM [3.1] and KRUTH [3.2].

### 3.1 Stereolithography

---

Stereolithography is historically the first RP technique which was commercially available. The technique in its current form was independently developed by teams in France [3.3], USA [3.4, 3.5] and Japan [3.6]. Stereolithography is currently the most widely used RP technique and has become a standard tool for industrial and medical prototyping. By solidifying a liquid photosensitive monomer with a laser or UV-light source a polymeric part is built up layer by layer [3.7, 3.8].

The working principle of the most commonly used systems is depicted in Fig. 3.2: A building platform is immersed in a tank filled with liquid photosensitive resin. By using a galvanic mirror system, a laser beam is projected onto selected regions of the resin-surface. Where the laser hits the resin, the monomer solidifies due to the photochemically induced reaction. After the laser beam has scanned all regions of the current layer which need to be solidified, the part is coated with a fresh layer of liquid resin. This is typically achieved by lowering the part and recoating the surface using a wiper blade. Commonly used layer thicknesses vary between 0.02 and 0.2 mm.

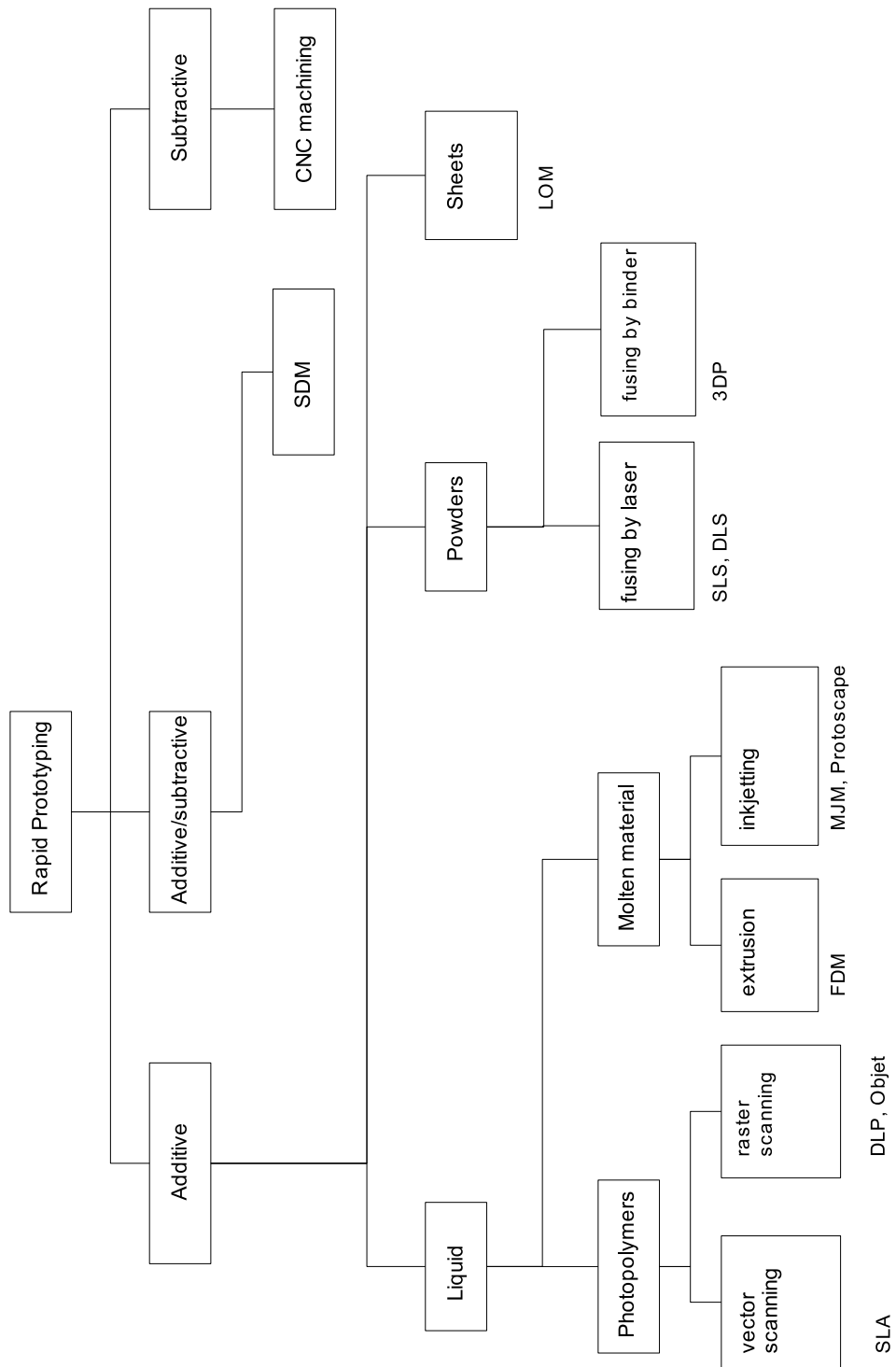


**Figure 3.1:** Classification RP processes after [3.1] and [3.2].

After the new layer of liquid resin has been formed, the above process is repeated until the part is complete. In order to achieve high build speeds and good surface quality, SLA machines use special exposure-strategies. Typically, the outer contours of the region which has to be solidified are exposed in one step ("borders"). In a following step the inner regions are exposed separately ("hatches"). When all layers have been

exposed, the part can be taken out of the build-chamber to remove remaining liquid resin and to prepare the part for necessary post-processing steps. In a first step the usually incompletely cured resin is thoroughly finish-cured by flood-exposing the part with UV light.

In a second step (which is only necessary for parts with higher quality requirements) the surface of the part is treated to remove the typical stair-steps originating from the layered manufacturing process. This can be achieved by sanding or grid-blasting the part. This step can be very time consuming since a smooth surface finish must be achieved without destroying the geometrical dimensions of the part by removing too much material. It is also possible to paint the SLA part. The applied paint will smoothen the surface and yield surfaces with high quality.

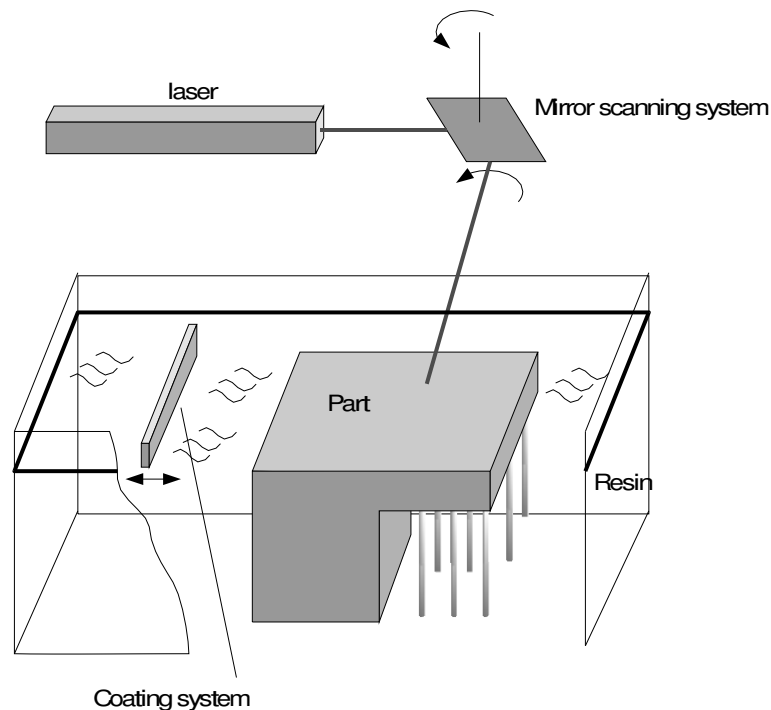


**Figure 3.2:** Principle of stereolithography.

The key advantages and drawbacks of stereolithography can be summarized as follows:

- SLA is currently the method with the highest geometric resolution and best surface quality.
- Recently developed resins allow the fabrication of parts with mechanical properties comparable to many engineering polymers.
- In cases where the SLA resins cannot fulfill the required mechanical or optical properties, the SLA part can be molded with a large number of molding techniques like investment casting or silicone molding.

There are also a number of drawbacks:

- Since the SLA part is immersed in a liquid resin during the fabrication process, support structures have to be printed for supporting undercut and island features. After the part is taken out of the machine, these support structures have to be removed manually usually leaving a surface finish inferior to unsupported surfaces.
- Since the monomer shrinks during polymerization, the build-up of internal stresses, which can lead to warpage later on, is possible. Due to the development of advanced resins and building-strategies this problem has been minimized in recent years.
- SLA can only process photopolymers or powder filled photopolymers. This clearly limits the number of available materials, and certain material groups (elastomers, metals, ..) can only be made accessible by appropriate molding techniques.

When SLA is used in combination with secondary molding processes, the SLA manufacturing strategy can be modified in order to achieve optimal results. If investment casting is chosen as secondary operation, the QuickCast process developed by 3D Systems can help to increase the compatibility between SLA and investment casting. In order to reduce the necessary resin and to improve the burnout-characteristics of the SLA part, the QuickCast process produces parts with a solid shell which is filled by a honeycomb structure inside. Some of the honeycomb walls are missing to help releasing the uncured resin. The honeycomb-walls fill roughly 15% of the overall part volume, thus reducing the amount of polymer which has to be burnt out after embedding the SLA part with ceramic slurry.

### 3.1.1 Stereolithography for microsystems

One of the most intriguing aspects of stereolithography is its potential to fabricate parts that are small enough for applications in MEMS (microelectromechanical systems). The shaping techniques which are currently used for the fabrication of MEMS [3.9–3.11] can achieve very small feature sizes, but the geometric complexity of the parts fabricated with these techniques is usually simple.

SLA parts like the one shown in Fig. 3.3 can expand the design space and free the MEMS engineer from currently existing manufacturing limitations. A fairly large number of research institutions is working on making SLA accessible for MEMS applications. The systems developed at these institutions are mainly based on the following principles [3.12, 3.13]:

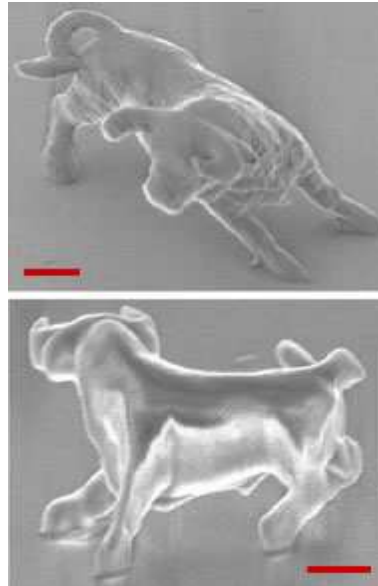


**Figure 3.3:** Bull fabricated with micro-stereolithography. The size-bar corresponds to  $2\ \mu\text{m}$ , from [3.14].

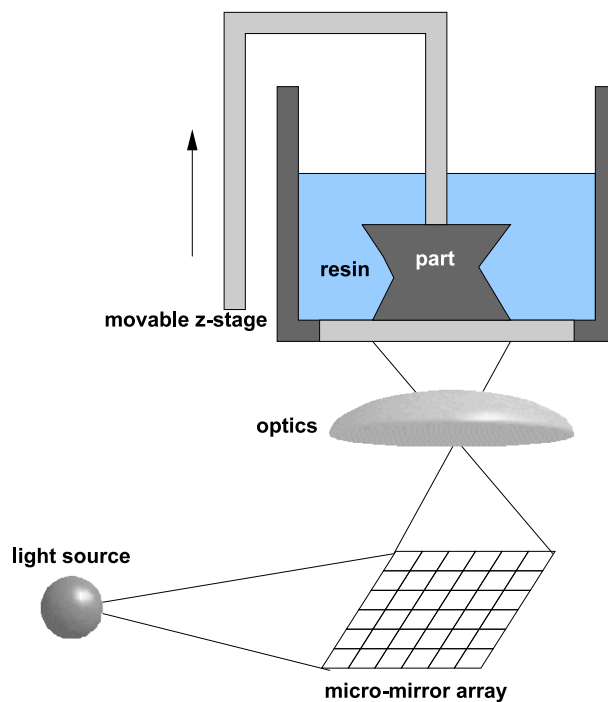


**Figure 3.4:** Working principle for RP systems based on digital micro-mirrors.

### 3.1.1.1 Systems based on pixel arrays (DLP - digital light processing)

Machines based on digital mirror devices (DMD) or dynamic mask generators have found widespread applications [3.15–3.18]. The common principle of these systems is depicted in Fig. 3.4: A digital mirror device or a dynamic LCD mask is illuminated by a non-coherent light beam. The pixels of the dynamic mask can be turned on and off

individually and by projecting the image of the mask onto a photo-sensitive resin one layer of the part that is to be fabricated is generated. After applying a next layer, this process is repeated until the part is complete.

This technique is interesting due to technical and economical reasons. By using commercially available dynamic masks (which are used in video projection systems) instead of an expensive laser the system costs can be kept low. These systems are also technically appealing since they can shape a complete layer with one exposure, using the parallel arrangement of individually accessible pixels on the array. Currently used systems have achieved resolutions in the  $xy$ -plane down to  $5 \mu\text{m}$  with a minimum layer thickness of  $10 \mu\text{m}$ .

The drawback of this method is the fact that currently available dynamic masks cannot operate at the short wavelengths which are used for conventional stereolithography. That means that new resins, especially developed for these processes, need to be utilized. Recently developed dynamic masks [3.19] can operate at shorter wavelengths, but these systems are not commercially available. Another drawback is the fact that the dynamic masks operate with a fixed number of pixels (e.g.  $1280 \times 1024$ ). This means that a higher feature resolution automatically means a smaller build volume.

Example parts which were made using SLA systems based on dynamic masks are shown in Fig. 3.5. This type of system was used for the fabrication of parts presented in Chap. 9.

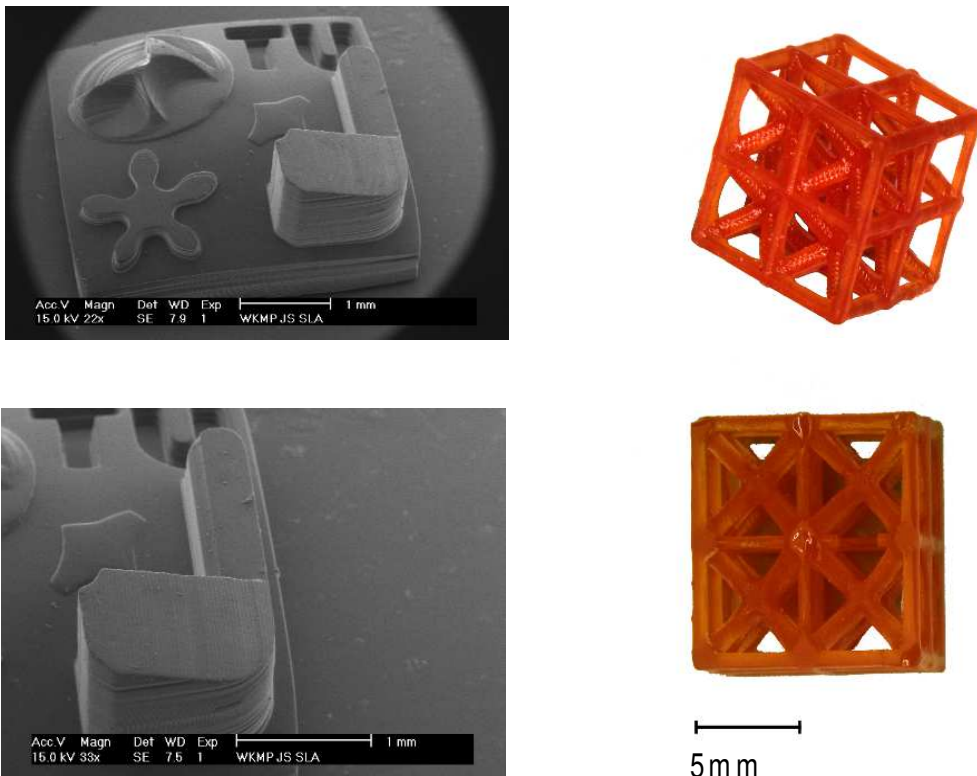


**Figure 3.5:** Parts fabricated with DLP (SLA systems using dynamical masks). The SEM-images on the left show the master pattern for a mold insert. The photographs on the right show a cellular solid

### 3.1.1.2 Miniaturized SLA systems

Several research groups [3.20–3.23] have modified the conventional, vector based SLA process in order to achieve significantly smaller feature sizes than commercially available SLA systems. 3D Systems also offers a system with reduced spot size (Viper si2, minimum spot size 0.075 mm) which is used for fabricating miniaturized parts.

The goal of these modifications is to reduce the beam diameter as far as possible in order to achieve small feature sizes. Furthermore the repeatability of the beam positioning system must be improved. Systems which use galvanometric mirrors have to fight a problem which is illustrated in Fig. 3.6: Since the focal length of the optical system in an SLA machine is constant, but the distance from the resin surface to the center of the galvanometric scanner is variable, the minimum waist of the laser beam is not always on the resin surface, thus limiting the overall feature resolution. An alternative to galvanometric scanning systems is the use of a fixed laser beam in combination with an xy-platform. This can improve the resolution, but will increase the necessary build time since the movement of the building platform cannot be as fast as a scanning laser beam.

A reduced spot size will increase the necessary build-time since the smaller spot has to make more scans to cover a certain area. It can therefore be expected that for practical purposes the spot size will remain in the range of several tens of microns.

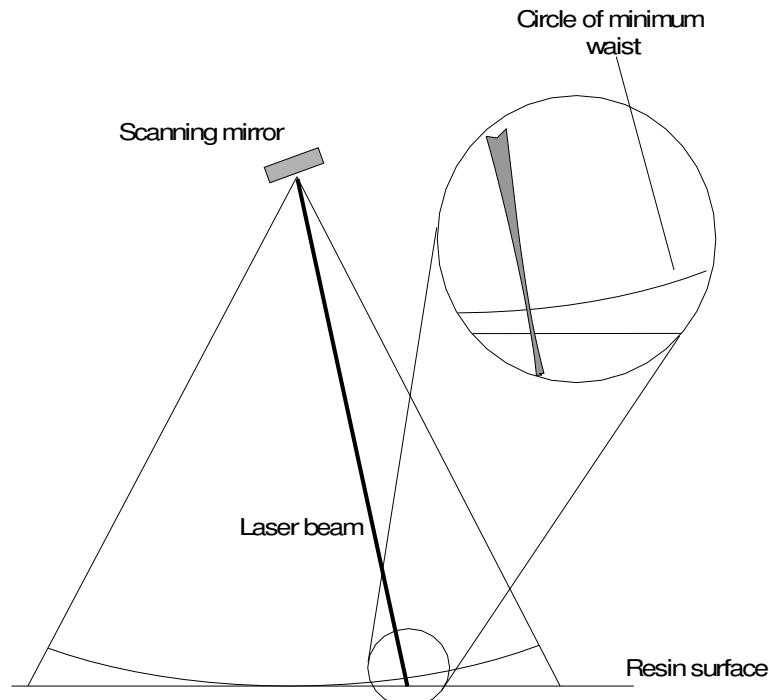


**Figure 3.6:** The minimum waist of the incident laser beam deflected by a galvanometric mirror intersects the flat resin surface only at certain positions, after [3.7].

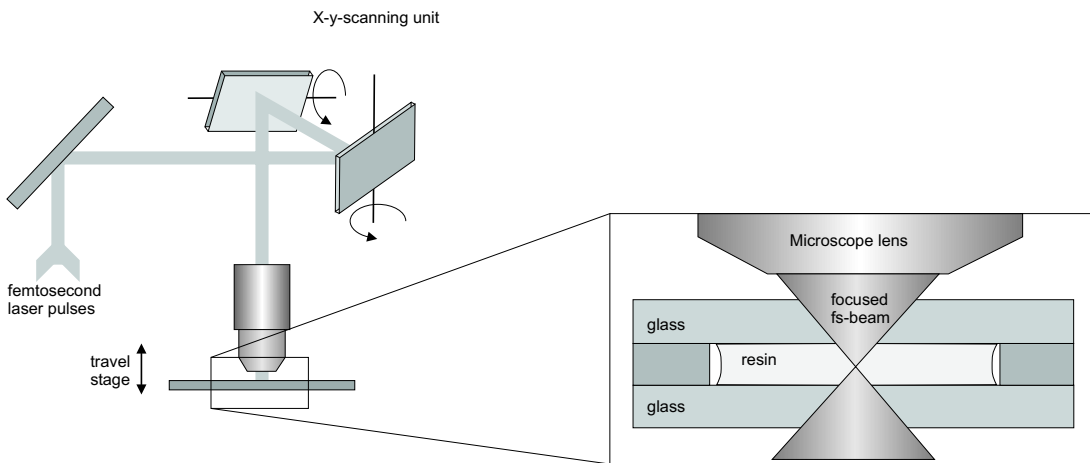


**Figure 3.7:** Principal setup for a two-photon system using femtosecond laser pulses, after [3.24].

### 3.1.1.3 Two-photon processes

By using two-photon processes [3.14, 3.25, 3.26] the feature resolution can be enhanced significantly compared to the two above mentioned processes. Currently, two different setups are used for two-photon-lithography: One approach uses two crossing laser beams. Specially developed resins can only harden in the region where these two beams overlap [3.14]. The second approach [3.24, 3.27] uses highly focused femtosecond laser-pulses. Only in the center of the focus the intensity is high enough to trigger two-photon absorption. By using this approach (see Fig. 3.7) an object can be fabricated by scanning the resin from the top according to the outline of the object. The object is built layer by layer by moving the resin along the z-axis after one x-y-layer has been finished. Two-photon-processes therefore need no recoating system, simplifying the task of fabricating very thin layers (around  $1\ \mu\text{m}$  or even below) (see Fig. 3.8).

In conventional SLA, based on one-photon-induced photochemical reactions, the liquid resin hardens wherever it is exposed to light (and even slightly beyond the exposed regions). The number of polymer molecules, which are formed due to this reaction, is proportional to the number of incoming photons. By using a two-photon process, the probability that a polymer molecule is formed can be made non-linearly dependent on the intensity of the incoming laser beams. The first photon excites the resin-molecules to an intermediate, short living state  $A^*$ , the second photon further excites the molecules from  $A^*$  to  $A^{**}$  from where the photochemical reaction can take place and the polymer-chains are formed. The probability of a photochemical reaction depends on the product of the intensity of the two laser beams (respectively the square of the light intensity if only one laser is used). Since the laser intensity usually varies according to a Gaussian curve across the diameter of the beam, this means that a polymer is most likely formed in the center of the intersection-volume. The feature resolution can therefore be made smaller than the minimum spot size of the laser beams, leading to parts with exceptionally high geometric resolution (see Fig. 3.3).

The main problem with this approach is the small build speed. Since every voxel has

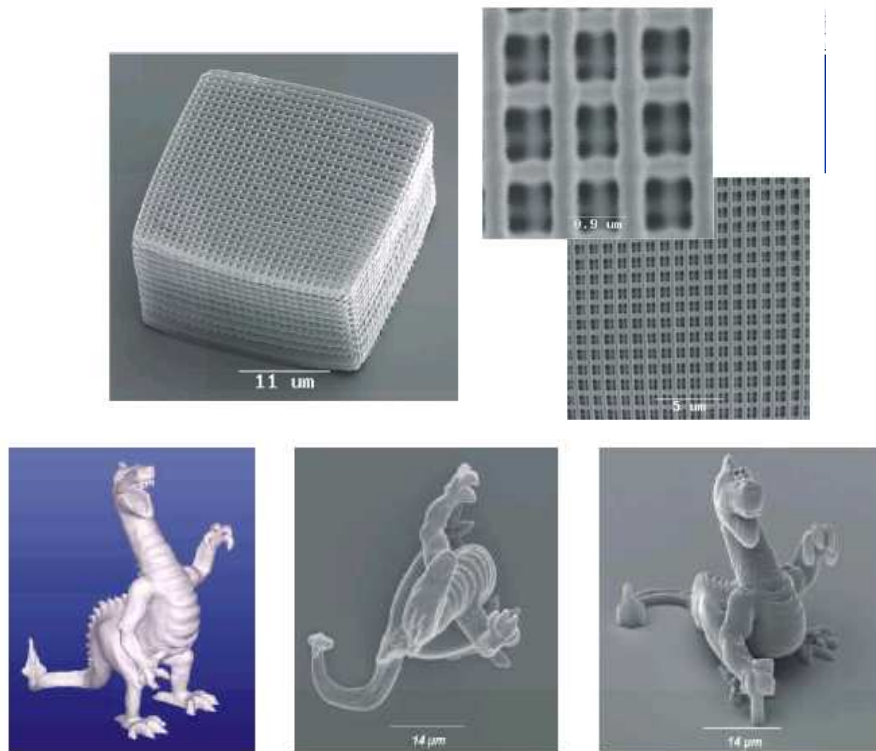


**Figure 3.8:** Cellular structure (top) and dragon (bottom) fabricated by two-photon stereolithography [3.24].

to be exposed sequentially, the build time (assuming cubic voxels with side length  $d$ ) for a constant volume goes up with  $\frac{1}{d^3}$ . For systems based on crossing laser beams, the maximum build size is limited since at least one of the two orthogonal laser beams has to pass liquid resin to get to the intersection site. The resin has to absorb a certain fraction of the incoming light, and if the laser has to travel a long distance through a highly absorbing medium, the intensity at the intersecting site will be too low to start the photochemical reaction. Systems based on one laser [3.24] avoid this problem since they use resins [3.28] which are transparent for the incoming light, and only absorb energy at the doubled laser frequency.

### 3.1.2 Materials for stereolithography

There is a large number of SLA resins available commercially (see Tab. 3.1). Most of these materials are based on epoxy chemistry and depending on the individual requirements (toughness, strength, temperature resistance, colour, ...) each manufacturer offers a number of different materials. Vantico is marketing a resin which can change its colour from transparent to red if the laser intensity exceeds a certain threshold, therefore allowing to color certain regions inside the SLA part.

Except Envisiontec all manufacturers in Tab. 3.1 are selling resins which can be used in machines compatible with the UV-laser based systems from 3D Systems. DMEC is only active on the Japanese market, they are also selling a filled resin which can be

used for tooling applications.

The commercially available SLA resins are mainly used for fabricating polymeric parts. Materials developed by research institutions are also used for fabricating metallic or ceramic parts. This can be achieved by mixing metallic or ceramic powder into the resin [3.20, 3.30–3.32]. Applications where such structures are required include for instance photonic crystals [3.29], where heavily undercut parts need to be fabricated (see Fig. 3.9).

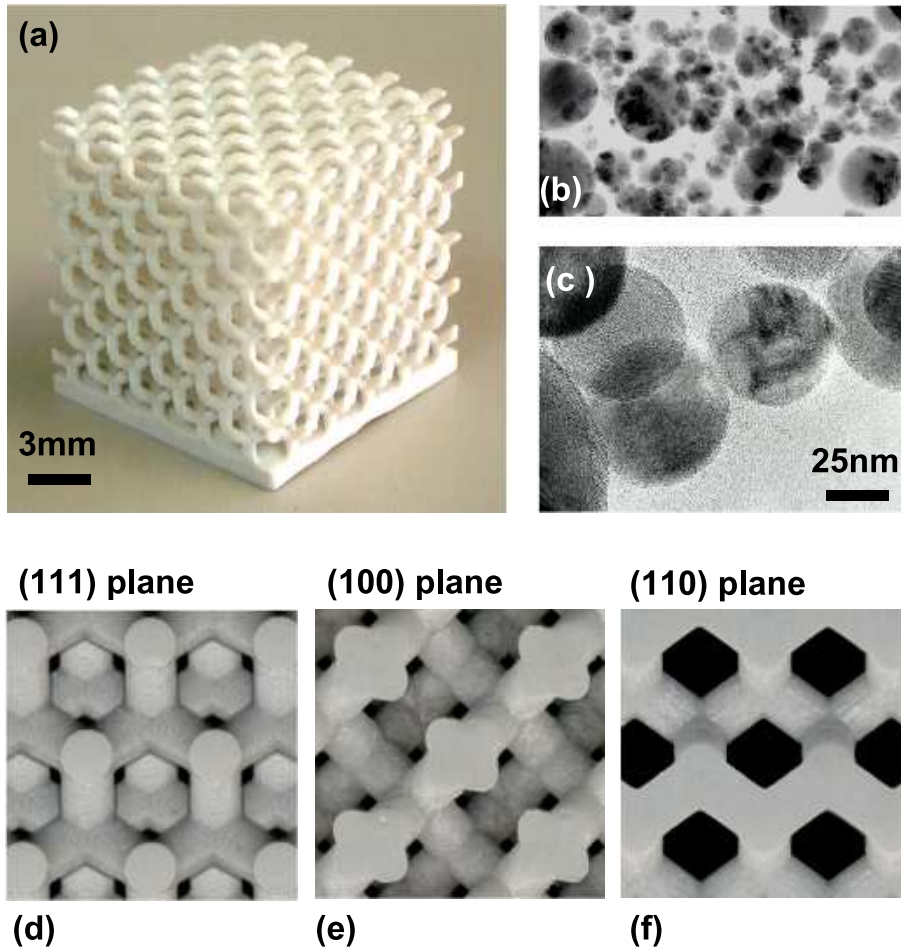


**Figure 3.9:** Photonic crystal (a) made by stereolithography using a powder filled (b, c) resin. (d)-(f) show the shape of the crystal along different optical axes. This anisotropy defines the optical properties of the structure [3.29].

For these applications a conventional SLA machine can be used which uses filled resins instead of unfilled commercial resins. After solidifying defined regions with the laser the remaining resin can be washed off and a green part is obtained which can be further processed by debinding and sintering. Ceramic resins have also been developed for systems using digital mirror devices [3.16, 3.33]. The challenge when using powder filled resins is to achieve a high solid loading and at the same time a good surface quality (the powder particles might scatter the incoming light, thus reducing the feature resolution).

Besides resins filled with metallic or ceramic particles, it is also possible to process resins with elastomeric properties on SLA machines [3.34]. Interesting results have

**Tab. 3.1.** Material suppliers for stereolithography resins.

Supplier	URL	Type of material
Vantico	<a href="http://www.vantico.com">www.vantico.com</a>	epoxy resins, two color resins
RPC	<a href="http://www.rpc.ch">www.rpc.ch</a>	epoxy and acrylate
DSM Somos	<a href="http://www.dsmsomos.com">www.dsmsomos.com</a>	epoxy
D-MEC	<a href="http://www.d-mec.co.jp">www.d-mec.co.jp</a>	epoxy, filled epoxy
Envisiontec	<a href="http://www.envisiontec.de">www.envisiontec.de</a>	acrylate resin

also been achieved by shaping liquid crystals using stereolithography [3.35]. When exposing the nematic liquid crystal to a moderate magnetic field (0.5 - 1 Tesla), it is possible to orient the crystals during photopolymerization. The orientation of the magnetic field can change from layer to layer, yielding a defined anisotropy in the final part. By this way materials with unusual thermo-mechanical properties can be tailored. It is possible to achieve unusually high glass transition temperatures in excess of 300 °C as well as polymeric structures with no thermal expansion in the x-y-plane [3.36, 3.37].

### 3.1.3 Objet Quadra

An interesting variant to the conventional SLA approach has been developed and commercialized by Objet (Isreal) under the name Quadra. This system is based on an UV-curable resin, which is dispensed by an inkjet-printer head with more than 1500 nozzles. The resin is printed on selected regions. After one layer has been dispensed, the liquid resin is flush exposed by an UV lamp and forms a solidified layer. The process is repeated by printing a successive layer of resin.

Since the part is not embedded in liquid resin during the fabrication process, this system uses a second material for fabricating support structures. The support material is UV-curable, too, but it is very soft and can be removed mechanically after the part is taken out of the machine.

According to Quadra, this system can build parts as large as 270x300x200 mm<sup>3</sup> with a x-resolution of 0.08 mm, a y-resolution of 0.04 mm and a layer thickness of 0.02 mm. According to early user-tests the Quadra system can deliver parts with excellent surface quality, but due to the shrinkage of the resin during curing thicker parts tend to warp.

## 3.2 Selective Laser Sintering (SLS)

SLS was among the first RP processes which were made available commercially. DTM (now part of 3D Systems) was founded in 1987 and after operating as service bureau for several years, the first SLS systems were sold in 1992. EOS (Germany) was founded in 1989 and sold their first system in 1990.

The principle of the SLS process is depicted in Fig. 3.10. Using a galvanometric mirror system, a laser beam is scanned over a powder bed. Where the beam hits the powder

surface, the particles are thermally bonded together, therefore forming a solid object. After one layer has been scanned by the laser, the part is lowered and a next powder layer is spread over the powder bed. The process is repeated until the part is complete. The part can be removed from the powder bed with the unsintered powder (which can be reused for the next process cycle) and the part is ready for secondary processes.

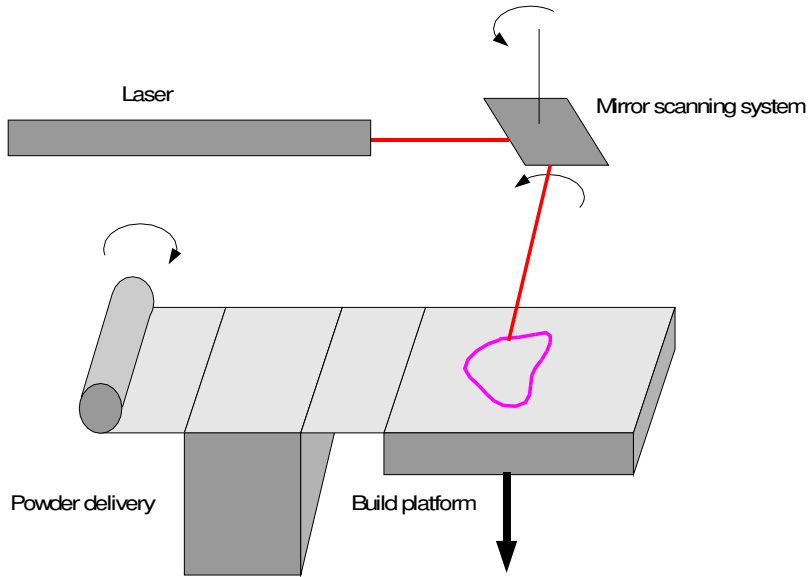


**Figure 3.10:** Working principle for selective laser sintering.

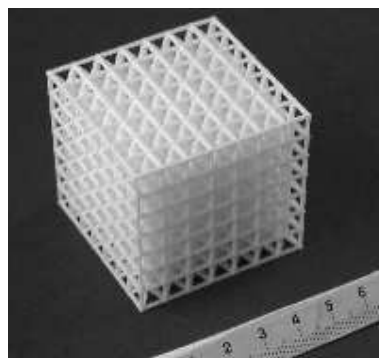
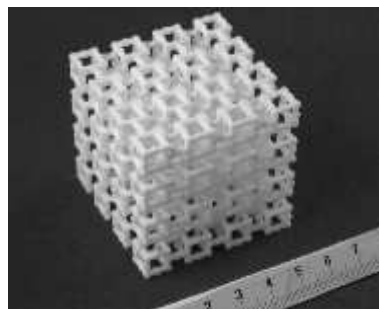


**Figure 3.11:** Parts made on an SLS machine.

A broad variety of materials is available for SLS, including polymers, metals and ce-

**Tab. 3.2.** Materials for selective laser sintering (3D Systems).

Material		Duraform PA	GF	ST 100	Castform PS
Property	Units				
Tensile strength	MPa	44	38	510	3
Tensile modulus	MPa	1600	5910		1600
Young's modulus	GPa			137	
Elongation	%	9	2	10	
remark		Polyamide	glass filled Polyamide	bronze infiltrated stainless steel	wax infiltrated Polystyrene

**Tab. 3.3.** Strength values for tensile test samples with different orientation.

Sample	Elastic modulus	Tensile strength
	MPa	MPa
x 1	630	35
x 2	730	30
y 1	235	9
y 2	530	19
z 1	144	2
z 2	361	5

ramics. The simplest approach is to fuse low-melting polymeric powders with an infrared laser (usually a CO<sub>2</sub> laser with a power range between 20 and 100 W). Available polymeric materials (see e.g. Tab. 3.2) include polyamide, elastomeric materials and polystyrene (which can be used for investment casting). Since SLS can process conventional thermoplastic materials, SLS-parts can be used as functional prototypes with mechanical properties that are comparable to injection molded parts. A polymeric SLS part is shown in Fig. 3.11. The surface finish of SLS parts is mainly delimited by the size of the used powders (usually in the range of 50  $\mu\text{m}$ ). Typical surface roughness values  $R_a$  are around 10  $\mu\text{m}$ .

When fabricating polymeric SLS parts care has to be taken to use appropriate processing parameters. In Tab. 3.3 parts made by an RP service bureau have been tested for their tensile strength and elastic modulus in different directions. According to the data sheet, a strength of 40 MPa was to be expected. The measured data, especially in z-direction, is significantly different from this value. The probable reason for this is an inappropriate machine setup with too thick layers and/or too high scan speed. This example clearly indicates the permanent need for quality control when RP is used to fabricate functional parts. This issue had to be considered for testing the mechanical properties of cellular solids presented in Chap. 8.

For the fabrication of metallic SLS-parts, there are currently two approaches in use: The direct approach [3.38] [3.39] where metallic particles are directly fused together. This approach is described in more detail in the following section.

The indirect approach [3.40–3.42] uses polymer-coated metal powder. The Vanguard machines sold by 3D-Systems are based on this type of process. The laser beam is strong enough to partially melt the polymeric skin of the metal powder. The liquid polymer sinters the particles together. The process delivers a so-called green part which needs further processing to obtain a dense metallic part. After thermally removing the polymer binder, the part can either be infiltrated with a low melting metal or it can be sintered to full density. In both cases (especially during sintering) the dimensions of the part will change, and this change has to be compensated by adjusting the CAD-models which serve as input for the machine.

**Direct laser sintering of metals** Several research groups [3.43, 3.44] as well as commercial suppliers (EOS, Optomec) are using direct laser sintering to fabricate dense metallic parts. Since the melting point of most metals is far above the melting point of polymers, this direct SLS approach is based on lasers with significantly higher power (several hundred W to several kW). Materials which have been processed with this approach include steels [3.45, 3.46], bronze-steel or copper-steel compound materials, titanium alloys [3.47, 3.48] and even refractory metals.

This direct approach is appealing because it allows the direct fabrication of complex, functional metallic parts. The process is material-saving since the non-sintered powder can usually be reused. When feeding different materials into the laser beam, it is even possible to fabricate composite or gradient materials [3.49]. The main markets which are targeted by this approach are the fabrication of tooling inserts and Rapid Manufacturing of small series parts for the aerospace industry (load bearing parts, gas turbine components, ...).

The parts made by direct laser sintering can either be used as fabricated or they can be post-processed with various finishing techniques like machining or electro discharge machining. Secondary processes cause additional fabrication time and increased cost, but they help to improve the accuracy of the parts and the surface finish. The part in Fig. 3.12 is as manufactured.



**Figure 3.12:** Steel parts made by direct laser sintering (EOS GmbH).

In [3.50, 3.51] it is shown, how laser sintering can be used to deposit several materials in one part. By using sacrificial materials (which can be etched if they are made of bulk material or blown out if they are in powder form) it is possible to generate internal channels, which can for example serve as conformal cooling channels when used in mold inserts.

One challenge which has to be overcome when using direct laser sintering is to com-

compensate for the distortion that can be caused when the liquified metal shrinks during solidification. This problem occurs not only in direct laser sintering but also in other RP processes where the build material undergoes a phase transformation while the part is fabricated (e.g. SLA resin changes its volume during photocuring). The problem is illustrated in Fig. 3.13 and Fig. 3.14. Metal powder is deposited on a previously shaped layer and molten by the laser beam. During the solidification process the liquid metal attaches to the underneath layer and starts to solidify. This phase transformation causes the metal to shrink, introducing compressive stresses in the previously built layer and tensile stresses in the current layer. If these stresses become too large, the metal can be deformed plastically, leading to a christmas-tree like structure shown in Fig. 3.14.

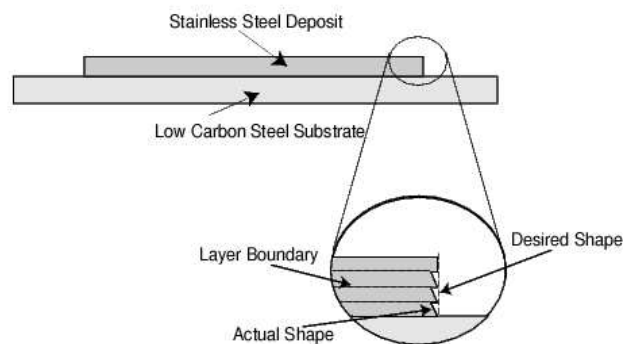


**Figure 3.13:** Origin of christmas tree steps [3.51].

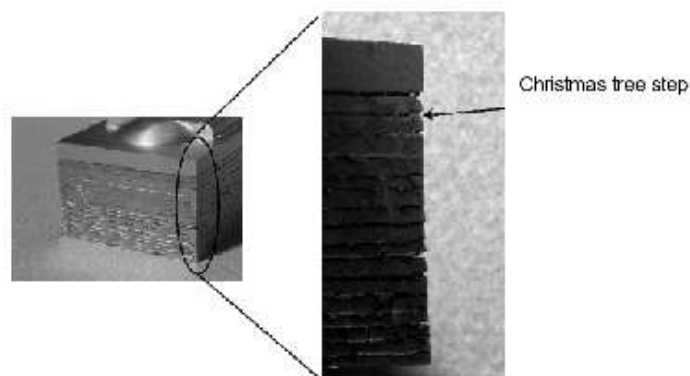


**Figure 3.14:** Metal part showing christmas tree steps [3.51].

A second issue that has to be considered is the rapid cooling rate which the molten material is undergoing during the build-process. In many cases this rapid solidification will lead to hard but brittle materials. Due to these two reasons special processing conditions and materials have to be used to fabricate useful metal parts with direct laser sintering.

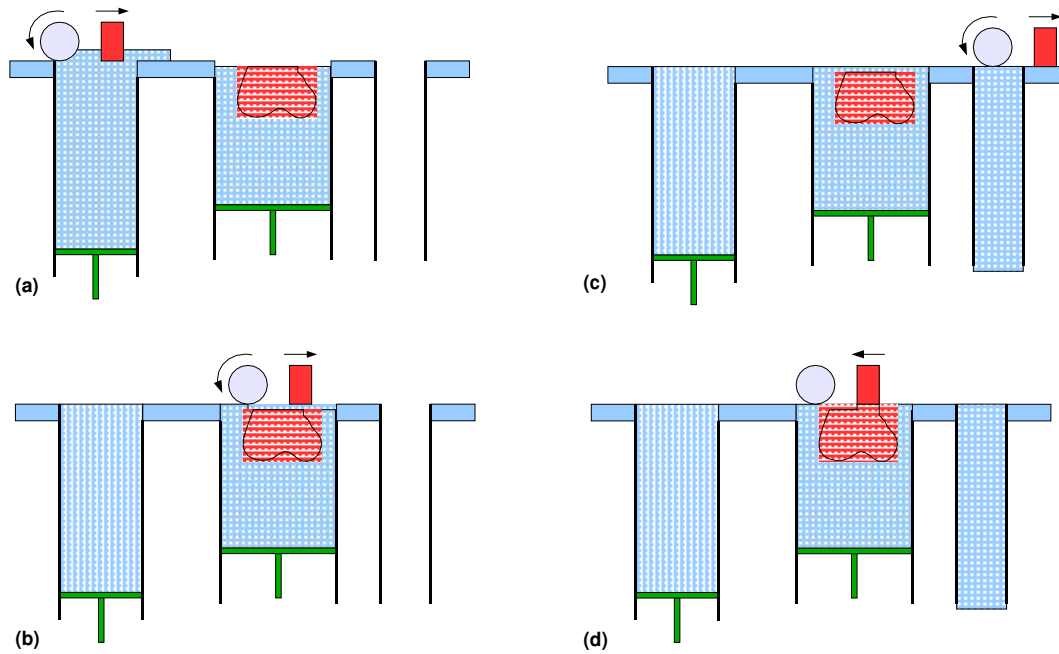


**Figure 3.15:** Build process for a part made by ZCorps 3D printing process.

### 3.3 3D Printing

3D printing is a process which was originally developed at MIT [3.52, 3.53] and was first commercialized by zCorp. It is based on selectively bonding powder particles by infiltrating them with a polymeric binder which is printed using inkjet-technology. The working principle is depicted in Fig. 3.15: In a first step the printer spreads powder from the feed box onto the build platform Fig. 3.15 (a),(b). When the build platform is completely coated with a layer of fresh powder (Fig. 3.15 (c)) the inkjet head (equipped with 120-1200 nozzles) starts to print a 2D-pattern onto the loose powder, see Fig. 3.15 (d). As “ink” a polymeric binder is used which bonds the loose powder particles. When the printing process is complete, the next powder layer is deposited onto the build platform and the process is repeated until all layers are built. A fairly large number of materials can be processed with 3D printing. Commercial suppliers offer starch- and mineral-based powders as well as metallic and ceramic powders.

#### Inkjet printing

Besides the already commercialized 3D-printing process, science-oriented projects are relying on inkjet printing for the deposition of functional and structural arrays with arbitrary geometry. One advantage of this process is the minimal consumption of materials. Droplets are only deposited where material is required. This is especially important where opto-electronic [3.54] or biomedical [3.55] applications are targeted. Inkjet printing allows the processing of many liquids, as long as the viscosity is low enough to allow the formation of sufficiently small droplets [3.56].

Systems currently in development can deposit droplets in the range of 10-20 pico-liter

with an x-y-placement error around  $5\ \mu\text{m}$  [3.57], and by using several print-heads it is possible to deposit multiple materials in each layer. Most of the currently investigated applications still operate with one or very few layers, for instance to fabricate DNA micro-arrays for cell sorting, protein deposition or drug delivery.

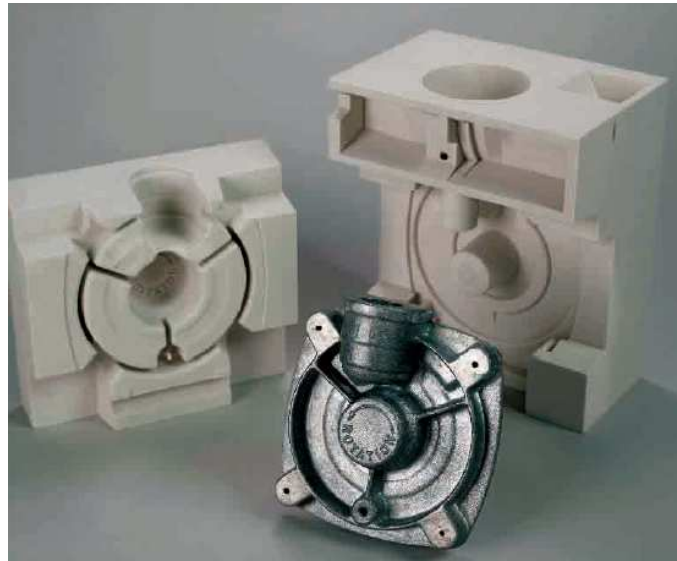


**Figure 3.16:** Molds for metal casting made by the 3DP Direct Metal Casting process [3.58].

## 3.4 Systems based on the deposition of thermoplastics

---

### 3.4.1 Fused Deposition Modeling (FDM)

FDM is a process based on the extrusion of liquified thermoplastic polymers. A thread made of this thermoplastic material is fed through a heated nozzle where it is heated slightly ( $0.5^\circ$ ) beyond the melting point of the material. The nozzle moves in x-y direction and extrudes the material onto the base where it is fused with the underlying material (see Fig. 3.17).

In order to be able to build parts with overhangs, systems based on FDM need to work with a second nozzle which extrudes a support material onto which the overhanging part material can be extruded. This support material can either be removed mechanically or by dissolution in water (if water soluble wax is used as support). Currently FDM systems are commercially offered by Stratasys. Stratasys is also offering a water soluble support material (Water Works) which significantly simplifies the task of removing the support structure compared to the traditional support materials which had to be removed mechanically.

Stratasys offers a range of systems which mainly differ in the build speed and the achievable build volume. One of the main advantages of FDM is the large range of available materials. Since many thermoplastics can be used, parts made by FDM not

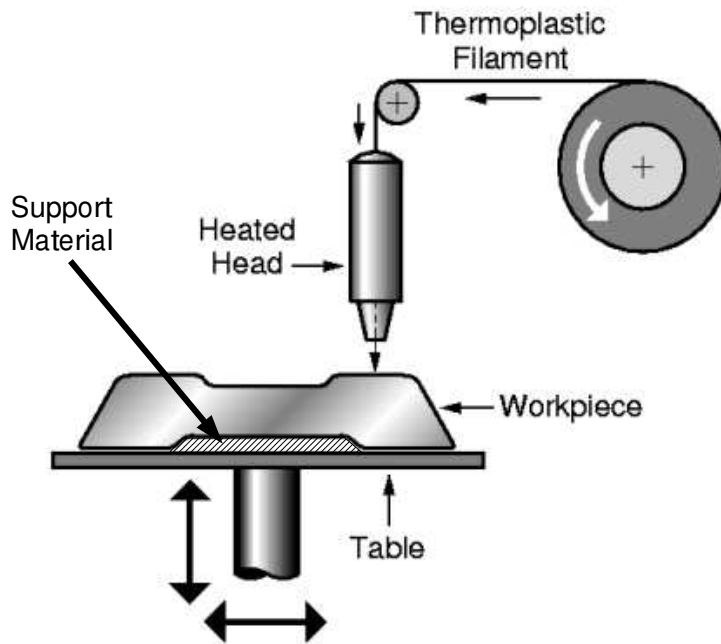


**Figure 3.17:** Working principle of fused deposition modeling, after [3.59].

only serve as visual aids, but they can also be used as functional parts for the evaluation prototypes which later on will be mass-manufactured by plastic injection molding.

Currently Staratsys offers build materials out of investment casting wax, acrylonitrile butadiene styrene (ABS), polycarbonate and an elastomer. The build and support material are stored as filament (diameter 1.7 mm) on a spool and a drive block feeds the filament into the heating chamber where it is brought to the appropriate temperature. The extrusion is achieved by a tip which reduces the diameter of the filament before it is deposited onto the build platform.

FDM was one of the first RP technologies that were offered commercially. The main drawback of these systems is the fact that they use only one nozzle to deposit material. In order to keep the build time reasonably low, the diameter of the filament cannot be too small, therefore the accuracy and surface smoothness achieved by FDM is somewhat lower than that of competing technologies. Especially droplet-based processes which can use large number of parallel nozzles are becoming a strong competition for FDM.

### 3.4.2 ModelMaker Series

The Model Maker series of RP machines was developed in the early 1990s by Sanders Prototype (now Solidscape Inc.) and is based on inkjetting wax droplets on a build platform. The system uses two nozzles, one dispenses the build material, the other one the support material, which later on is washed away by using a special solvent (Bioact). The system can produce very accurate parts by jetting tiny wax-droplets. In order to keep the thickness of the individual layers within tight tolerances, each layer

is machines flat after completion of the deposition process.

Parts made by the Model Maker process are mainly used as patterns for investment casting. Due to the high accuracy and good surface finish of these parts, the jewellery and medical industry are making large use of these systems. The Model Maker is mainly useful for the fabrication of small, intricate parts since the build time for larger structures becomes inhibiting high.

#### 3.4.3 MultiJet Modeling

Multi-Jet-Modeling is an RP technique developed and commercialized by 3D-Systems. The principle of these machines is based on inkjetting molten wax droplets onto the build platform through a large number of nozzles (around 300). The wax solidifies after being printed onto the build platform, and by turning on and off the nozzles individually the part can be printed.

The key advantages of these systems is the fact that they can be used in an office environment and that their build speed is quite high (due to the use of a large number of deposition nozzles).

3D-Systems currently offers two different build materials. One is used for the fabrication of patterns for investment casting (where the focus is put on a good surface finish), the other can be used for printing parts which are used as visual aids or concept models and which need a higher strength than the wax parts for investment casting.

## 3.5 CNC Machining, Shape deposition Manufacturing

---

Computer numerical control (CNC) machining is the basis for many near-net and net-shape manufacturing processes. Its advantages are the high accuracy that can be achieved as well as the large number of engineering materials which can be shaped by machining. CNC based techniques are used for a number of RP-processes, and several manufacturers offer RP machines using CNC-methods.

The main disadvantage of CNC machining is the complex process which is necessary to generate appropriate code for the CNC-path generation. The conventional CNC-code generation for a part with complex geometry can be a time-consuming task which has to be done by an experienced engineer. To simplify this task, several strategies have been developed which can help to make CNC based techniques useful for RP applications [3.60]

#### **Shape Deposition Manufacturing**

Shape Deposition Manufacturing is a process developed at Stanford University [3.39, 3.50, 3.61]. It is based on combining additive and subtractive manufacturing techniques using CNC-milling as shaping process. Several variants have been developed, depending on the desired target material. By using additive and subtractive processes

at the same time, it is possible to separate the shaping process from the deposition process. Whereas in most other RP processes the part accuracy is limited by the deposition process (which determines the layer thickness), SDM shapes the deposited material later on, thus improving surface finish and tolerance range of the final part.

Since it is possible to use different deposition techniques which do not necessarily need to be very accurate regarding the quality of the deposition patterns, it is possible to use a broad spectrum of materials. These materials include metals (deposited by plasma spraying or laser deposition [3.39]), thermosetting polymers, waxes and ceramics [3.61, 3.62]. It is also possible to embed sensors into these structures [3.63]. In Chap. 6 it is shown, how Mold SDM can be used to fabricate complex ceramic parts.

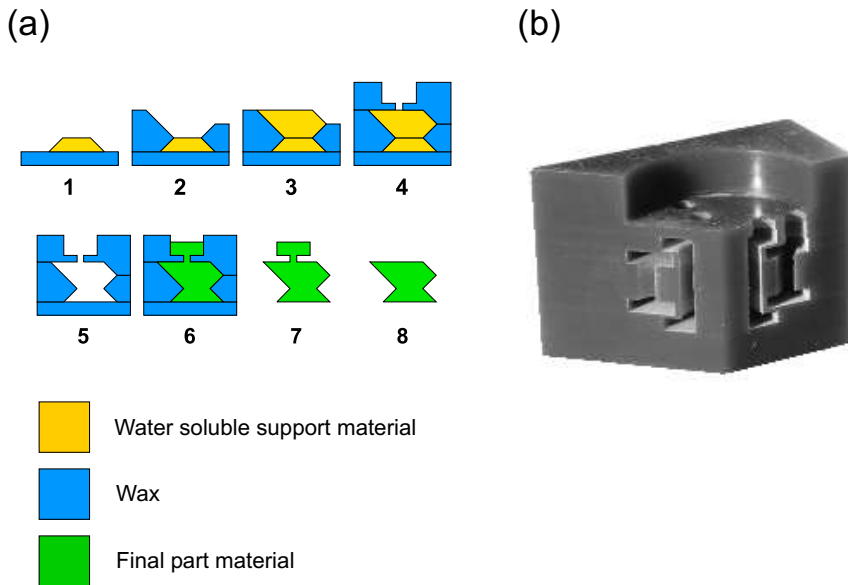


Figure 3.18: Mold SDM.

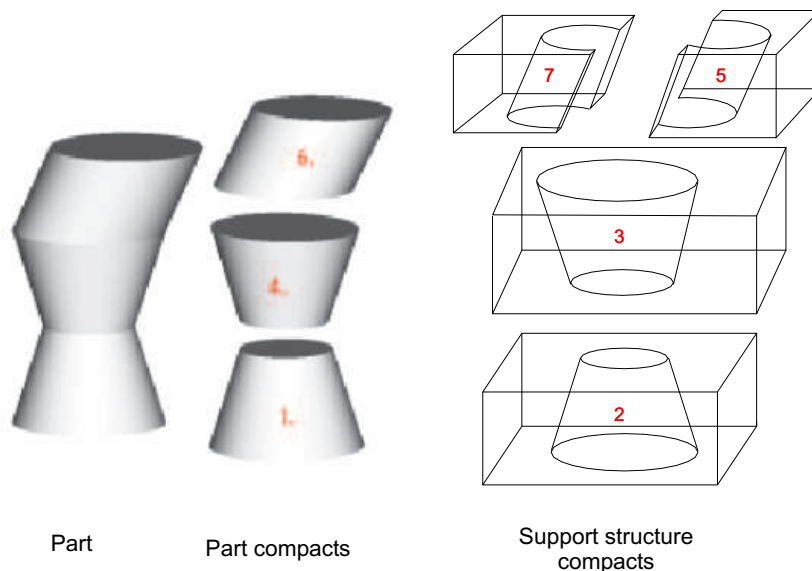


Figure 3.19: Decomposing a part into compacts [3.50].

For the fabrication of polymeric and ceramic components, a variant of SDM called Mold SDM has been developed. The process scheme for Mold SDM is depicted in

Fig. 3.18: The part and the surrounding mold have to be decomposed into manufacturable compacts (see Fig. 3.19). Each compact must have a geometry which is machinable. The thickness (in contrast to other layer-based RP processes) is not necessarily constant. After the part decomposition is complete, the CNC-code for each compact is generated and the mold, including the sprue and runner system, is manufactured (Fig. 3.18 (1)-(4)) using two different materials. A mold material and a sacrificial (water soluble) material. The sacrificial material has the same shape as the final part and serves as support structure for the mold material. The mold material is typically a low-melting wax and the sacrificial material is either a UV-curable resin or a water soluble wax.

All materials need to be machinable and whenever one compact has been finished, the liquid material for the next compact is deposited using a simple dispensing system. The material then solidifies either by UV-curing or by cooling down below the melting temperature.

After all compacts have been machined Fig. 3.18 (4) the sacrificial material is dissolved in water in order to obtain the final mold in Fig. 3.18 (5). After casting the target material (Fig. 3.18 (6)) the mold can be removed by melting off the wax material (Fig. 3.18 (7)). By using various room-temperature molding processes, the mold can be filled with polymeric resins or powder filled (ceramic and metallic) slurries.



**Figure 3.20:** Ceramic gas turbine made by Mold SDM. The picture on the left shows the sacrificial turbine-compact after milling. The picture on the right is the ceramic turbine in the green state. The diameter of the turbine is 12 mm.

A ceramic sample part which has been manufactured by this route is shown in Fig. 3.20. The picture on the left shows the turbine out of sacrificial water soluble material during shaping, and the picture on the right the final ceramic part after melting off the mold.

Compared to other RP processes Mold SDM has several advantages: The accuracy as well as the surface finish are very good due to the use of CNC machining for shaping the compacts. Since the final part is cast in one step, there exist no bonding-problems between neighbouring layers. Especially in the case of brittle materials like ceramics this is of advantage. The main drawback is the larger amount of work which is necessary to decompose the part into compacts and to generate the cutting files.

### 3.6 Laminated Object Manufacturing (LOM)

LOM (see Fig. 3.21) is an RP technique which manufactures three-dimensional models by stacking individually sheets of paper (or composites, respectively). Before stacking, the individual layers are cut out of a roll of paper, coated with an appropriate adhesive. The roll of paper is guided over the build platform, and a laser beam cuts out the contours of the desired layer. Regions of the paper which are not part of the 3D-structure are cross-hatched in order to be removed later on. After one layer has been completed, the build platform is lowered and the paper roll advances. These steps are repeated until the part is complete.

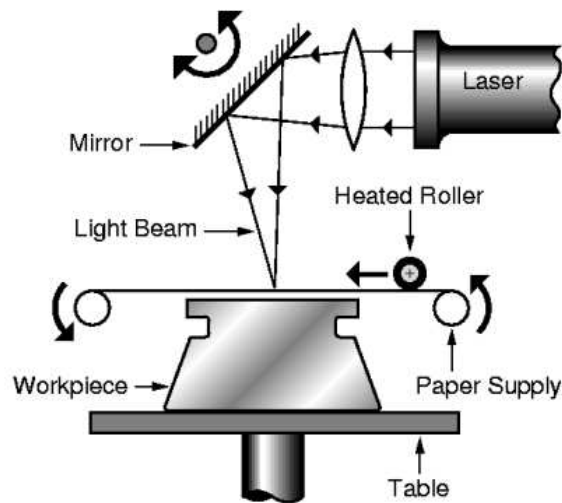


**Figure 3.21:** Working principle of layered object manufacturing, after [3.59].

Since LOM is a combination of additive and subtractive processes, it can be used for the fabrication of large parts (the laser has only to cut out the contours of each layer, which increases the build speed compared to other RP techniques).

The main drawback is the labor-intensive post-processing. The cross-hatched, unnecessary paper has to be removed manually, which can be a time-consuming task. Since the strength of LOM-parts is somehow limited, they are frequently used as lost patterns for secondary processes (e.g. investment casting, sand casting, ...).

A typical processing sequence for a LOM part is shown in Fig. 3.22 [3.64]: The part comes out of the machine as a block (a) which includes the cross-hatched support material as well as the part material. First, the support-base layer, onto which the first paper-layers are laminated, has to be removed (b). In a next step (c) the outer support wall has to be removed.

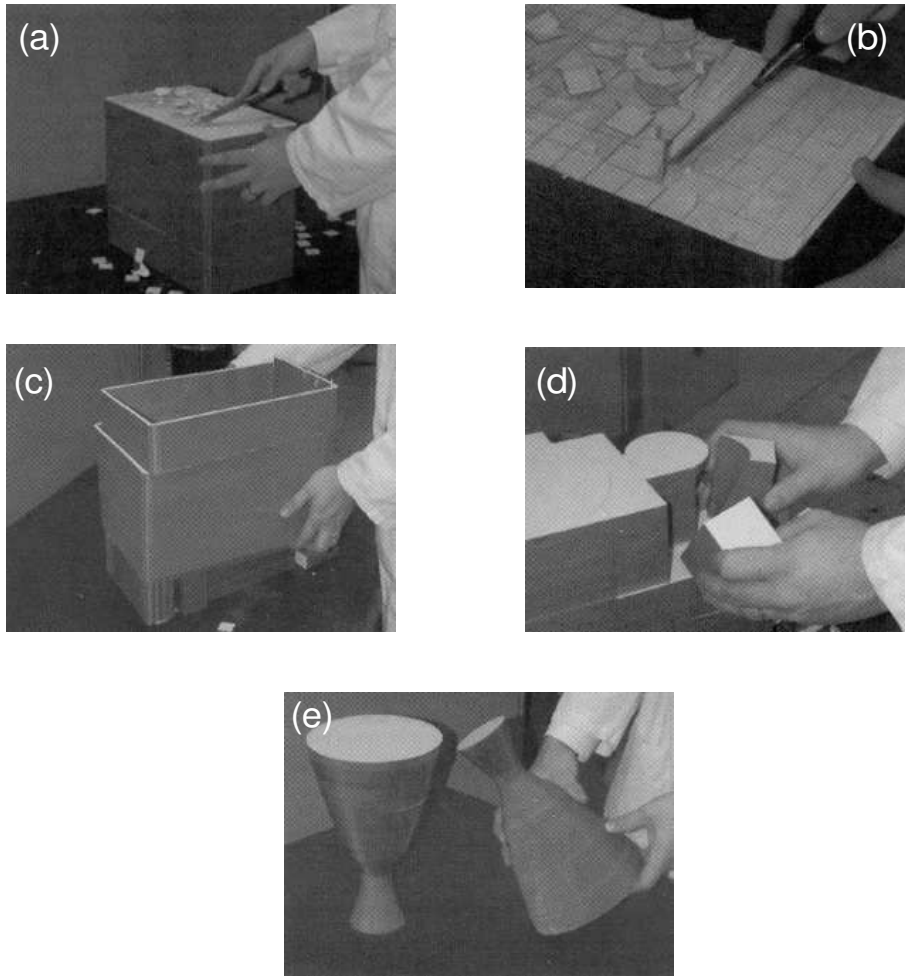


**Figure 3.22:** Processing sequence for a LOM part [3.64].

## 3.7 System selection

The following tables and charts summarize the most relevant system parameters for commonly used RP systems. They should help to compare the individual advantages and drawbacks when selecting a system for a specific application.

In Fig. 3.23 the tolerance range versus surface roughness RMS are depicted for selected RP systems together with RP related secondary molding processes. The tolerance range is given for a part with dimensions around 25 mm.

It can be seen that most molding processes (except sand casting) exhibit a very good surface finish, this means the surface of the master pattern which is molded, is replicated with high accuracy. Due to the internal stresses that arise during most molding processes, the molded parts can warp and the tolerance range suffers. These stresses can either be caused due to changes in temperature (solidification of molten material in plastic injection molding or in metal-castings) or by chemical reactions that cause a volume change of the molded material (electroplating and silicone molding).

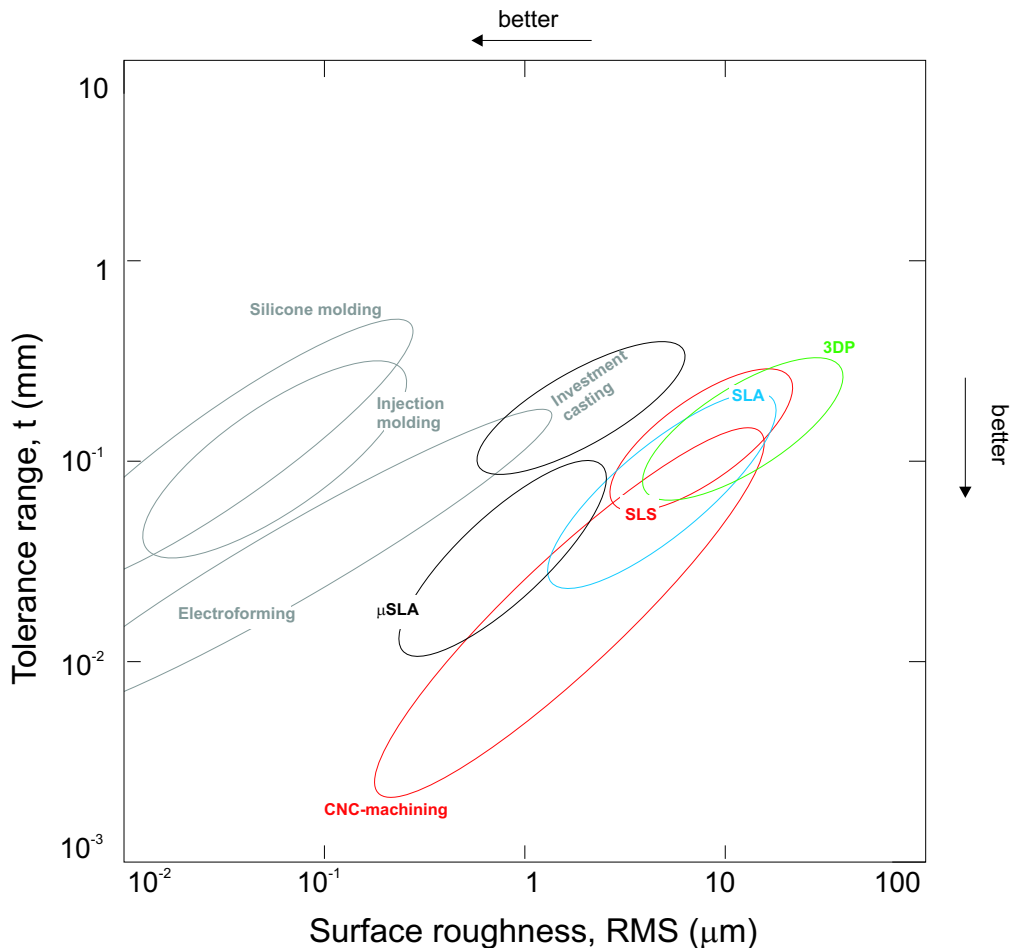


**Figure 3.23:** Tolerance range  $t$  versus surface roughness  $RMS$  for selected RP-related processes, modified after [3.65]. The tolerance range is given for parts with dimensions around 25 mm.

From Fig. 3.23 it also becomes obvious why RP is still struggling to become a standard process for tooling applications whereas prototypes for investment casting are already made on a routine basis using RP: The injection molding process replicates the tool surface with significantly higher precision than investment casting. The most commonly used RP processes can generate patterns with a smooth enough surface for investment casting. For a high quality injection molding tool the surface quality should roughly be one order of magnitude better than currently possible. This means that extensive post-treatment of RP patterns is necessary to make them suitable for tooling applications. The tool insert must also meet tight tolerances along the parting line to avoid flashing.

For estimating the cost of printing a part with a certain height, the build speed versus system cost of various RP systems is depicted in Fig. 3.24.

### Rapid manufacturing versus traditional manufacturing processes

One of the most appealing aspects of RP is the fact that arbitrary shapes can be built without tooling.

When the decision has to be made between traditional manufacturing processes (in

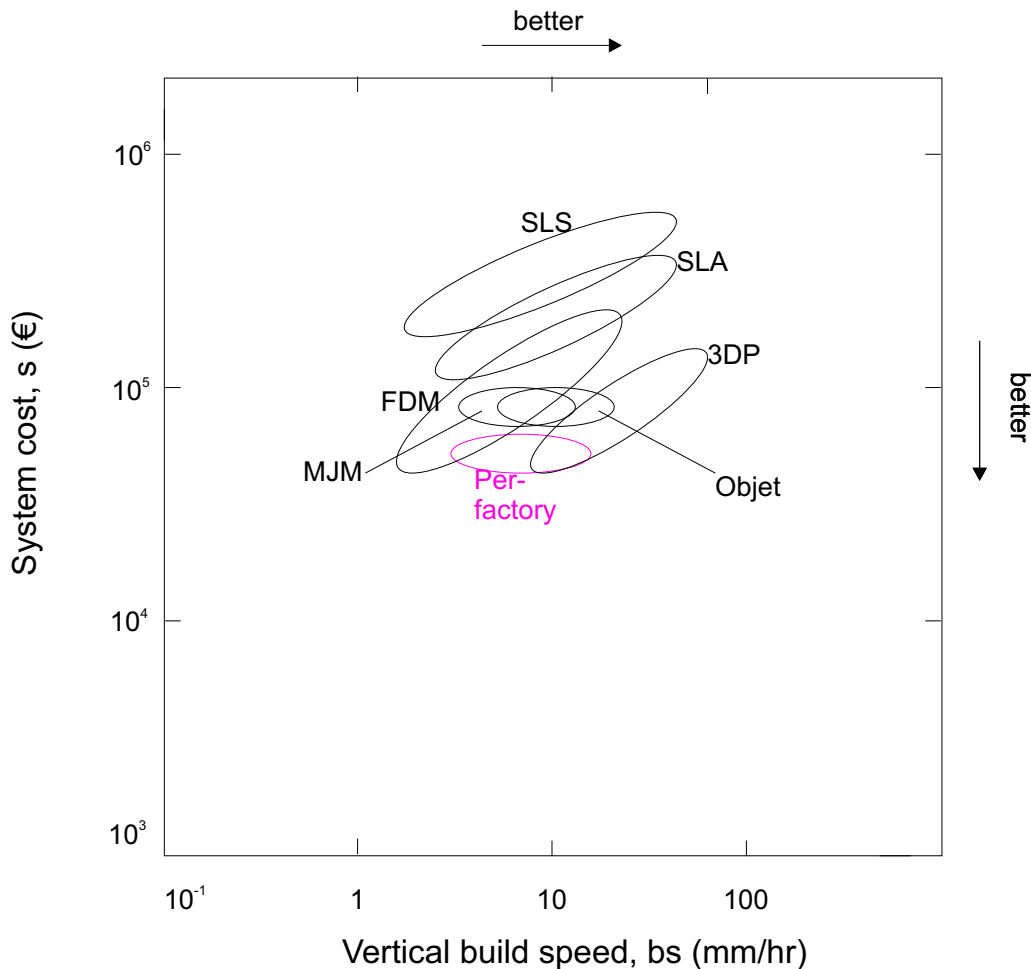


**Figure 3.24:** Build speed versus system cost for selected RP systems.

many cases injection molding) and rapid manufacturing (RM), several issues have to be considered:

- How important is the lead-time? The faster the final part has to be delivered and the more likely frequent design changes will occur, the more appealing is the use of rapid manufacturing.
- How large is the part? The build time and the material cost of an RP part is heavily depending on the part volume. There is only a weak dependence between cycle time and part volume in conventional processes like injection molding. Furthermore materials for mass fabrication are significantly cheaper (e.g. around € 2 per kg for injection molding feedstock compared to € 200 per kg for RP material) than materials for RM.
- How important is the surface quality? Traditional, tooling based manufacturing processes can deliver very accurate parts with high surface finish, as long as the tool is accurate enough and has an appropriate surface. This means that eventually necessary post-treatment needs only to be done once (on the tool). In the case of RM, each part has to be post-treated individually. This means that RM is economically only feasible if no or very little post-treatment is required.

- Is the required material available for RP? The number of available RP materials is steadily increasing. Nevertheless a much larger number of various materials is available for traditional manufacturing processes, and not all of their properties can be mimicked by RP materials.

Overall, it has to be decided whether RP can (1) fulfill the required technical requirements (material, surface quality, accuracy, ..) and (2) if there is an economic advantage when using RM instead of traditional processes. The previous sections can help to decide whether the RM project is feasible technically. For the economic aspect an approach used in [3.65] can be utilized. Using the following equations, charts like the one depicted in Fig. 3.25 can be calculated. These charts help to decide, which minimum batch size is required to make traditional mass manufacturing methods more economical than RM.

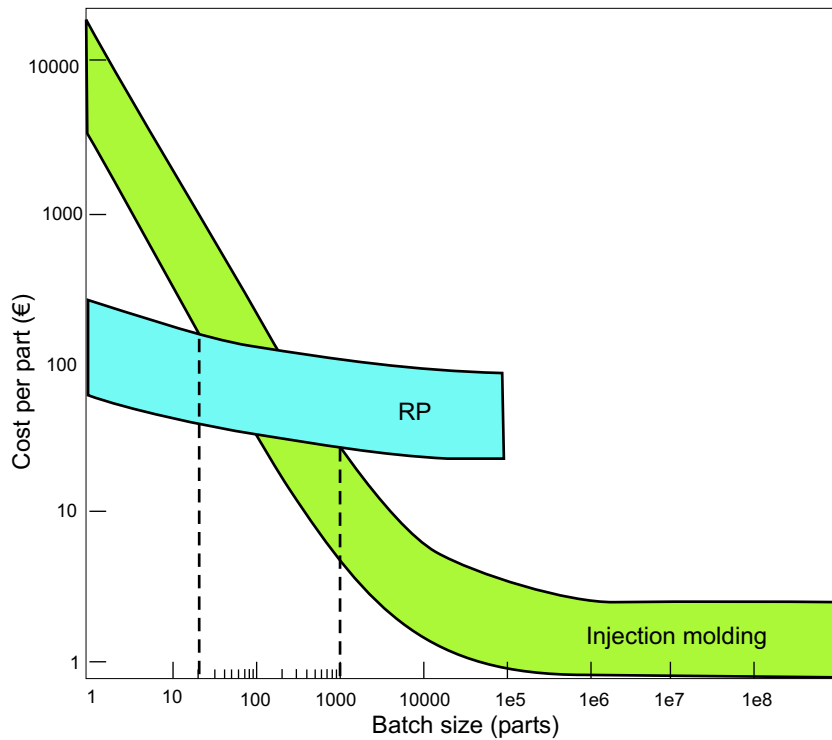


**Figure 3.25:** Cost per part versus batch size for parts made by injection molding and RP.

In this resource-based approach the cost  $C$  for a part of mass  $m$  is made up of the cost for material  $C_m$  (€/kg), tooling  $C_t$  (€) and the gross overhead  $\dot{C}_{L,gross}$  (€/hr).

$$C = [mC_m] \quad + \quad \frac{1}{\dot{n}} [C_t] \quad + \quad \frac{1}{\dot{n}} [\dot{C}_{L,gross}], \quad (3.1)$$

where  $\dot{n}$ , the batch rate, is the number of parts produced per hour .

In more detail, the gross overhead rate can be broken down to the basic overhead rate  $\dot{C}_{L_0}$  which includes for instance cost for labor, the capital write-off and the cost for energy and space:

**Tab. 3.4.** Resources used in production, after [3.65].

Resource		Symbol	Unit
Materials	incl. consumables	$C_M$	€/kg
Capital	cost of equipment	$C_C$	€
	load factor	$L$	
	write-off time	$t_c$	yr
	cost of tooling	$C_t$	€
Time	overhead rate	$\dot{C}_L$	€/hr
Energy	power	$\dot{P}$	kW
	cost of energy	$C_e$	€/kWh
Space	area	$A$	m <sup>2</sup>
	cost of area	$\dot{C}_s$	€/m <sup>2</sup> h

$$\dot{C}_{L,gross} = \dot{C}_{L_0} + \frac{C_c}{L t_c} + \dot{P} C_e + A C_s. \quad (3.2)$$

For used abbreviations see Tab. 3.4. This cost model is only a simplified approach to estimate the cost for using a certain process. The cost contributors in Eq. 3.1 and 3.2 could be further broken down in order to describe costs caused by royalty payments, costs for waste disposal, for administration, and so on.

Regarding RP and RM, the most dominant cost factors are capital cost (determined by equipment prices and build speed), material cost and cost for labor (especially important if post-processing of RP parts is necessary).

## 3.8 References

- 3.1 D.T. Pham and R.S. Gault. A comparison of rapid prototyping technologies. *Int. J. of Machine Tools & Manufacture*, 38:1257–1287, 1998.
- 3.2 J.P. Kruth. Material increment manufacturing by rapid prototyping techniques. *CIRP Annals*, 40(2):603–614, 1991.
- 3.3 J.-C. André, A. Le Méhauté, and O. De Witte. Dispositif pour réaliser un modèle de pièce industrielle. French Pat. 2.567.668, 1986.
- 3.4 C. Hull. Apparatus for production of three-dimensional objects by stereolithography. U.S. patent 4,575,330, 1986.
- 3.5 A.J. Herbert. Solid object generation. *J. Appl. Photo. Eng.*, 8(4):185–188, 1982.
- 3.6 H. Kodama. Automatic method for fabricating a three-dimensional plastic model with photo-hardening polymer. *Rev. Sci. Instr.*, 52(11):1770–1773, 1981.

- 3.7 P.F. Jacobs. *Rapid prototyping and manufacturing*. Society of Manufacturing Engineers, Dearborn, 1992.
- 3.8 A. Gebhardt. *Rapid Prototyping - Werkzeuge für die schnelle Produktentwicklung*. Hanser Fachbuch, München, second edition, 2000.
- 3.9 M. Madou. *Fundamentals of microfabrication*. CRC Press Boca Raton, New York, 1997.
- 3.10 P. Rai-Choudhury, editor. *Handbook of microlithography, micromachining and microfabrication*. SPIE, Washington, 1997.
- 3.11 R. Brück, N. Rizvi, and A. Schmidt. *Angewandte Mikrotechnik*. Carl Hanser Verlag, München, 2001.
- 3.12 A. Bertsch, P. Bernhard, and P. Renaud. Microstereolithography: Concepts and applications. In *Proceedings of 8th IEEE International Conference on Emerging Technologies and Factory Automation (ETFA 2001)*, pages 289–298, 2001.
- 3.13 V.K. Varadan, X. Jiang, and V.V. Varadan. *Microstereolithography and other fabrication techniques for 3D MEMS*. John Wiley and sons Ltd, 2001.
- 3.14 S. Kawata, H.-B. Sun, T. Tanaka, and K. Takada. Finer features for functional microdevices. *Nature*, 412:697–698, 2001.
- 3.15 S. Monneret, V. Loubere, and S. Corbel. Microstereolithography using a dynamic mask generator and a non-coherent visible light source. In *Proceedings of the 1999 Design, Test, and Microfabrication of MEMS and MOEMS*, pages 553–561. Society of Photo-Optical Instrumentation Engineers, Bellingham, WA, Paris, Mar.30-Apr. 1 1999.
- 3.16 S. Ventura, S. Narang, P. Guerit, S. Liu, D. Twait, P. Khandelwal, E. Cohen, and R. Fish. Freeform fabrication of functional silicon nitride components by direct photo shaping. In *Solid Freeform and Additive Fabrication*, Materials Research Society Symposium - Proceedings, pages 81–89. MRS, San Francisco, April 24-26 2000.
- 3.17 A. Bertsch, S. Zissi, J.Y. Jezequel, S. Corbel, and J.C. André. Microstereophotolithography using a liquid crystal display as dynamic mask-generator. *Microsystem Technologies*, 3(2):42–47, 1997.
- 3.18 A. Bertsch, H. Lorenz, and P. Renaud. 3D microfabrication by combining microstereolithography and thick resist UV lithography. *Sensors and Actuators A*, 73(1-2):14–23, 1999.
- 3.19 H. Kück, W. Doleschal, A. Gehner, W. Grundke, R. Melcher, J. Paufler, R. Seltmann, and G. Zimmer. Deformable micromirror devices as phase modulating high resolution light valves. In *Proceedings of the 1995 8th International Conference on Solid-State Sensors and Actuators and Eurosensors IX*, pages 301–304. IEEE, Piscataway, 25-29 Jun. 1995.
- 3.20 X. Zhang, X.N. Jiang, and C. Sun. Microstereolithography of polymeric and ceramic microstructures. *Sensors and Actuators*, A77(2):149–156, 1999.

- 3.21 T. Nakamoto, K. Yamaguchi, P.A. Abraha, and K. Mishima. Manufacturing of three-dimensional micro-parts by UV laser induced polymerisation. *J. Micromech. Microeng.*, 6:240–253, 1996.
- 3.22 K. Ikuta and K. Hirowatari. Real three dimensional micro fabrication using stereo lithography and metal molding. In *Proceedings of the 1993 IEEE Micro Electro Mechanical Systems*, pages 42–47, Fort Lauderdale, Feb. 7-10 1993.
- 3.23 C. Tille, R. Deuke, and R. Eidam. Manufacturing high resolution parts with stereolithography method. In D.L. Bourell, editor, *Solid Freeform Fabrication Symposium 1999*, pages 849–856, University of Texas, Austin, August 9-11 1999.
- 3.24 U. Stute, J. Serbin, C. Kulik, and B.N. Chichkov. Three-dimensional nanostructures fabricated by two-photon polymerization of hybrid polymers. In P. Bartolo and G. Mitchel et al, editors, *Proceedings of the first international conference on advanced research in virtual and rapid prototyping*, pages 399–403, Leiria, Portugal, 2003.
- 3.25 S.M. Kuebler, S.P. Ananthavel, M. Rumi, S.R. Marder, J.W. Perry, S. Barlow, B.H. Cumpston, D.L. Dyer, J.E. Ehrlich, L.L. Erskine, A.A. Heikal, I.-Y.S. Lee, D. McCord-Maughon, J. Qin, H. Röckel, and X.-L. Wu. Two-photon polymerization initiators for efficient three-dimensional data storage and microfabrication. In *Proceedings of the 1999 Quantum Electronics and Laser Science Conference (QELS '99)*, page 52. IEEE, Piscataway, May 23-28 1999.
- 3.26 B.H. Cumpston, S.P. Ananthavel, S. Barlow, D.L. Dyer, J.E. Ehrlich, L.L. Erskine, A.A. Heikal, S.M. Kuebler, I.-Y.S. Lee, D. McCord-Maughon, J. Qin, H. Röckel, M. Rumi, X.-L. Wu, S.R. Marder, and J.W. Perry. Two-photon polymerization initiators for three-dimensional optical data storage and microfabrication. *Nature*, 398:51–54, 1999.
- 3.27 F. Korte, J. Serbin, J. Koch, A. Egbert, C. Fallnich, A. Ostendorf, and B.N. Chichkov. Towards nanostructuring with femtosecond laser pulses. *Applied Physics A: Materials Science and Processing*, 77(2):229–235, 2003.
- 3.28 J. Serbin, A. Egbert, A. Ostendorf, B.N. Chichkov, R. Houbertz, G. Domann, J. Schulz, C. Cronauer, L. Frohlich, and M. Popall. Femtosecond laser-induced two-photon polymerization of inorganic-organic hybrid materials for applications in photonics. *Optics Letters*, 28(5):301–303, 2003.
- 3.29 S. Kirihaara, M.W. Takeda, K. Sakoda, and Y. Miyamoto. Fabrication of three-dimensional photonic crystals with diamond structure by stereolithography. In P. Bartolo and G. Mitchel et al, editors, *Proceedings of the first international conference on advanced research in virtual and rapid prototyping*, pages 283–288, Leiria, Portugal, 2003.
- 3.30 G.A. Brady, T.-M. Chu, and J.W. Halloran. Curing behavior of ceramic resins for stereolithography. In D.L. Bourell et al., editor, *Solid Freeform Fabrication Symposium 1996*, pages 403–410, University of Texas, Austin, August 12-14 1996.

- 3.31 G. A. Brady and J. W. Halloran. Solid freeform fabrication of ceramics via stereolithography. *Naval Research Reviews*, L(3):39–43, 1998.
- 3.32 W. Zimbeck, M. Pope, and R.W. Rice. Microstructures and strengths of metals and ceramics made by photopolymer-based Rapid Prototyping. In D.L. Bourell et al., editor, *Solid Freeform Fabrication Symposium 1996*, pages 403–410, University of Texas, Austin, August 12-14 1996.
- 3.33 S. Ventura, S. Narang, P. Guerit, S. Liu, D. Twait, P. Khandelwal, and E. Cohen. Solid freeform fabrication and design. In *24th Annual Conference on Composites, Advanced Ceramics, Materials, and Structures: B*, volume 21 of *Ceramic Engineering and Science Proceedings*, pages 111–119. American Ceramic Soc, Westerville, Ohio, Cocoa Beach, Jan. 23-28 2000.
- 3.34 A.-M. Clarinval, R. Carrus, and T. Dormal. Development of material fo Optoform process. In P. Bartolo and G. Mitchel et al, editors, *Proceedings of the first international conference on advanced research in virtual and rapid prototyping*, pages 279–282, Leiria, Portugal, 2003.
- 3.35 J.W. Schultz and R.P. Chartoff. Photopolymerization of nematic liquid crystal monomers for structural applications: molecular order and orientation dynamics. *Polymer*, 39(2):319–325, 1998.
- 3.36 J.S. Ullett, J.W. Schultz, and R.P. Chartoff. Novel liquid crystal resins for stereolithography: processing parameters and mechanical analysis. *Rapid Prototyping Journal*, 6(1):8–17, 2000.
- 3.37 J.S. Ullett, J.W. Schultz, T. Benson-Tolle, and R.P. Chartoff. Thermal-expansion and fracture properties of parts made from liquid crystal stereolithography resins. *Materials and Design*, 20(2):91–97, 1999.
- 3.38 C. Wilkening. Fast production of technical prototypes using direct laser sintering of metals and foundry sand. In D. Bourell et al., editor, *Proceedings of the Solid Freeform Fabrication Symposium 1996*, pages 133–140, University of Texas, Austin, August 12-14 1996.
- 3.39 R. Merz, F.B. Prinz, K. Ramaswami, M. Terk, and L. Weiss. Shape deposition manufacturing. In H.L. Marcus et al., editor, *Proceedings of the Solid Freeform Fabrication Symposium 1994*, pages 1–8, University of Texas, Austin, August 8-10 1994.
- 3.40 B. Badrinarayan and J.W. Barlow. Effect of processing parameters in SLS of metal-polymer powders. In H.L. Marcus et al., editor, *Proceedings of the Solid Freeform Fabrication Symposium 1995*, pages 55–63, University of Texas, Austin, August 7-9 1995.
- 3.41 J.C. Nelson. *Selective Laser Sintering: A definition of the process and an empirical sintering model*. PhD thesis, The University of Texas at Austin, 1993.
- 3.42 P.K. Subramanian, J.W. Barlow, and H.L. Marcus. Effect of particle size on SLS and post-processing of alumina with polymer binders. In H.L. Marcus et al.,

- editor, *Proceedings of the Solid Freeform Fabrication Symposium 1995*, pages 346–352, University of Texas, Austin, August 7-9 1995.
- 3.43 F.B. Prinz, L.E. Weiss, C.H. Amon, and J.L. Beuth. Processing, thermal and mechanical issues in Sape Deposition Manufacturing. In H.L. Marcus et al., editor, *Proceedings of the Solid Freeform Fabrication Symposium 1995*, pages 118–129, University of Texas, Austin, August 7-9 1995.
- 3.44 M.L. Griffith, M.E. Schlienger, L.D. Harwell, M.S. Oliver, M.D. Baldwin, M.T. Ensz, J.E. Smugeresky, M. Essien, J. Brooks, C.V. Robino, W.H. Hofmeister, M.J. Wert, and D.V. Nelson. Thermal behavior in the LENS process. In D.L. Bourell et al., editor, *Solid Freeform Fabrication Symposium 1998*, pages 89–96, University of Texas, Austin, August 10-12 1998.
- 3.45 G. Link. *Layered manufacturing of laser deposited carbon steels*. PhD thesis, Stanford University, 1999.
- 3.46 J. Hänninen. Direct metal laser sintering. *Advanced Materials and Processes*, 160(5):33–36, 2002.
- 3.47 S. Das, M. Wohler, J.L. Beaman, and D.L. Bourell. Processing of titanium net shapes by SLS/HIP. In D.L. Bourell et al., editor, *Solid Freeform Fabrication Symposium 1998*, pages 469–477, University of Texas, Austin, August 10-12 1998.
- 3.48 B. Engel and D.L. Bourell. Titanium alloy powder preparation for selective laser sintering. *Rapid Prototyping Journal*, 6(2):97–106, 2000.
- 3.49 J.R. Fessler, A.H. Nickel, G. Link, F.B. Prinz, and P. Fussell. Functional gradient metallic prototypes through Shape Deposition Manufacturing. In D.L. Bourell et al., editor, *Solid Freeform Fabrication Symposium 1997*, pages 521–528, University of Texas, Austin, August 1997.
- 3.50 J.-H. Kao. *Process planning for additive/subtractive freeform fabrication using medial axis transform*. PhD thesis, Stanford University, 1999.
- 3.51 A. Nickel. *Analysis of thermal stresses in Shape Deposition Manufacturing of metal parts*. PhD thesis, Stanford University, 1999.
- 3.52 E. Sachs, M. Cima, P. Williams, D. Brancazio, and J. Cornie. Three dimensional printing. rapid tooling and prototypes directly from a cad model. *Journal of Engineering for Industry*, 114(4):481–488, 1993.
- 3.53 E. Sachs et al. Three-dimensional printing techniques. International Patent WO 93/25336, 1993.
- 3.54 S.E. burns, P.Cain, J. Mills, J. Wang, and H. Siringhaus. Inkjet printing of polymer thin-film transistor circuits. *MRS Bulletin*, 28(11):829–834, 2003.
- 3.55 Y. Yoshioka, G. Jabbour, and P. Calvert. Multilayer inkjet printing of materials. In *Nanoscale Optics and Applications*, volume 4809 of *Proceedings of SPIE - The International Society for Optical Engineering*, pages 164–169, Jul 8-9, Seattle 2002.

- 3.56 B. Derby and N. Reis. Inkjet printing of highly loaded particulate suspensions. *MRS Bulletin*, 28(11):815–818, 2003.
- 3.57 L.T. Creagh and M. McDonald. Design and performance of inkjet print heads for non-graphic-arts applications. *MRS Bulletin*, 28(11):807–811, 2003.
- 3.58 T. Clay and T. Krouth. Direct metal casting. *Advanced Materials and Processes*, 161(1):43–44, 2003.
- 3.59 D. Cebon, M.F. Ashby, and L. Lee-Shothaman. *Cambridge Engineering Selector V 3.1*. Granta Design Ltd., 2000.
- 3.60 J. Wirth. *Rapid Modeling*. Hanser Fachbuch, München, 2002.
- 3.61 A.G. Cooper, S. Kang, J.W. Kietzman, F.B. Prinz, J.L. Lombardi, and L.E. Weiss. Automated fabrication of complex molded parts using Mold Shape Deposition Manufacturing. *Materials and Design*, 20(2/3):83–89, 1999.
- 3.62 J. Kietzman, B.-H. Park, and F. Prinz. Part strength improvement in polymer shape deposition manufacturing. *Rapid Prototyping Journal*, 7(3):130–137, 2001.
- 3.63 F.B. Prinz, A. Golnas, and A. Nickel. Does integrated-circuit fabrication show the path for the future of mechanical manufacturing? *MRS Bulletin*, 25(10):32–35, 2000.
- 3.64 K.G. Cooper. *Rapid Prototyping technology*. Marcel Dekker, 2001.
- 3.65 M.F. Ashby, editor. *Materials selection in mechanical design*. Butterworth-Heinemann, Oxford, 2 edition, 1999.

Cellular solids form the basis of many structural as well as functional materials. Applications in engineering include packaging, lightweight-structures [4.1, 4.2] and photonic crystals. Cellular materials are also common in nature [4.3] where their properties are evolutionary tailored according to the natural environment. The molecular building blocks of these biological cellular solids are usually very simple, but by arranging these building blocks on multiple hierarchies, extremely complex and mechanically efficient materials-structures can be obtained.

Cellular solids typically exhibit very complex geometries with severe undercuts. Currently, cellular solids for engineering applications are obtained by foaming a liquid with a gaseous foaming agent. After the liquid has solidified, a solid cellular material with usually random cell distribution is obtained. In contrast to these foaming techniques, RP offers the possibility to define and fabricate cellular structures with defined internal and external geometry. Furthermore, recently developed techniques enable the fabrication of complex structures with very small feature resolution. Microstereolithography for instance enables the user to fabricate parts with feature resolutions in the range of 5-10  $\mu\text{m}$  [4.4, 4.5]. Another order of magnitude in resolution can be gained by using two-photon lithography [4.6–4.9] (see also Sec. 3.1.1.3).

It can be expected that these techniques will have significant impact in the development of materials for optoelectronic and biomedical applications. The following two sections will give a short overview of the state of the art in this field.

## 4.1 Cellular structures for photonic crystals

---

Photonic crystals [4.10, 4.11] are a class of materials with exceptional optical properties that make them interesting as base materials for applications in telecommunication and optical computing. The geometrical basis of these materials is a periodic (two- or three-dimensional) lattice whose lattice constant is in the order of the wavelength of the incident light. The geometry of the utilized lattices can be very complex, a fact which makes RP an interesting manufacturing technique for such materials. Stereolithography has been used to fabricate ceramic photonic crystals for microwave applications [4.12]. For shorter wavelengths, where even smaller features are required, two-photon lithography will be an [4.7] option. Alternatively, techniques like Robocasting have also been investigated [4.13].

## 4.2 Cellular materials for biomedical applications

---

Many biological materials (e.g. wood, cork, bone,...) are cellular, since cellular architectures offer the possibility to optimize the properties (stiffness, density, strength, ..) of a structure according to the environmental conditions. By using Rapid Prototyping it is possible to fabricate cellular materials on a similar size scale like in natural material-structures. By using appropriate moulding techniques, these structures can be fabricated out of a wide variety of materials (polymers, ceramics [4.2, 4.14–4.16], composites) which are compatible with requirements in biomaterials science [4.17]. Cellular materials for biomedical applications offer several advantages compared to bulk biomaterials:

- By tuning the porosity of the material, the stiffness of the cellular structure can be tailored to match the stiffness of the surrounding tissue. Large differences in material moduli [4.18] can lead to degradation of surrounding tissue and to material failure at the interfaces between the two materials.
- Artificial cellular structures used in, for instance, tissue engineering [4.19], resemble their natural counterparts, and therefore offer more opportunities to achieve a high degree of biocompatibility. Seed cells can settle more easily in an open, foam-like structure than on a solid block of material. The high surface area of a cellular structure can be used to tailor the degradation rate of biodegradable materials and the culture medium can more easily access all regions inside the structure.

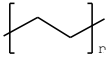
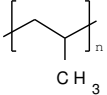
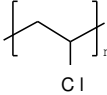
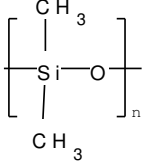
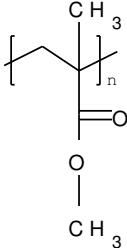
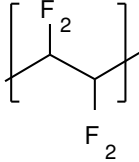
### 4.2.1 Requirements for RP processes

If RP is to be considered as manufacturing tool for cellular structures, each possible process has to be evaluated regarding the following issues (see also Chap. 9):

- Cellular structures exhibit significantly undercut features. The utilized process must be able to shape such features. This requirement is especially critical for processes which rely on support structures that have to be removed mechanically (e.g. stereolithography). Since the overhangs within cellular structures cannot be reached mechanically, internal undercuts must be manufacturable without support. Processes which work without support structures (e.g. SLS, 3DP, ..) or with wash-away support (FDM) are advantageous in this respect.
- For many biomedical applications a fairly high accuracy is demanded (e.g. fitting tolerances for implants). The utilized RP process has to meet these requirements.

## 4.2. CELLULAR MATERIALS FOR BIOMEDICAL APPLICATIONS

**Tab. 4.1.** Classification of biomaterials. Direct RP processes are in **bold**, indirect processes in *italic*

Material	Formula	abbrev.	typical application	RP processes
<b>Biocompatible materials</b>				
<b>Metals</b>				
titanium	Ti		implants	<b>SLS</b> , <i>investment casting</i>
stainless steel				<b>SLS</b>
CoCr-alloys				
<b>Ceramics</b>				
alumina	Al <sub>2</sub> O <sub>3</sub>		orthopedic load bearing applications, coatings	<b>SLS, SLA, FDM</b> , <i>gelcasting</i>
zirconia	ZrO <sub>2</sub>		hip prostheses	<b>SLS, SLA, FDM</b> , <i>gelcasting</i>
<b>Polymer</b>				
polyethylene		PE	acetabular components in artificial hips, syringes	
polypropylene		PP	heart valves, sutures	
poly(vinyl chloride)		PVC	tubings, packaging	
polyamide		PA	sutures, syringes	<b>SLS</b> , <i>vacuum casting</i>
poly(dimethyl siloxane)		PDMS	breast implants, plastic surgery, tubings, artificial skin	<i>vacuum casting</i>
poly(methyl methacrylate)		PMMA	hard contact lenses	
poly(tetrafluoroethylene)		PTFE	implants	
poly(ethylene terephthalate)		PET	artificial blood vessels	

**Tab. 4.2.** Classification of biomaterials (continued). Direct RP processes are in **bold**, indirect processes in *italic*

Material	Formula	abbrev.	typical application	RP processes
<b>Biodegradable materials</b>				
<b>Polymers</b>				
polyglycolide		PGA	bone plates	<b>FDM</b>
poly(L-lactide)		PLA (poly-lactic acid)	sutures, fixation plates, screws	<b>FDM, 3DP</b>
poly(ε-caprolactone)		PCL		<b>FDM</b>
poly(p-dioxanone)				
polypeptides				
polyanhydrides				
<b>Bioresorbable materials</b>				
<b>Polymers</b>				
chitin				
chitosan			contact lenses, controlled release systems, artificial blood vessels, artificial skin	<b>FDM, Modelmaker, vacuum casting</b>
collagene			artificial blood vessels, membranes, cornea-implants	
<b>Ceramics</b>				
hydroxyapatite	Ca <sub>10</sub> (PO <sub>4</sub> ) <sub>6</sub> (OH) <sub>2</sub>	HA	bone replacement material	<b>FDM, SLA, Modelmaker, gelcasting</b>
beta-tricalcium phosphate	Ca <sub>3</sub> (PO <sub>4</sub> ) <sub>6</sub>	TCP	see HA	
bio-glasses	P <sub>2</sub> O <sub>5</sub> -CaO-Na <sub>2</sub> O-systems			

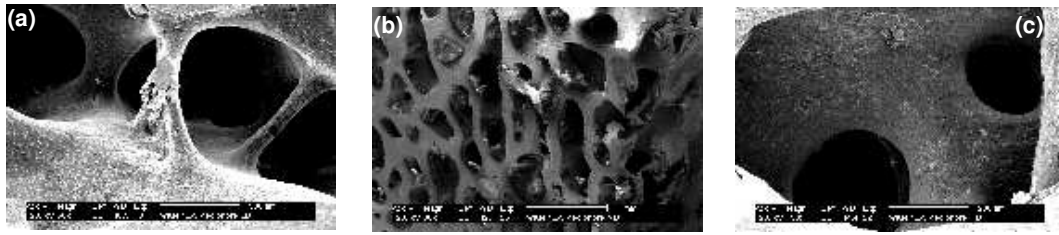


**Figure 4.1:** Scanning electron micrograph of trabecular bone.

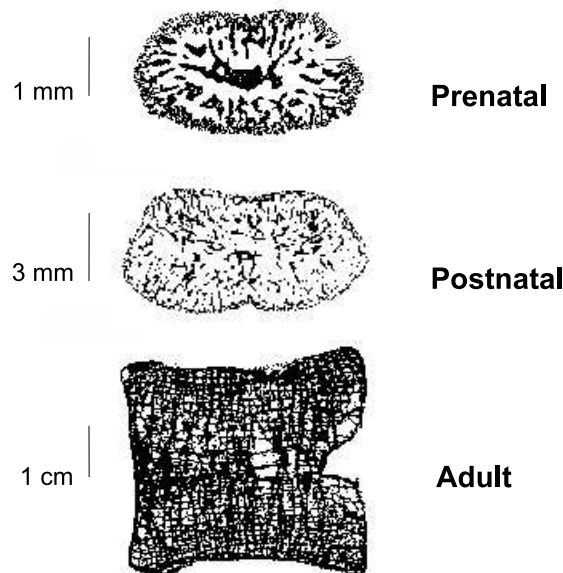


**Figure 4.2:** Architecture of the human vertebral body depending on age. In the embryo the arrangement of the trabecula is radial, in the adult horizontal-vertical, according to the direction of the applied loads [4.20].

- Especially for cellular solids, the required features sizes are very small. Ideally, the final structure should be a one-to-one copy of the natural counterpart (see Fig. 4.1 and Fig. 4.2). If, for instance, scaffolds for bone tissue engineering have to be fabricated, features below 0.5 mm have to be manufactured [4.21–4.23]. Osteoblasts, the bone forming cells, like to grow in pores whose diameter roughly corresponds to the pore sizes found in trabecular bone. Some RP processes like stereolithography are already able to reach these resolutions, and therefore a fairly large number of investigations are dealing with the fabrication of scaffolds for bone tissue engineering. For the cultivation of other cell types, e.g. chondrocytes [4.24] or hepatocytes, even smaller pores are required.
- Most of the currently available RP processes cannot directly shape biomaterials. It is therefore necessary to use a two-step process to obtain the final structure: In a first step RP is used to shape a sacrificial part. This sacrificial shape is then molded with the appropriate material. In Tab. 4.1 and Tab. 4.2 the most commonly used biomaterials are listed, together with RP-methods which are suitable to shape them.

As can be seen from Tab. 4.1 and Tab. 4.2, several RP processes have been investigated regarding their suitability for shaping biomaterials. Besides well established applications (e.g. pre-operative planning, drilling-templates for dental surgery, master patterns for fixation plates, silicone structures [4.25], ...), applications of cellular biomaterials shaped by RP are currently mostly in a research state. Most of the currently available techniques have been investigated regarding their suitability for shaping cellular structures. FDM [4.26–4.28] can be used for directly shaping thermoplastic biodegradable materials, ceramic-polymeric composites or ceramic green parts. SLA has been used to shape moulds for indirect processes [4.15], see also Chap. 9.

Using dispensing systems [4.29–4.31], it is possible to deposit complex, thermally sensitive materials as well as living cells. These systems offer a great degree of freedom regarding materials, they can dispense multiple materials in the same part, but they operate only sequentially and are therefore quite slow.

Fairly advanced are systems based on 3DP [4.32] which use biodegradable powders which are fused together. Some of the efforts in using 3DP have been commercialized by Therics Inc., who developed the TheriForm process which is based on 3DP [4.33].

## 4.2.2 Applications

Commercial products, which are based on cellular structures made by RP, are already available. One example are vertebral body replacements out of titanium (see Fig. 4.3). These structures are made by using a wax-part (fabricated by utilizing a Protoscape Modelmaker) as lost pattern for investment casting of titanium. These structures exhibit excellent stiffness and strength while maintaining a low weight.



**Figure 4.3:** Interpore Cross (Irvine, California) produces these cellular structures out of titanium as vertebral body replacement device [4.34].

Another application which is pursued in several research projects is the fabrication of scaffolding materials for bone tissue regeneration (see Fig. 4.4). Some of the mechan-

ical and materials issues regarding this application are discussed in Chap. 8 and 9.

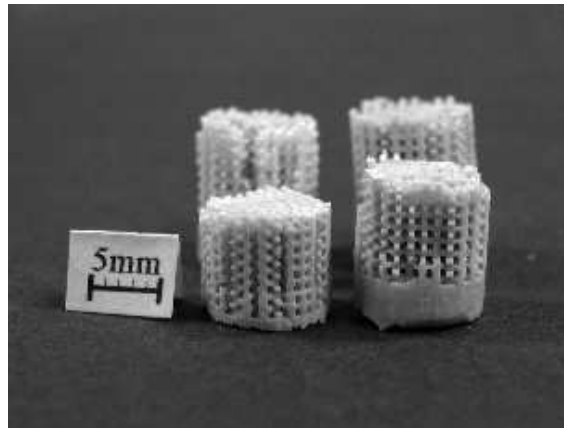


**Figure 4.4:** Ceramic (hydroxyapatite) cellular structure made by molding a photopolymer-scaffold with gelcasting.

## 4.3 References

- 4.1 L.J. Gibson and M.F. Ashby. *Cellular solids*. Cambridge University Press, second edition, 1997.
- 4.2 W.Frieß and J. Warner. Biomedical applications. In Schüth et al. [4.35], pages 2923–2970.
- 4.3 G. Jeronimidis. Structure-property relationship in biological materials. In M. Elices, editor, *Structural biological materials*, chapter 1, pages 3–18. Pergamon, 2000.
- 4.4 A. Bertsch, S. Zissi, J.Y. Jezequel, S. Corbel, and J.C. André. Microstereolithography using a liquid crystal display as dynamic mask-generator. *Microsystem Technologies*, 3(2):42–47, 1997.
- 4.5 T. Nakamoto, K. Yamaguchi, P.A. Abraha, and K. Mishima. Manufacturing of three-dimensional micro-parts by UV laser induced polymerisation. *J. Micromech. Microeng.*, 6:240–253, 1996.
- 4.6 S. Kawata, H.-B. Sun, T. Tanaka, and K. Takada. Finer features for functional microdevices. *Nature*, 412:697–698, 2001.
- 4.7 U. Stute, J. Serbin, C. Kulik, and B.N. Chichkov. Three-dimensional nanostructures fabricated by two-photon polymerization of hybrid polymers. In P. Bartolo and G. Mitchel et al, editors, *Proceedings of the first international conference on advanced research in virtual and rapid prototyping*, pages 399–403, Leiria, Portugal, 2003.
- 4.8 J. Serbin, A. Egbert, A. Ostendorf, B.N. Chichkov, R. Houbertz, G. Domann, J. Schulz, C. Cronauer, L. Frohlich, and M. Popall. Femtosecond laser-induced two-photon polymerization of inorganic-organic hybrid materials for applications in photonics. *Optics Letters*, 28(5):301–303, 2003.

- 4.9 B.H. Cumpston, S.P. Ananthavel, S. Barlow, D.L. Dyer, J.E. Ehrlich, L.L. Erskine, A.A. Heikal, S.M. Kuebler, I.-Y.S. Lee, D. McCord-Maughon, J. Qin, H. Röckel, M. Rumi, X.-L. Wu, S.R. Marder, and J.W. Perry. Two-photon polymerization initiators for three-dimensional optical data storage and microfabrication. *Nature*, 398:51–54, 1999.
- 4.10 E. Yablonovitch. Inhibited spontaneous emission in solid-state physics and electronics. *Phys.Rev.Lett.*, 58:2059, 1987.
- 4.11 S. John. Strong localization of photons in certain disordered dielectric superlattices. *Phys.Rev.Lett.*, 58:2486, 1987.
- 4.12 S. Kirihaara, M.W. Takeda, K. Sakoda, and Y. Miyamoto. Fabrication of three-dimensional photonic crystals with diamond structure by stereolithography. In P. Bartolo and G. Mitchel et al, editors, *Proceedings of the first international conference on advanced research in virtual and rapid prototyping*, pages 283–288, Leiria, Portugal, 2003.
- 4.13 P.G. Clem, J.F. Carroll, M.K. Niehaus, J. Cesarano, J.E. Smay, J.A. Lewis, and S.-Y. Lin. Materials for freedom fabrication of GHz tunable dielectric photonic crystals. In *Rapid Prototyping Technologies*, volume 758 of *Proceedings Materials Research Society Symposium*, pages 41–46, 2003.
- 4.14 E. Charrière, J. Lemaitre, and Ph. Zysset. Hydroxyapatite cement scaffolds with controlled macroporosity: fabrication protocol and mechanical properties. *Biomaterials*, 24:809–817, 2003.
- 4.15 J. Stampfl, R. Cano Vives, S. Seidler, R. Liska, F. Schwager, H. Gruber, A. Wöß, and P. Fratzl. Rapid prototyping - a route for the fabrication of biomimetic cellular materials. In P.J. Bartolo, G. Mitchell, et al., editors, *Advanced Research in Virtual and Rapid Prototyping*, Proceedings VRAP 2003, Leiria, pages 659–666. ESTG, 2003.
- 4.16 R.Z. LeGeros and J.P. LeGeros. Dense hydroxyapatite. In L.L. Hench and J. Wilson, editors, *An introduction to bioceramics*, volume 1 of *Advanced Series in Bioceramics*, pages 139–157. World Scientific, 1993.
- 4.17 B.D. Ratner, A.S. Hoffman, F.J. Schoen, and J.E. Lemons. *Biomaterials science*. Academic Press, 1996.
- 4.18 L.M. Milkowski, V.R. Gervasi, S. Kumaresan, and R.S. Crockett. Development of a mechanically similar composite bone replica. volume 1 of *Proceedings of the Annual International Conference of the IEEE Engineering in Medicine and Biology*, pages 329–341, 1999.
- 4.19 W. Sun, A. Darling, B. Starly, and J. Nam. Computer-aided tissue engineering: overview, scope and challenges. *Biotechnol. Appl. Biochem.*, 39:29–47, 2004.
- 4.20 P. Roschger, B.M. Grabner, S. Rinnerthaler, W. Tesch, M. Kneissel, A. Berzlanovich, K. Klaushofer, and P. Fratzl. Structural development of the mineralized tissue in the human L4 vertebral body. *Journal of Structural Biology*, 136:126–136, 2001.

- 4.21 J.M. Karp, P.D. Dalton, and M.S. Shoichet. Scaffolds for tissue engineering. *MRS Bulletin*, April:301–305, 2003.
- 4.22 K.F. Leong, C.M. Cheah, and C.K. Chua. Solid freeform fabrication of three-dimensional scaffolds for engineering replacement of tissues and organs. *Bio-materials*, 24:2363–2378, 2003.
- 4.23 S. Limpanuphap and B. Derby. Manufacture of biomaterials by a novel printing process. *J. Materials Science: Materials in Medicine*, 13:1163–1166, 2002.
- 4.24 W. Kafienah, M. Jakob, O. Demartean, A. Frazer, M.D. Barker, I. Martin, and A.P. Hollander. Three-dimensional tissue engineering of hyaline cartilage: Comparison of adult nasal and articular chondrocytes. *Tissue engineering*, 8(5):817–826, 2003.
- 4.25 R. Sodian, M. Löbe, A. Hein, D.P. Martin, S.P. Hörstrup, E.V. Potapov, H. Hausmann, T. Lüth, and R. Hetzer. Application of stereolithography for scaffold fabrication for tissue engineered heart valves. *American Society for Artificial Internal Organs Journal*, 48(1):12–16, 2002.
- 4.26 R.K. Panda, P. Teung, S.C. Danforth, and A. Safari. Fabrication of calcium phosphate based ceramics with controlled porosity for bone scaffolds. In R.Z. Le Geros and J.P. Le Geros, editors, *Bioceramics Vol. 11*, Proceeding of the 11th International Symposium on Ceramics in Medicine, pages 727–730, 1998.
- 4.27 T. Cao, K.-H. Ho, and S.-H. Teoh. Scaffold design and in vitro study of osteochondral coculture in a three-dimensional porous polycaprolactone scaffold fabricated by fused deposition modeling. *Tissue engineering*, 9(4):103–112, 2003.
- 4.28 D.W. Hutmacher. Scaffold design and fabrication technologies for engineering tissues - state-of-the-art and future perspectives. *J. Biomaterials Science - polymer edition*, 12(1):107–124, 2001.
- 4.29 L. Geng, Y.S. Wong, D.W. Hutmacher, W. Feng, H.T. Loh, and J.Y.H. Fuh. Rapid prototyping of 3d scaffolds for tissue engineering using a four-axis multiple-dispenser robotic system. In D.L. Bourell, editor, *Solid Freeform Fabrication Symposium 2003*, pages 423–432, University of Texas, Austin, 2003.
- 4.30 T.H. Ang, F.S.A. Sultana, D.W. Hutmacher, Y.S. Wong, J.Y.H. Fuh, X.M. Mo, H.T. Loh, E. Burdet, and S.H. Teoh. Fabrication of 3D chitosan-hydroxyapatite scaffolds using a robotic dispensing system. *Materials Science and Engineering C*, 20:35–42, 2002.
- 4.31 R.C.Y. Auyeung, B.R. Ringeisen, H. Kim, H.D. Young, B.J. Spargo, A. Pique, D. Chrisey, and P.K. Wu. Cell-by-cell construction of living tissue. In *Electroactive Polymers and Rapid Prototyping*, volume 698 of *Proceedings Materials Research Society Symposium*, pages 329–341, 2002.
- 4.32 C.X.F. Lam, X.M. Mo, S.H. Teoh, and D.W. Hutmacher. Scaffold development using 3D printing with a starch-based polymer. *Mater.Sci.Eng.*, C20:49–56, 2002.

- 4.33 J. Zeltinger, J. Sherwood, D.A. Graham, R. Mueller, and L.G. Griffith. Effect of pore size and void fraction on cellular adhesion, proliferation and matrix deposition. *Tissue Engineering*, 7:575–572, 2001.
- 4.34 Revolutionary implants from rapid prototyping. <http://www.cadcamnet.com>, 2003.
- 4.35 F. Schüth, K.S.W. Sing, and J. Weitkamp, editors. *Handbook of porous solids*. Wiley-VCH, 2002.

## **Part II**

### **Original papers**



---

# THE SEPARATION OF THE FRACTURE ENERGY IN METALLIC MATERIALS

**J. Stampfl, O. Kolednik**

*International Journal of Fracture* 101(4):321-345, 2000

**Abstract.** The total plastic strain energy which is consumed during fracture of a plain-sided CT specimen is separated into several components. These are the energies required for deforming the specimen until the point of fracture initiation, for forming the flat-fracture surfaces, for forming the shear-lip fracture surfaces, and for the lateral contraction and the blunting at the side-surfaces,  $W_{lat}$ . Characteristic crack growth resistance terms,  $R_{flat}$  and  $R_{slant}$ , are determined describing the energies dissipated in a unit area of flat-fracture and slant-fracture surface, respectively.  $R_{flat}$  is further subdivided into the term  $R_{surf}$ , to form the micro-ductile fracture surface, and into the subsurface term,  $R_{sub}$ , which produces the global crack opening angle.

Two different approaches are used to determine the fracture energy components. The first approach is a single-specimen technique for recording the total crack growth resistance (also called energy dissipation rate). Plain-sided and side-grooved specimens are tested. The second approach rests on the fact that the local plastic deformation energy can be evaluated from the shape of the fracture surfaces. A digital image analysis system is used to generate height models from stereophotograms of corresponding fracture surface regions on the two specimen halves.

Two materials are investigated: a solution annealed maraging steel V 720 and a nitrogen alloyed ferritic-austenitic duplex steel A 905. For the steel V 720 the following values are measured:  $J_i = 65 \text{ kJ/m}^2$ ,  $R_{surf} = 20 \text{ kJ/m}^2$ ,  $R_{flat} = 280 \text{ kJ/m}^2$ ,  $R_{slant} = 1000 \text{ kJ/m}^2$ ,  $W_{lat} = 30 \text{ J}$ . For the steel A 905 which has no shear lips, the measured values are:  $J_i = 190 \text{ kJ/m}^2$ ,  $R_{flat} = 1000 \text{ kJ/m}^2$ , and  $W_{lat} = 45 \text{ J}$ . Apart from materials characterization, these values could be useful for predicting the influence of specimen geometry and size on the crack growth resistance curves.

## 5.1 Introduction

The crack growth resistance of a material depends on the total amount of non-reversible energy which is consumed during a fracture process. In fracture mechanics tests it is often observed that the crack growth resistance depends on the geometry and the size of the specimen (e.g., see [5.1] for an outline of the problem). This effect is noticed for a wide class of low-strength or medium-strength engineering materials where a large plastic zone accompanies the crack tip during crack propagation, i.e. for fracture under large-scale yielding (lsy) or general yielding (gy) conditions. Even if the consideration is confined to deeply notched bend-type specimen, the influence of geometry is significant.

As a consequence of these observations, two fundamental questions appear. The first question is: How can the crack growth resistance of these materials be characterized? The second question, in the literature referred to as “transferability problem”, is: How can fracture toughness data, that are measured on a specific specimen, be transferred to specimens of other geometries or to a structural component of arbitrary shape? Both questions have yet to be resolved.

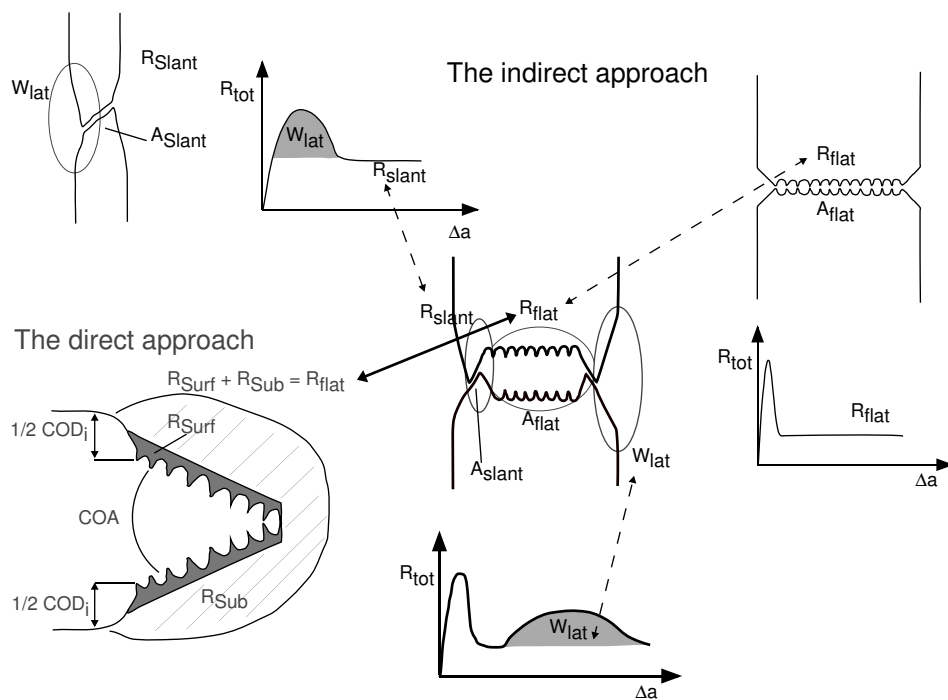


**Figure 5.1:** A schematic view of the indirect and the direct approach to separate the fracture energies.

The geometry problem occurs because the local fracture properties of materials depend on the constraint. Different constraint measures have been introduced in the literature [5.2–5.6]. In the low-constraint near-side-surface regions of a deeply notched bend-type specimen the material behaves tougher than in the high-constraint mid-section region. Usually, this behavior is reflected in the fracture surface appearance:

we see a flat-fracture mid-section region accompanied by two shear lip regions with slant fracture surfaces near the side surfaces. The global fracture properties of the material result as a complicated interplay of all the different constraint conditions along the crack front [5.7].

A promising way to resolve the geometry problem would be to separate the total plastically deformed region into several characteristic parts and to predict the amount of the plastic strain energy dissipated in each part. By doing this, we can extract a value of the crack growth resistance for the high-constraint region, that might be characteristic for the material. (Another characteristic value, for the low-constraint region directly near the side-surface, might exist, too.) This would answer the first question posed, and it would be also an important step towards solving the transferability problem.

For a separation to be successful, it is not only necessary that it is clearly defined and conceptually feasible; it is also strongly desired that the amount of plastic strain energy consumed in each part can be determined experimentally. Existing theories about the geometry influence on the crack growth resistance, [5.1–5.3, 5.5, 5.6, 5.8–5.10], could not be proved and new, improved theories could not be derived, otherwise. To the knowledge of the authors no such separation has been reported so far. (A short literature survey will be given below.)

We will demonstrate in this study that it is possible to separate the total plastic strain energy for the fracture of Compact Tension specimens made of two different steels in a reasonable way and to measure all the energy components. The general outline of the procedure is shown in Fig. 5.1. Two different approaches are used. The first approach is an indirect one: different fracture mechanics experiments are designed so that a careful analysis allows the separation of the total fracture energy into several characteristic parts. The second approach is a more direct one: the local plastic deformation energy is estimated from the topography of the fracture surfaces. Plastic deformation during fracture produces a misfit between corresponding fracture surface regions on both parts of the broken specimen, which can be analyzed to determine the locally dissipated plastic strain energy.

The combination of both approaches could be a powerful means towards a solution of the geometry problem.

## 5.2 A Brief Literature Survey

---

### 5.2.1 The definition of the total crack growth resistance

The total crack growth resistance,  $R_{\text{tot}}$ , of a material can be defined as total non-reversible energy which is necessary to extend the crack area by an increment, see Turner and Kolednik [5.11],

$$R_{\text{tot}} \equiv \frac{1}{B} \frac{d}{d(\Delta a)} (W_{\text{pl,tot}} + \Gamma). \quad (5.1)$$

$W_{pl,tot}$  denotes the total non-reversible strain energy consumed during the fracture process,  $\Gamma$  is the surface energy,  $\Delta a$  the crack extension and  $B$  the specimen thickness. For elastic ideally brittle materials,  $W_{pl,tot} = 0$  and  $R_{tot}$  reduces to the Griffith solution [5.12], i.e. to twice the specific surface energy,  $R_{tot,el} = 2\gamma_0$ . If plasticity were confined to a constant, narrow zone around the crack tip, the Orowan [5.13] and Irwin [5.14] approach of the existence of a specific non-linear fracture surface energy would be applicable:  $R_{tot,ssy} = 2(\gamma_0 + \gamma_{pl}) = const$ . The subscript “ssy” indicates that the confinement of the plastic zone must be even stronger than for small-scale yielding (ssy) conditions. For most elastic-plastic materials even for ssy-conditions the specific plastic strain energy for fracture exceeds the specific surface energy by several orders of magnitude,  $\gamma_{pl} \gg \gamma_0$ . It should be remarked that for micro-crack toughening, fiber reinforced, or transformation toughened materials with brittle matrices additional non-reversible energy terms appear, originating from processes other than plastic deformation, [5.15–5.17]. These energy terms must be included on the right-hand side of Eq. (5.1).

The total crack growth resistance,  $R_{tot}$ , was introduced by Turner [5.1]. He called  $R_{tot}$  the “energy dissipation rate”, symbolized by the letter  $D$ . This nomenclature might be somewhat misleading, because parts of the energies in Eq. (5.1) are not really dissipated during fracture [5.11]. Apart from the terms just mentioned above, these are the non-reversible elastic strain energy that originates due to the non-homogeneous crack-tip field, [5.18], and the surface energy.

Since some confusion seems to exist in the literature, a note regarding the reversibility of fracture energies is presented in Sec. 5.9. An important analysis on the thermodynamics of fracture was published by Gurney [5.19].

## 5.2.2 Some previous ideas on the separation of fracture energies

The idea of the separation of the fracture energies is not new. Cotterell and Reddel [5.20] performed fracture tests on thin double-edged notched panels with different ligament lengths. The total work of fracture was measured for each test and plotted against the ligament length. This diagram displayed a linear relationship. By extrapolating the linear regression line to zero ligament length, an “essential work of plane stress fracture” was determined, which depended on the specimen thickness. It was claimed that the essential work of fracture corresponds to the work done in the crack-tip region, distinct from the work done in the outer plastic regions. Based on the same idea, several other studies were performed later, e.g. [5.21, 5.22].

Turner [5.1], and John and Turner [5.23] discovered that resistance curves in terms of the total crack growth resistance, i.e.  $R_{tot}-\Delta a$ -curves, show typically a regime of steady-state growth after a short transition region of decreasing  $R_{tot}$ . They compared the curves for side-grooved and plain-sided specimens and attempted to break the steady-state value,  $R_{tot,ss}$ , into two [5.1] or three [5.9] components to find characteristic terms of dissipated energy per unit of crack area, or per unit of (shear-lip) volume. These terms, called “specific intensities of the rate of energy dissipation”

(SIREN), were then used to predict the resistance curves for other (bend-type) geometries. However the procedure has not been completely successful so far. One possible limitation was that only a multi-specimen method had been used to record the  $R_{tot}-\Delta a$ -curves, compared to the single-specimen technique applied in this investigation.

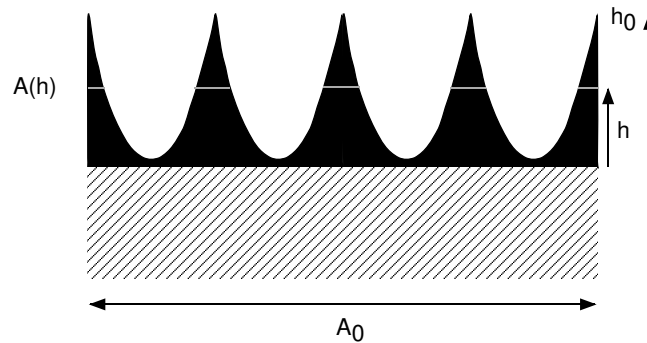


**Figure 5.2:** A schematic crosssection of a micro-ductile fracture surface to Stüwes model for the estimation of  $R_{surf}$

Another interesting approach was chosen by Shoji [5.24]: he sliced bend and CT specimens made of a bainitic steel perpendicular to the crack plane and measured the plastic strains near the fracture surfaces by applying a recrystallization-etch technique. The local plastic strain values were used to evaluate for the mid-section region the plastic strain energy within an intensely deformed region around the crack tip. This value was found to be independent of crack extension. A similar experiment, with specimens of different thicknesses, was conducted in [5.25].

Stüwe [5.26, 5.27] developed a model to estimate the specific plastic strain energy to form a micro-ductile fracture surface from the dimple height (see Fig. 5.2. A short description of the model will be given in Section 6.2. In [5.28] the fracture surface energy was determined for a maraging steel, similar to the one used in the current study. The dimple height was measured by stereophotogrammetric analyses of corresponding fracture surface regions on both specimen halves [5.29, 5.33].

Mecklenburg et al. [5.30] determined for three steels the rates of the elastic, the plastic, and the total strain energies versus the crack extension for side-grooved CT specimens. They observed that after a short crack extension a steady-state condition was reached. The sizes of the energy rates depended on the initial crack length and the specimen size.

## 5.3 The Total Plastic Strain Energy for Fracture and its Components

### 5.3.1 The different plastic strain energy terms

In a micro-ductile plane-strain fracture experiment (e.g., using a specimen with side grooves) plastic strain energy,  $W_{pl,surf}$ , is consumed to form the dimple structure of the fracture surfaces. This term is connected to the void growth and coalescence processes occurring within the process zone directly in front of the crack tip. For sssy-conditions,  $R_{surf} = W_{pl,surf}/(B\Delta a)$  will come close to the size of  $R_{tot,ssy}$ . In all other cases additional energy,  $W_{pl,sub}$ , is necessary for the deformation below the fracture surfaces. The sum of both, surface plus subsurface term, is the plastic energy for flat fracture,  $W_{pl,flat}$ .

To fracture a smooth-sided specimen (without side grooves)  $W_{pl,flat}$  is needed for the flat fracture regions in the center of the specimen.  $W_{pl,slant}$  shall denote the energy (surface plus subsurface) for producing the slant fracture of the shear lip regions near the side surfaces. Additional plastic energy is needed for the lateral contraction of the side surfaces and for the blunting process at the side surfaces, both combined in the term  $W_{pl,lat}$ . Another term,  $W_{pl,i}$ , is necessary for fracture initiation, i.e. for deforming the material until to the point when the first crack extension occurs in the specimen center. The total plastic strain energy (consumed until a certain amount of total crack extension or until final fracture),  $W_{pl,tot}$ , is given by

$$W_{pl,tot} = W_{pl,i} + W_{pl,flat} + W_{pl,slant} + W_{pl,lat}. \quad (5.2)$$

It should be noted that both the second and the third term of Eq.(5.2) might contain also some remote plasticity appearing near the back face of the specimen.

Since  $W_{pl,i}$  remains unchanged after fracture initiation, it does not influence the size of  $R_{tot}$ . Thus, the totally consumed non-reversible energy during fracture can be written as

$$W_{pl,tot} = W_{pl,i} + \int_0^{\Delta a} R_{tot} d(\Delta a). \quad (5.3)$$

### 5.3.2 A general outline for determining the energy terms

The indirect approach to determine the different energy terms relies on the measurement of the crack growth resistance of the materials not only in terms of the commonly used J-integral vs. crack extension ( $J - \Delta a$ -) curves, but also in terms of the total crack growth resistance,  $R_{tot}$ , vs.  $\Delta a$  curves.

**Tab. 5.1.** Chemical composition of the maraging steel V720

C	Si	Mn	Mo	Ni	Co	Ti	Al
0.003	0.10	0.10	5.3	18.5	9.0	0.6	0.1

$W_{pl,i}$  is evaluated from the area under the load vs. load-line displacement curve at the point of fracture initiation (which is detected by a potential drop technique).  $W_{pl,flat}$  and the fracture properties of the specimen center region are derived from a test of a side-grooved specimen (see Fig. 5.1).  $W_{pl,slant}$  is determined from the resistance curve of a thin specimen where the two shear lip regions merge into one slant fracture surface.  $W_{pl,lat}$  can be measured as the shaded area in the  $R_{tot} - \Delta a$ -curves in Fig. 5.1. This is deduced from the results of a multi-specimen test and demonstrated on specimens with different thicknesses.

In a previous investigation a digital image analysis procedure for reconstructing the topography of fracture surfaces from stereo photographs taken in the scanning electron microscope was developed [5.31, 5.32]. This technique is used for the direct approach to determine the fracture energy terms. From the topographic measurements the fracture surface energy,  $W_{pl,surf}$ , is evaluated using Stüwe's model. The new technique allows the automatic analysis of whole fracture surface regions, compared to the time consuming point-per-point analysis which had to be done in [5.28, 5.29, 5.33]. This enables  $W_{pl,surf}$  to be estimated much faster and more accurately than in previous work [5.34, 5.35].

Our new technique for analyzing fracture surfaces can be also applied to measure the crack opening angle,  $COA$ , near the mid-section of the specimens. This allows the determination of  $W_{pl,sub}$  for the flat-fracture region.

## 5.4 Materials and Specimens

The separation of the total fracture energy is demonstrated on two materials. The first material is a solution annealed maraging steel V 720. The steel was forged, solution annealed for 1 hour at 820°C, and subsequently cooled in air. The tensile tests resulted a yield strength of  $\sigma_y = 750$  MPa, an ultimate tensile strength of  $\sigma_u = 1050$  MPa and a strain hardening exponent of  $n = 0.15$ . The Young's modulus is  $E = 193$  GPa. The chemical composition is given in Tab. 5.1.

The second material is a nitrogen alloyed ferritic-austenitic duplex steel A 905. After the forging the steel was solution annealed for 30 minutes at 1100°C and water quenched. Due to this treatment the steel has a microstructure of elongated domains of about 50% austenite and ferrite. The tensile properties (perpendicular to the crack plane) are  $\sigma_y = 630$  MPa,  $\sigma_u = 950$  MPa,  $n = 0.20$  and  $E = 215$  GPa. The chemical composition is given in Tab. 5.2.

From both materials Compact Tension (CT-) specimens were machined in a  $S$ - $T$ -crack plane orientation, i.e. the elongated domains of the steel A 905 lie parallel to the crack front. The specimens had a width of  $W = 50$  mm, an initial crack length  $a_0 \approx 28$  mm

**Tab. 5.2.** Chemical composition of the duplex steel A905

C	Si	Mn	P	S	Cr	Mo	Ni
0.017	0.37	5.15	0.021	0.002	25.63	2.04	4.04
V	W	Cu	Al	N			
0.06	0.49	0.10	0.009	0.34			

and a thickness of  $B = 25$  mm. For the steel V 720 thinner specimens were tested, too.

## 5.5 An Indirect Procedure to Separate Fracture Energies

In this section characteristic plastic energy terms are extracted from fracture mechanics tests conducted with side-grooved specimens and plain-sided specimens of different thicknesses. J-integral versus crack extension ( $J$ - $\Delta a$ ) curves were recorded following the ESIS [5.36] and ASTM [5.37] Standard Procedures. The  $R_{\text{tot}}-\Delta a$ -curves were determined by a single-specimen technique which is described in the following section.

### 5.5.1 Single specimen tests

#### 5.5.1.1 A single specimen technique for measuring the total crack growth resistance

Eq. (5.1) can be extended by considering the balance of energy during an increment of crack extension [5.11],

$$R_{\text{tot}} \equiv \frac{1}{B} \frac{d(W_{\text{pl}} + \Gamma)}{d(\Delta a)} = \frac{1}{B} \frac{d(U - W_{\text{el}})}{d(\Delta a)} \equiv C. \quad (5.4)$$

The right-hand side extension of Eq. (5.4) can be seen as the crack driving force,  $C$  which balances  $R_{\text{tot}}$  during equilibrium crack growth. It is used to evaluate  $R_{\text{tot}}$  experimentally.  $U$  is the external energy which can be measured by integrating the area below the load vs. load-line displacement ( $F$ - $v_{\text{LL}}$ -) curve. The reversible elastic strain energy,  $W_{\text{el}}$ , can be determined by measuring the load,  $F$ , and applying the relation

$$W_{\text{el}} = \frac{\phi F^2}{2}, \quad (5.5)$$

where  $\phi$  denotes the compliance of the specimen. For the side-grooved specimen  $\phi$  is evaluated for an effective thickness,  $B_e$ . Formulae for  $\phi$  and  $B_e$  are given in the Standard Procedures [5.36, 5.37].

If the current crack length is known,  $R_{\text{tot}}$  can be evaluated by differentiating numerically the ( $U - W_{\text{el}}$ ) vs.  $\Delta a$ -curve. The current crack length is determined by the direct-current potential drop technique.

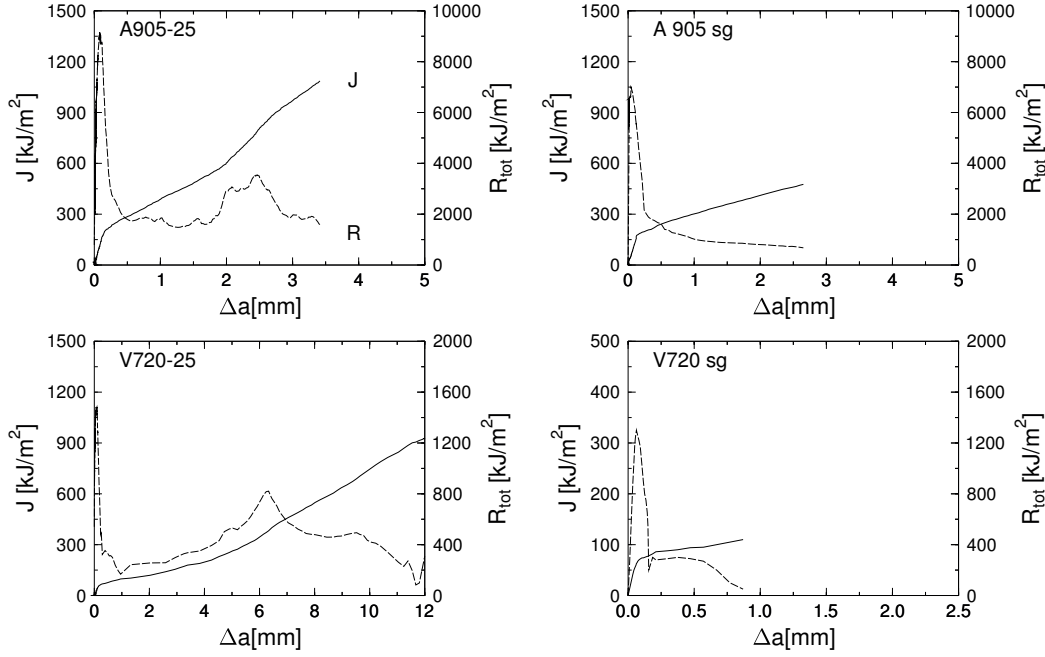


**Figure 5.3:**  $J$ -integral,  $J$  (solid line), and total crack growth resistance,  $R_{\text{tot}}$  (dashed line), with respect to the crack extension,  $\Delta a$ , for 25 mm thick specimen with and without side-grooves. Note the different scales.

### 5.5.1.2 Test results of the plain-sided specimens

On the left-hand side of Fig. 5.3 the  $R_{\text{tot}}-\Delta a$ -curves of the plain sided specimens are plotted, together with the conventional  $J$ -integral vs. crack extension ( $J$ - $\Delta a$ -) curves. Both  $R_{\text{tot}}-\Delta a$ -curves exhibit sharp peaks at or near the point of fracture initiation. For the steel A 905,  $R_{\text{tot}}$  falls down after the peak to a lower plateau value of  $R_{\text{tot}} \approx 2000 \text{ kJ/m}^2$ . Between  $\Delta a = 1.7$  and  $2.8 \text{ mm}$  a second peak can be observed with a maximum value of  $\hat{R}_{\text{tot}} \approx 4000 \text{ kJ/m}^2$  at  $\hat{\Delta a} = 2.5 \text{ mm}$ . For the steel V 720 the picture is not so clear. It is possible to detect a lower plateau value of about  $R_{\text{tot}} \approx 270 \text{ kJ/m}^2$  combined with a very broad peak between  $\Delta a = 2.5$  to  $11 \text{ mm}$ . The second  $R_{\text{tot}}$ -peak,  $\hat{R}_{\text{tot}} \approx 800 \text{ kJ/m}^2$ , lies at  $\hat{\Delta a} = 6.2 \text{ mm}$ . The  $J$ - $\Delta a$ -curves yield fracture initiation values of  $J_i = 65 \text{ kJ/m}^2$  for the steel V 720 and  $J_i = 200 \text{ kJ/m}^2$  for the steel A 905.

Beyond the initial part, the  $R_{\text{tot}}-\Delta a$ -curves look like the first derivatives of the  $J$ - $\Delta a$ -curves. This is reasonable because for general-yielding conditions  $R_{\text{tot}}$  and the slope of the  $J$ - $\Delta a$ -curve are directly related (and not  $R_{\text{tot}}$  and  $J$ !) [5.38]. For deeply notched bend-type specimens the relation reads (see Sec. 5.10)

$$\frac{dJ}{d(\Delta a)} \approx \frac{\eta}{b} R_{\text{tot}}. \quad (5.6)$$

$b$  is the ligament length,  $b = W - a$ , and  $\eta$  is the pre-factor in the formula to evaluate  $J$  from the area,  $U$ , below the  $F$ - $v_{\text{LL}}$ -curve,

$$J = \frac{\eta U}{bB}. \quad (5.7)$$

In [5.8] a relation between the slope of the  $J$ - $\Delta a$ -curve and  $R_{\text{tot}}$  was deduced that is valid for sssy-conditions as well. As was pointed out by Kolednik [5.8, 5.38], the significance of Eq. (5.6) lies in the fact that it clearly demonstrates that for elastic-plastic materials the  $J$ - $\Delta a$ -curve does not scale to the crack growth resistance. This fact was noticed later by Atkins [5.39], and Cotterell and Atkins [5.40], too.

The first peak of the  $R_{\text{tot}}$ - $\Delta a$ -curve is a result of crack tip blunting. It was found in [5.42] that the point of fracture initiation in the center region is correlated to the (first) inflection point of the  $R_{\text{tot}}$ - $\Delta a$ -curve. To understand the significance of the second peak we conducted an extensive multi-specimen test on the steel V 720. Before discussing this multi-specimen test, the testing results of the side-grooved specimens shall be presented.

### 5.5.1.3 Test results of the side-grooved specimens

We performed these single-specimen tests with 20% side-grooved specimens,  $B_n = 20$  mm. The results are shown on the right-hand side of Fig. 5.3.

The  $R_{\text{tot}}$ - $\Delta a$ -curve of the steel V 720 shows a sharp peak at initiation followed by a very short plateau region with  $R_{\text{tot}} \approx 280$  kJ/m<sup>2</sup> (which comes close to the lower plateau value of the non-sidegrooved specimen seen in Fig. 5.3). We doubt that the decrease of  $R_{\text{tot}}$  after  $\Delta a \approx 0.6$  mm is significant because the crack growth became unstable afterwards. The decrease in  $R_{\text{tot}}$  is caused probably by the increase of the crack velocity. Thus, we take  $R_{\text{flat}} \approx 280$  kJ/m<sup>2</sup> as the approximate value of the crack growth resistance for the (steady-state) flat-fracture region, although there remains some uncertainty for larger  $\Delta a$ -values. The  $J$ - $\Delta a$ -curve shows a fracture initiation value that is similar to that for the non-side grooved specimen,  $J_i = 70$  kJ/m<sup>2</sup>.

A similar behavior was observed for the steel A 905. After the initiation peak, the  $R_{\text{tot}}$ - $\Delta a$ -curve slowly decreases to a value of about  $R_{\text{tot}} \approx 1000$  kJ/m<sup>2</sup>. This value is taken as approximating  $R_{\text{flat}}$ . Due to the increased crack velocity the few data points measured beyond  $\Delta a \approx 1.4$  mm are questionable. From the  $J$ - $\Delta a$ -curve we get  $J_i = 190$  kJ/m<sup>2</sup>.

It should be stated that side-grooved specimens do not necessarily give  $R_{\text{flat}}$ -values. In very tough materials some lateral contraction can be observed in spite of the side-grooves.

## 5.5.2 A multi-specimen test on the steel V-720

In Fig. 5.6 the heat-tinted surfaces of the 12 broken specimens of the steel V 720 are shown. It can be seen that the crack extension in the center region of the specimen is about 15 mm when the crack begins to grow near the side surfaces. In Fig. 5.4 the local

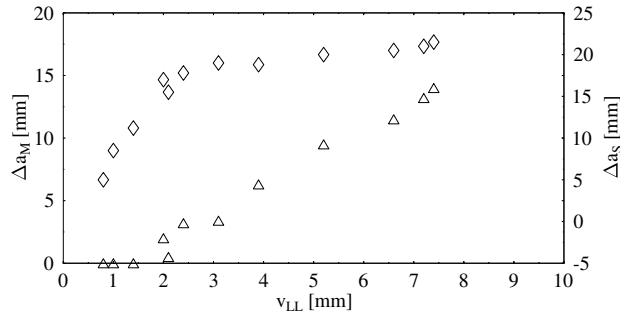


**Figure 5.4:** Local crack in the mid-section region  $\Delta a_M$  (◇), and at the side-surfaces,  $\Delta a_S$  (△), with respect to the load line displacement,  $v_{LL}$ , for plain-sided specimens of the steel V 720.

crack extensions in the mid-section,  $\Delta a_M$ , and at the side surfaces,  $\Delta a_S$ , are plotted with respect to the load-line displacement.

Near the mid-section the crack growth is initiated at  $v_{LL} \approx 0.5$  mm. At a load-line displacement of about  $v_{LL} \approx 2$  mm crack growth starts at the side surfaces. At the same moment the crack growth rate in the center region slows down appreciably because the crack already approaches the neutral axis of the CT-specimen. From the  $v_{LL}$ - $\Delta a$ -curve (which is not included here) it is seen that at  $v_{LL} = 2$  mm the crack extension amounts  $\Delta a \approx 6.3$  mm. At this value the  $R_{tot} - \Delta a$  curve has its second peak. Thus, it is concluded that this peak appears at (or shortly before) the moment where crack growth is initiated at the side surfaces. A similar observation was made in [5.41] for another material.

It is interesting to check the lateral contraction of the plain-sided specimens. The maximum deformation in thickness ( $z$ -) direction (which amounts 0.32 mm on each side) is reached when the crack extension starts near the side surfaces. During further crack extension at the side surfaces a “lateral contraction zone” moves with the crack front, but the amount of additional  $z$ -deformation decreases.

The results of this section suggest that the second peak of the  $R_{tot} - \Delta a$ -curve may originate from the blunting process near the side-surface regions and the lateral contraction of the specimen. The curve displays its second maximum at the point of initiation of crack growth near the side surfaces.

To prove this hypothesis  $R_{tot}$ - $\Delta a$ -curves were analyzed for specimens with different thicknesses.

### 5.5.3 The influence of specimen thickness

From the steel V 720 additional single specimen tests were conducted on specimens having thicknesses of  $B = 16, 8,$  and  $4$  mm. The resulting  $R_{tot}$ - $\Delta a$ - and  $J$ - $\Delta a$ -curves

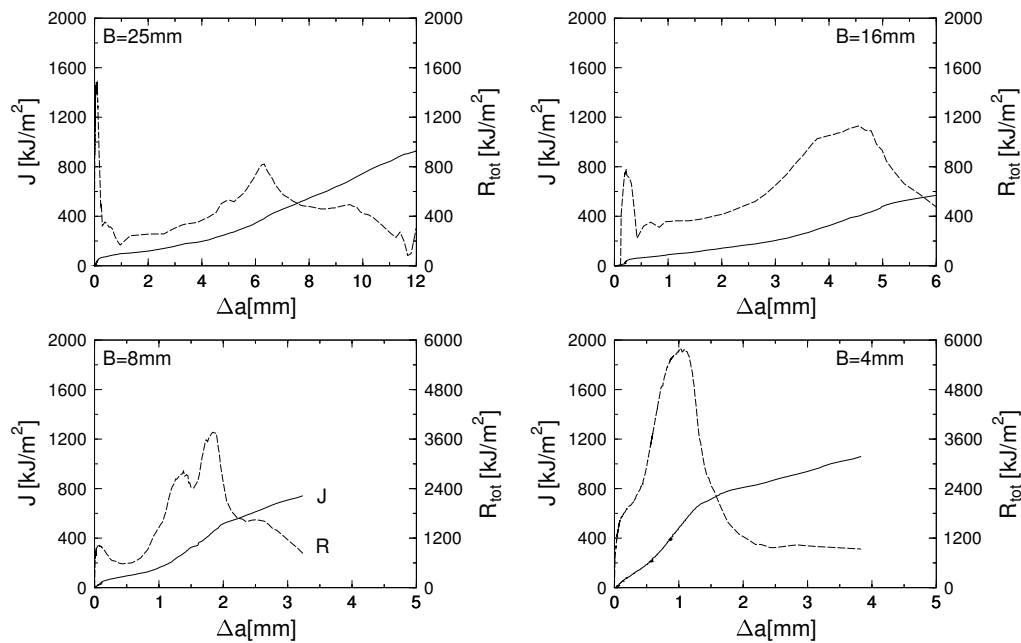


**Figure 5.5:**  $J$ -integral,  $J$  (solid line), and total crack growth resistance,  $R_{tot}$  (dashed line), with respect to the crack extension,  $\Delta a$ , for plain-sided specimens of different thickness. Steel V 720. Note the different scales.

are collected in Fig. 5.5.

All  $J$ -integral initiation values lie about  $J_i = (60 - 65) \text{ kJ}/\text{m}^2$ . It is noteworthy that with decreasing thickness the second peak of the  $R_{tot}-\Delta a$ -curve is shifted to lower  $\Delta a$ -values:  $\widehat{\Delta a} = 6.2, 4.5, 1.8$  and  $1.1$  mm for  $B = 25, 16, 8$  and  $4$  mm. The height of the second peak increases:  $\widehat{R_{tot}} = 800, 1100, 3700$  and  $5800 \text{ kJ}/\text{m}^2$ .

Of particular interest is the  $R_{tot}-\Delta a$ -curve of the thinnest specimen,  $B = 4$  mm, where the first and second peak merge into one peak. After a mean crack extension of  $\Delta a \approx 2.3$  mm a steady-state condition seems to be reached when  $R_{tot} = 1000 \text{ kJ}/\text{m}^2$ . The fracture surface reveals a short, cusped flat fracture region. The two shear lip regions join and form one slant fracture surface region.

The lateral contraction of the specimens was studied, too. In each specimen the  $z$ -deformation is largest at the position of the stretched zone in the mid-section of the specimen. By comparing different specimens it can be observed that the  $z$ -deformation reaches its maximum value at that point when crack growth is initiated at the side surfaces. The lateral contraction process is about to be completed when the end of the second peak of the  $R_{tot}-\Delta a$ -curve is reached, e.g. at  $\Delta a \approx 2.3$  mm for the thinnest specimen. The mean crack extension where the lateral contraction process is completed, will depend on the ligament length. For a specimen with a very large ligament length, e.g., a Double Cantilever Beam (DCB) specimen, or ideally, an infinite clamped strip, the lateral contraction process would not cease and a steady-state contraction zone would move with the crack front.

This point leads to the conclusion that the steady-state  $R_{tot}$  of this specimen after the peak characterizes the crack growth resistance for producing a slant shear-lip fracture surface. Thus, we get for the steel V 720 a characteristic value of  $R_{slant} = 1000 \text{ kJ/m}^2$ . The ratio  $R_{slant}/R_{flat}$  has a size of 3.6.

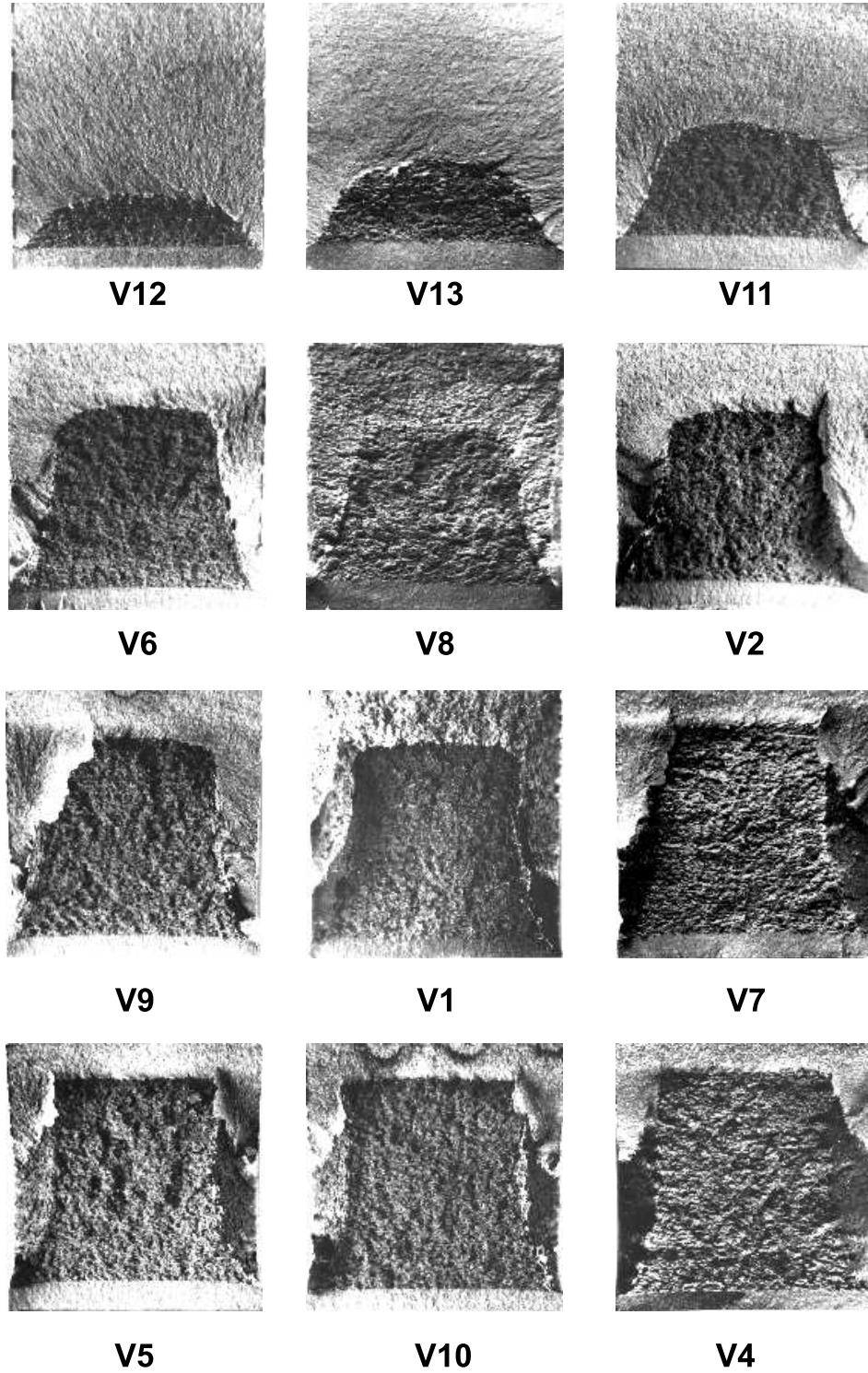


**Figure 5.6:** Heat-tinted fracture surfaces of the V720-specimens from the multi-specimen test. The specimen thickness is 25 mm

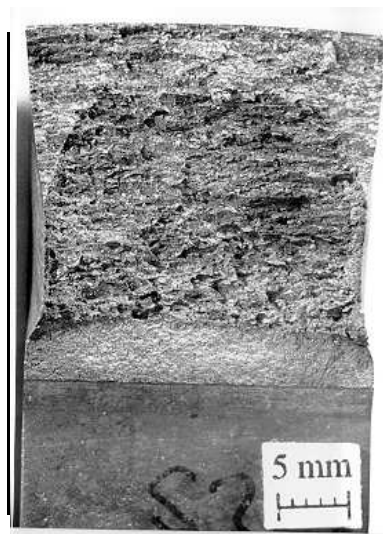
### 5.5.4 Fracture surface analysis on the steel A 905

Fig. 5.7 presents the fracture surface of a plain sided specimen made of the steel A 905. No shear lips can be found. The reason is that the ferritic domains in front of the crack tip fail at low loads by cleavage or quasi-cleavage fracture [5.42]. At these low loads the width of the low-constraint side-surface region, which scales with the plastic zone size, is small and, as a consequence, no shear lips can be formed. A similar observation was made on a mild steel containing long MnS-inclusions [5.29]: the critical plastic strain for void nucleation is very small, hence no shear lips can be formed.

A section parallel to the crack front shows that the flat fracture surfaces bend concavely near the side surfaces. It seems as if the crack growth resistance for flat fracture,  $R_{\text{flat}}$ , increases gradually when approaching the side surfaces due to an increase of the subsurface energy,  $W_{\text{pl,sub}}$ . The two regions of enhanced  $R_{\text{flat}}$  are 6 to 7 mm broad (observe the development of the stretched zone width along the crack front in Fig. 5.7).

The lateral contraction of this specimen is quite large, too. The maximum  $z$ -deformation amounts 1.16 mm on each side.

Summarizing this section, it is stated that there exists no unique characteristic value of the crack growth resistance of the near-side surface regions for the steel A 905.



**Figure 5.7:** Fracture surface of a plain-sided specimen made of steel A 905. Note the large lateral contraction and the increased width of the stretched zone near the side-surfaces.

### 5.5.5 The separation of the fracture energies

#### 5.5.5.1 General remarks

As a basic hypothesis for the separation of the total plastic strain energy,  $W_{\text{pl,tot}}$ , into its components (via the indirect approach) it is assumed that there exist characteris-

tic values of the crack growth resistance to form either the (plane strain) flat-fracture surfaces,  $R_{\text{flat}}$ , or the slant shear lip surfaces,  $R_{\text{slant}}$ .  $R_{\text{flat}}$  and  $R_{\text{slant}}$  should be independent of crack extension and specimen thickness. This assumption does not seem unrealistic, as long as we consider deeply notched CT- or bend type specimen.

The separation is demonstrated on five specimens of the steel V 720 (plain sided specimens with thicknesses  $B = 25, 16, 8, 4$  mm and side grooved specimen) and on the two specimens of the steel A 905. All the results of the separation procedure are collected in Table 5.1.

The fracture surfaces of each (heat tinted) specimen were photographed in the scanning electron microscope. On each photo the final average crack extension,  $\Delta a_{\text{tot}}$ , was measured. The boundary between the flat-fracture and the slant-fracture region was marked. and the sizes of the corresponding fracture surface areas,  $\Delta A_{\text{flat}}$  and  $\Delta A_{\text{slant}}$ , were determined. The plastic strain energies to form either the flat or the slant fracture surfaces are estimated by

$$W_{\text{pl,flat}} = R_{\text{flat}} \Delta A_{\text{flat}} \quad (5.8)$$

or

$$W_{\text{pl,slant}} = R_{\text{slant}} \Delta A_{\text{slant}}. \quad (5.9)$$

The values  $R_{\text{flat}} = 280 \text{ kJ/m}^2$  and  $R_{\text{slant}} = 1000 \text{ kJ/m}^2$  were used for the steel V 720, and  $R_{\text{flat}} = 1000 \text{ kJ/m}^2$  for the steel A 905. For the latter material  $W_{\text{pl,slant}}$  was not determined because no shear lips were observed.

The second peak of the  $R_{\text{tot}}-\Delta a$ -curve was ascribed to the blunting process near the side-surface regions and to the lateral contraction of the specimen. Accordingly, the plastic strain energy term  $W_{\text{pl,lat}}$  can be evaluated by integrating numerically the area under the second peak in the  $R_{\text{tot}}-\Delta a$ -curve. (The area is taken above an estimated “baseline” that is given, e.g. for the steel A 905 by the steady-state value  $R_{\text{tot}} = 2000 \text{ kJ/m}^2$ .)

The  $W_{\text{pl,i}}$ - and the  $W_{\text{pl,tot}}$ -values are taken from the areas,  $U$ , under the load vs. load-line displacement curves by subtracting the elastic energy, Eq.(5.5).

### 5.5.5.2 Discussion of the results

Table 5.1 lists the following data: the final crack extension,  $\Delta a_{\text{tot}}$ ; the  $J$ -integral at fracture initiation in the center,  $J_i$ ; the flat-fracture area,  $\Delta A_{\text{flat}}$ , and the slant-fracture area,  $\Delta A_{\text{slant}}$ ; the plastic strain energies for fracture initiation in the center,  $W_{\text{pl,i}}$ , for forming the flat-fracture area,  $W_{\text{pl,flat}}$ , for forming the slant-fracture area,  $W_{\text{pl,slant}}$ , and for side-surface blunting and lateral contraction,  $W_{\text{pl,lat}}$ ; the sum of the estimated plastic fracture energies,  $\sum W_{\text{pl,est}} = W_{\text{pl,i}} + W_{\text{pl,flat}} + W_{\text{pl,slant}} + W_{\text{pl,lat}}$ , and the total plastic strain energy,  $W_{\text{pl,tot}}$ , measured in the tests.

It is interesting to note that  $W_{\text{pl,lat}} \approx 30 \text{ J}$  for the three thickest plain sided specimens of the steel V 720. This suggests that the plastic strain energy for side-surface blunting and lateral contraction is constant as long as the specimen is thick enough, so that the two shear lip regions are still separated by a flat-fracture region.

The ratio  $W_{pl,lat}/W_{pl,tot}$  gives the percentage of the total non-reversible fracture energy that comes from blunting and lateral contraction at the side surfaces. This ratio is remarkably large: For the steel V 720 the values are (with decreasing thickness) 26, 43, 69 and 61%, and for the steel A 905 it is 22%. (It should be kept in mind that the final crack extension of the specimens differs. All specimens were loaded at least up to the end of the second peak of the  $R_{tot}-\Delta a$ -curve. The reason for the different  $\Delta a_{tot}$ -values is that thinner specimens exhibit larger load-line displacement values and the tests had to be stopped before the clip gauge went out of range.)

A principle error is made in connection with the term  $W_{pl,i}$ . The reason is that at the point of fracture initiation,  $J = J_i$ , the crack extension has already reached a small, but finite value,  $\Delta a_i$ .  $\Delta A_i$  denotes the flat-fracture surface area at initiation. Thus, some plastic strain energy to produce  $\Delta A_i$  is counted twice, because it is included in both the  $W_{pl,i}$ , as well as in the  $W_{pl,flat}$  term. However, this error will be negligible in most cases except for small  $\Delta a_{tot}$ -values.

The sum of the estimated plastic fracture energies coincides quite well with the measured total plastic strain energy. The only exception is the plain sided specimen of the steel A 905, where the assumption of a constant  $R_{flat}$  is clearly not met, see Section 5.5.4.

Although no firm proof, this strongly suggests that our assumption of characteristic values of  $R_{flat}$  (for both steels) and  $R_{slant}$  (for the steel V 720) is correct. No data are available of specimens with other ligament lengths or other sizes. As far as it concerns highly constraint bend-type specimens, we expect that the characteristic values would be the same. However, we do not know how the flat-fracture and shear-lip fracture values would change for specimens with a low global constraint, like center-cracked tensile specimens. Whether the plastic strain energy for side-surface blunting and lateral contraction,  $W_{pl,lat}$  can be treated as a characteristic value, remains unclear.

**Table 5.1:** The separation of the total plastic strain energy for fracture,  $W_{pl,tot}$ , into its components: the plastic energies for producing fracture initiation in the center,  $W_{pl,i}$ , for forming the flat-fracture area,  $W_{pl,flat}$ , for forming the slant-fracture area,  $W_{pl,slant}$ , and for side-surface blunting and lateral contraction,  $W_{pl,lat}$ . Except for the specimen A 905-25, the sum of the local energies,  $\sum W_{pl,est}$ , corresponds well with the experimentally measured value  $W_{pl,tot}$

Specimen	$\Delta a_{tot}$	$J_i$	$\Delta A_{flat}$	$\Delta A_{slant}$	$W_{pl,i}$	$W_{pl,flat}$	$W_{pl,slant}$	$W_{pl,lat}$	$\sum W_{pl,est}$	$W_{pl,tot}$
	[mm]	[kJ/m <sup>2</sup> ]	[mm <sup>2</sup> ]	[mm <sup>2</sup> ]	[J]	[J]	[J]	[J]	[J]	[J]
V720-25	11.5	65	248	40	6.0	69	40	33	148	125
V720-16	7.4	60	102	15	3.0	29	15	29	76	68
V720-8	3.3	65	19.2	7.4	1.3	5.4	7.4	29	46	42
V720-4	3.0	65	10.8	5.2	0.6	3.0	5.2	17	26	28
V720-25sg	0.6	70	12.0	0	1.8	3.4	0	0	5.2	4.6
A905-25	3.5	200	88	0	33	88	0	45	146	207
A90-25sg	2.7	190	53	0	27	53	0	0	80	70

## 5.6 The Estimate of Fracture Energies from Fracture Surface Analyses

This section deals with the direct determination of characteristic plastic strain energies via stereophotogrammetric analyses of the fracture surfaces.

### 5.6.1 Stereophotogrammetry

Stereophotogrammetric means have been applied for a long time in fracture research, e.g., to study the topography of fatigue crack surfaces [5.43], and of micro-ductile [5.29, 5.33, 5.44, 5.45] or cleavage [5.29, 5.46, 5.47] fracture surfaces. The first semi-automatic analyses were reported in [5.48, 5.49].

Recently, an already existing digital photogrammetry system [5.50] was used to develop an automatic system for fracture surface analysis. The topography of a fracture surface is reconstructed by taking stereophotograms in the scanning electron microscope (SEM) and analyzing the images with a system for automatic image processing. This system finds homologous points on the stereophotograms and generates a three-dimensional model of the fracture surface consisting of about 10.000 to 20.000 points. The model is called "digital elevation model", DEM. The computing time for an analysis is about ten minutes on a PC. The new system for automatic fracture surface analysis is described in more detail in [5.31, 5.32, 5.35].

### 5.6.2 The plane strain fracture surface energy

In [5.26, 5.27], Stüwe introduced a model to estimate the plastic strain energy that is necessary to form a ductile fracture surface,  $W_{\text{pl,surf}}$ . A schematic cross-section of the broken specimen shows a series of dimples of height  $h_0$ , see Fig. 5.2.  $W_{\text{pl,surf}}$  is given by

$$W_{\text{pl,surf}} = 2 \int_0^{h_0} A(h) \left( \int_0^{\varphi(h)} \sigma(\varphi) d\varphi \right) dh \quad (5.10)$$

In Eq. (5.10)  $A(h)$  denotes the cross section at height  $h$ ,  $A_0$  is the original cross section,  $\varphi$  is the logarithmic (plastic) strain and  $\sigma(\varphi)$  is the flow stress. After inserting the relation  $\varphi(h) = \ln \left( \frac{A_0}{A(h)} \right)$  and after division by  $A_0$  the equation transforms to

$$R_{\text{surf}} = \frac{W_{\text{pl,surf}}}{A_0} = 2\bar{\sigma} \int_0^{h_0} \frac{A(h)}{A_0} \ln \left( \frac{A_0}{A(h)} \right) dh. \quad (5.11)$$

$R_{\text{surf}}$  is the specific plastic strain energy to form the micro-ductile fracture surface profile depicted in Fig. 5.2. The surface energy term is neglected.

$\bar{\sigma}$  designates an appropriate mean flow stress of the material which can be estimated by [5.27]

$$\bar{\sigma} = \sigma_u \frac{\exp(n)}{(1+n)n^n}, \quad (5.12)$$

using the approximation  $\sigma = \sigma_0 \varphi^n$  for the stress-strain curve where  $n$  is the strain hardening exponent and  $\sigma_0$  a reference stress. Eq.(5.11) can be evaluated if the distribution of  $A(h)$  versus  $h$  of the considered fracture surface regions is known.

It should be stated that the so determined value of  $W_{\text{pl,surf}}$ , sums the plastic strain energies of the fracture surfaces from the point of void initiation until to final failure of the bridges between the voids . Some plastic deformation energy,  $W_{\text{pl,sub}}$ , is additionally needed to initiate the voids. That means that, e.g. in the Irwin-Orowan case the total crack growth resistance must be somewhat larger,  $R_{\text{tot,ssy}} \geq R_{\text{surf}}$ , although the difference might be very small.

The knowledge of the topography of one fracture surface is not sufficient to evaluate Eq.(5.11), because the topography of one DEM could be compensated by the topography of its opposite from the second specimen half. For example, an ideally brittle material may exhibit a rough fracture surface, i.e. a certain distribution of  $A(h)$  versus  $h$  on one specimen half, but the two broken pieces could be glued together without any misfit and  $R_{\text{surf}}$  would be zero.  $R_{\text{surf}}$  is determined by the misfit between the broken parts. That means that the corresponding fracture surface regions on both parts of a broken specimen must be analyzed. The two opposite DEMs are then used to generate a void map [5.34] that contains the information about the misfit between the two fracture surfaces, i.e. the distribution of  $A(h)$  versus  $h$ . with this Eq.(5.11) can be solved numerically.

The specific plane strain fracture surface energy,  $R_{\text{surf}}$ , was determined on the steel V 720, only. (The austenitic-ferritic duplex steel A 905 shows a patchwork of micro-ductile and cleavage fracture surface regions. The determination of  $R_{\text{surf}}$  needs, therefore, a more sophisticated analysis, e.g. see [5.51], which has not been undertaken so far.) SEM-micrographs of two corresponding fracture surface regions near the stretched zone , together with the DEMs and crack profiles perpendicular to the crack front are presented in Fig. 5.8, 5.9 and 5.10. A void map can be found in [5.32]. Table 5.3 lists the estimated  $R_{\text{surf}}$ -values. All four values lie around  $R_{\text{surf}} = 20 \text{ kJ/m}^2$ . It is interesting to note that even the same size is measured for the side-grooved specimen at a distance of 3 mm in front of the fatigue crack, which is well beyond the point where fracture became unstable.

**Tab. 5.3.** The plastic strain energy to form a unit area of the micro-ductile flat-fracture surface for a plain-sided and a side-grooved specimen.

Specimen	Distance from fatigue crack	$R_{surf}$
	mm	$kJ/m^2$
V720-25	0.1	23
	0.1	16
	2.0	19
V720-sg	3.0	20

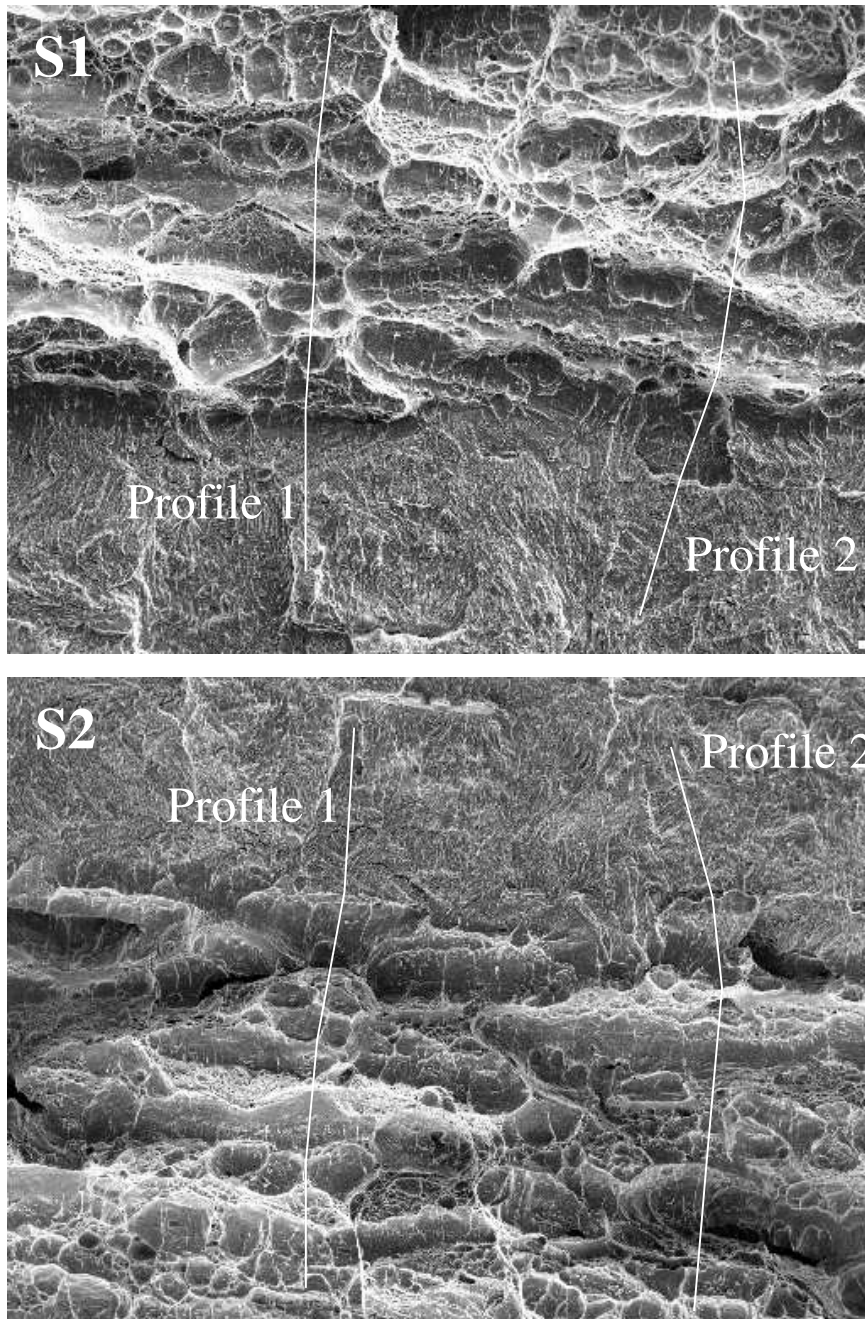


**Figure 5.8:** Corresponding fracture surfaces of the maraging steel V 720. The digital elevation models (DEMs) of the fracture surfaces are shown in Fig. 5.9, the crack profiles are presented in Fig. 5.10.

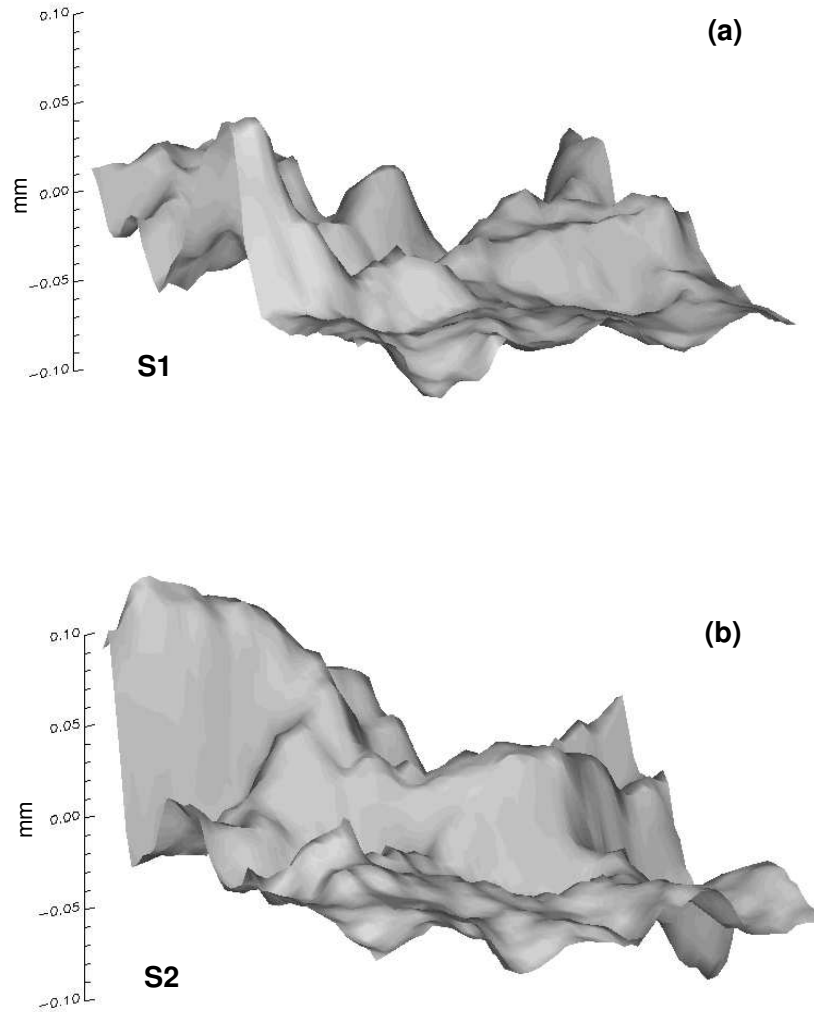


**Figure 5.9:** DEMs of the fracture surfaces in Fig. 5.8. Both specimen halves, side 1 (a) and side 2 (b), are shown.

### 5.6.3 The direct determination of $R_{\text{flat}}$

From the preceding section it is seen that for the steel V 720 even in the flat-fracture region only 7% of the plastic energy is used to form the fracture surfaces. The remaining 93% are spent below the surface. This energy,  $R_{\text{sub}} = R_{\text{flat}} - R_{\text{surf}} = 260 \text{ kJ/m}^2$ , is needed to produce the global crack opening angle,  $COA$ , in the wake of the crack.

$COA$  and  $R_{\text{tot}}$  are related by (see Sec. 5.10)

$$COA = \frac{dCOD}{d\Delta a} \approx \frac{\eta}{m\sigma_y b} R_{\text{tot}}. \quad (5.13)$$

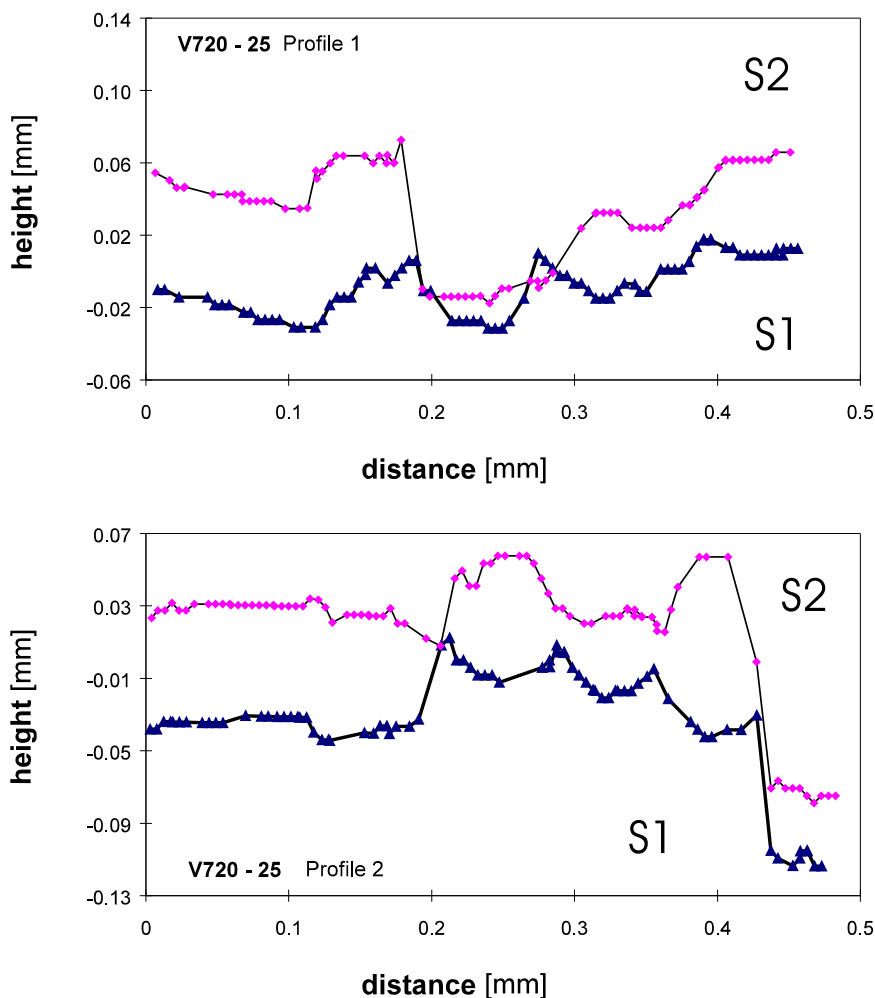


**Figure 5.10:** Crack profiles from the fracture surfaces in Fig. 5.8

Eq.(5.13) considers the behavior of the total specimen:  $\Delta a$  is the average of the crack extension values along the crack front and  $R_{tot}$  is the total crack growth resistance.  $COA$  and  $COD$  can be imagined as global values similar to that determined from the load-line displacement by adopting a plastic-hinge opening model with a fixed rotational center. However, Eq.(5.13) can be applied for a local description, too:  $COD$  and  $\Delta a$  are then local values measured at a given position along the crack front, and  $COA$  is, thus, a measure of the local crack growth resistance. To describe the behavior of the flat-fracture region Eq.(5.13) must be re-written as

$$COA_{flat} = \frac{dCOD_{flat}}{d\Delta a_M} \approx \frac{\eta}{m\sigma_y b} R_{sub}. \quad (5.14)$$

$\Delta a_M$  is the local crack extension in the mid-section. Inserting the data for the steel V 720 (with  $m = 1.9$  from Eq.(5.18)), the  $COA$ -estimate results  $COA_{flat} = 1.0^\circ$ .

A series of low-magnification stereophotograms were taken from the mid-section region of specimen to determine  $COA_{flat}$  experimentally. Again, both specimen halves were analyzed. From the DEMs crack profiles were extracted, from which  $COD$ -

$\Delta a$ -curves and the crack opening angle could be measured. The measurement gave  $COA_{\text{flat}} = (1.4 \pm 0.3)^\circ$ . This is in reasonable agreement to the estimated value, especially when bearing in mind that the local  $COD$ - $\Delta a$ -curve is bent and that only a 3 mm long region was analyzed. The curvature decreases with increasing  $\Delta a$ . This is because the local  $CTOD$  at the current tip displays a transition regime of declining values before it reaches its steady-state value [5.1, 5.23, 5.55].

From the preceding paragraph it is learned that  $COA$  should be determined in the flat-fracture region at a distance of at least 2 – 3 mm from the fatigue crack to compute  $R_{\text{sub}}$  from Eq.(5.14). The total value of  $R_{\text{flat}}$  is got by adding  $R_{\text{sub}}$  and  $R_{\text{surf}}$ . For tough materials the error, which is made by neglecting the surface term, will be in the order of a few percent, only.

#### 5.6.4 The determination of the local fracture toughness

The new technique for fracture surface analysis is a perfect tool for determining the local fracture properties of a material. The local fracture initiation toughness can be measured in terms of the critical crack tip opening displacement,  $COD_i$ , and the local crack growth toughness can be measured in terms of the crack opening angle,  $COA$ . Both  $COD_i$  and  $COA$  increase near the side-surface. For example, in [5.29, 5.52] the scatter and the variation of  $COD_i$  along the crack front of a mild steel was studied. In [5.53] for the same steel the mid-section and side-surface  $COA$ -values were determined <sup>1</sup>. Surface and mid-section  $COA$ -measurements on aluminum alloys are reported in [5.54]. Additional stereophotogrammetric studies for the two steels V 720 and A 905 are being undertaken presently.

To characterize the fracture properties of materials the characteristic  $COD_i$ - and  $COA$ -values for the flat-fracture and the slant-fracture regions can be sought, and for solving the transferability problem the variation of these values along the crack front (and with crack extension) can be analyzed. With Eq.(5.14) and Eq.(5.17) in Sec. 5.10,  $COD_i$  and  $COA$  can be transformed into the familiar  $J_i$ - and  $R$ -values.

To understand and to improve the fracture properties of two- or multi-phase materials, the determination of local fracture properties will be even more important. There, and in the field of microsystem technology, the new technique offers a vast variety of possible applications. A first example was presented in [5.42]: The crack growth resistance curves of the ferritic-austenitic steel A 905 shows a very strong influence of the crack-plane orientation. Via stereophotogrammetric studies it was possible to determine characteristic values for the fracture initiation toughness and to explain the different shapes of the resistance curves.

<sup>1</sup>These  $COA$ -values were transformed in [5.53] to  $CTOA$ -values taken 0.1 mm behind the current crack tip. The two  $CTOA$ -values (for the mid-section and the side-surface) were used subsequently to control the crack extension in the numerical analysis. In both the experimental determination and the application for controlling the crack growth in numerical studies, it is important to distinguish between global  $COA$  and local, near-tip  $CTOA$  values, see Sec. 5.10. The relation between  $COA$ - and  $CTOA$ -values was treated analytically in [5.10]. In the same paper, [5.10], a rule for estimating  $COA$  for various specimen sizes is proposed.

**Tab. 5.4.** The characteristic fracture energies determined on deeply notched CT specimens.

Material	$J_i$ [kJ/m <sup>2</sup> ]	$R_{surf}$ [kJ/m <sup>2</sup> ]	$R_{flat}$ [kJ/m <sup>2</sup> ]	$R_{slant}$ [kJ/m <sup>2</sup> ]	$W_{lat}$ [J]
Steel V 720	65	20	280	1000	30
Steel A 905	190	?	1000	–	45

## 5.7 Final Discussion and Summary

In this study the total plastic strain energy for fracturing plain-sided CT specimens is separated into several components. The purpose of the separation is to find characteristic fracture energies which can be used for the characterization of the crack growth resistance of the material and for the prediction of the crack growth resistance for other specimen geometries and sizes. For the two materials investigated, the solution annealed maraging steel V 720 and the nitrogen alloyed ferritic-austenitic duplex steel A 905, the characteristic fracture energies are listed in Table 5.4.  $J_i$  gives the commonly used fracture initiation toughness of the materials.  $R_{flat}$  describes the plastic strain energy for forming a unit area of the flat-fracture mid-section region.  $R_{flat}$  consists of a surface and a subsurface component. The surface component,  $R_{surf}$ , is the plastic strain energy to form the dimple structure of the fracture surface.  $R_{slant}$  describes the plastic strain energy for forming a unit area of the slant-fracture near side-surface regions.  $W_{lat}$  is the plastic strain energy for the lateral contraction and for the blunting process at the side-surfaces.

$R_{flat}$  is found by analyzing the crack growth resistance curves of a plain-sided and a side-grooved specimen. The size of  $W_{lat}$  is estimated directly from the resistance curve of the plain-sided specimen. A comparison of the behavior of specimens with different thicknesses shows that  $W_{lat}$  remains constant as long as the two shear-lip regions remain separated by a flat-fracture region. The analysis of a thin specimen, where the two shear-lips merge into one slant-fracture surface, leads to the size of  $R_{slant}$ .

The crucial point for the extraction of the characteristic fracture properties is the analysis of total crack growth resistance curves ( $R_{tot}$ - $\Delta a$ -curves) applying a single-specimen technique.

It is demonstrated that the characteristic fracture energies of the flat-fracture regime can be determined directly from the shape of the corresponding fracture surface regions on both specimen halves.  $J_i$  can be determined by measuring the critical crack tip opening displacement,  $COD_i$ . The sub-surface component of  $R_{flat} = R_{surf} + R_{sub}$  can be evaluated from the crack opening angle,  $COA$ ; the surface component is estimated via a model derived by Stüwe. A new system for the automatic analysis of fracture surfaces from stereophotograms generates tridimensional models of the depicted regions consisting of 10 000 to 20 000 points. From these models the necessary data for the evaluation of  $R_{surf}$  and  $R_{sub}$  can be extracted.

For the steel V 720 all the characteristic fracture energy components could be deter-

mined for four specimens with different thicknesses. The flat-fracture crack growth resistance of this material is not very large,  $R_{\text{flat}} = 280 \text{ kJ/m}^2$ . Only a very small part,  $R_{\text{surf}} = 20 \text{ kJ/m}^2$ , is necessary to form the micro-ductile fracture surface. The same  $R_{\text{surf}}$  is found at the begin and near the end of the transition region, and even in the fast-fracture region of a side-grooved specimen. The generation of a slant shear-lip fracture surface needs much more energy:  $R_{\text{slant}} = 1000 \text{ kJ/m}^2$ . A large part of the total crack growth resistance (22% to 61%) comes from lateral contraction and blunting at the side surfaces. It was found that the plastic work for the lateral contraction and the blunting at the side-surfaces,  $W_{\text{lat}}$ , remains constant as long as the specimen is thick enough, so that the shear-lip regions are separated by a flat-fracture region.

The steel A 905 has no shear-lips. Starting from a plateau-values of  $R_{\text{flat}} = 1000 \text{ kJ/m}^2$ , the flat-fracture crack growth resistance increases gradually towards the side-surface.  $R$  as a function of the distance from the side surface can be determined by stereophotogrammetric analyses. 22% of the total crack growth resistance comes from lateral contraction and blunting at the side surfaces.

Except for one specimen, the sum of local energy terms  $\sum W_{\text{pl,est}}$ , determined according to the procedures described in this work, corresponds well with the experimentally measured value  $W_{\text{pl,tot}}$ .

In this paper, two new techniques are applied to extract characteristic fracture energies from experiments. To solve the transferability problem similar experiments should be repeated, first, on CT- specimens with the same size but different ligament lengths, second, on CT-specimens with different sizes and, third, on different specimen types such as Center Cracked Tension (CCT-) or Double Edged Notched Tension (DENT-) specimens.

## Acknowledgements

---

The authors thank Raj Thampuran for very helpful discussions during the writing of the paper. The authors acknowledge the financial support of this work by the *Austrian Fonds zur Förderung der wissenschaftlichen Forschung* and by the *Österreichische Nationalbankfonds* (project numbers P11559-ÖTE / FWF 456 and P12278-MAT / FWF 482).

## 5.8 References

---

- 5.1 Turner C.E. (1990) in *Fracture Behavior and Design of Materials and Structures, Proc. ECF8* (edited by D. Firrao), EMAS, UK, Vol. II, pp. 933-949 and pp. 951-968.
- 5.2 Leever P.S. and J. C. Radon (1982) *International Journal of Fracture* **19**, 311.
- 5.3 Hancock J.W., W. G. Reuter and D. M. Parks (1993) *ASTM STP* **1171**, 21.

- 5.4 O'Dowd N.P. and C. F. Shih,(1991) *Journal of Mechanics and Physics of Solids* **39**, 989 .
- 5.5 O'Dowd N.P. and C. F. Shih (1994) *ASTM STP* **1207**, 21.
- 5.6 Brocks W. and W. Schmitt (1995) *ASTM STP* **1244**, 209.
- 5.7 Kolednik O., G.X. Shan and F.D. Fischer (1997) *ASTM STP* **1296**, 126.
- 5.8 Kolednik O. (1993) *International Journal of Fracture* **63**, 263.
- 5.9 Braga L.and C. E. Turner (1993) *ASTM STP* **1171**, 158.
- 5.10 Turner C.E. and O. Kolednik (1997) *Fatigue and Fracture of Engineering Materials and Structures* **20**, 1507.
- 5.11 Turner C.E. and O. Kolednik (1994) *Fatigue and Fracture of Engineering Materials and Structures* **17** 1089.
- 5.12 Griffith A.A. (1920) *Philosophical Transactions of the Royal Society London* **A221**, 163.
- 5.13 Orowan E. (1945) *Transactions of the Institute of Engineers and Shipbuilders Scotland* **89**, 165.
- 5.14 Irwin G.R. (1949) in *American Society of Metals Seminar Fracture of Metals* pp. 147-166.
- 5.15 Hutchinson J.W. (1987) *Acta metallurgica* **35**, 1605.
- 5.16 Budiansky B., J. W. Hutchinson and A. G. Evans (1986) *Journal of Mechanics and Physics of Solids* **34**, 167.
- 5.17 Evans A.G. (1989) *ASTM STP* **907**, 267.
- 5.18 Atkins A.G. and Y. W. Mai (1986) *International Journal of Fracture* **30**, 203.
- 5.19 Gurney C. (1994) *Philosophical Magazine* **69**, 33.
- 5.20 Cotterell B. and J. K. Reddel (1977) *International Journal of Fracture* **13**, 267.
- 5.21 Wnuk M.P. and D. T. Read (1986) *International Journal of Fracture* **31**, 161.
- 5.22 Marchal Y. and E. Delannay (1996) *International Journal of Fracture* **80**, 295.
- 5.23 John S. and C. E. Turner (1991) in *Defect Assessment in Components; Fundamentals and Applications, ESIS/EGF Pub. 9* (edited by J. G. Blauel and K.-H. Schwalbe). MEP, London, pp. 299-318.
- 5.24 Shoji T. (1981) *Journal of Testing and Evaluation* **9**, 324.
- 5.25 Mao X.and T. Shoji (1993) *Journal of Materials Science* **28**, 927.
- 5.26 Stüwe H. P. (1990) *Engineering Fracture Mechanics* **13**, 231.

- 5.27 Stüwe H.P. (1981) in *Three-dimensional Constitutive Relations and Ductile Fracture* (edited by S. Nemat-Nasser). North-Holland, Amsterdam, pp. 213-221.
- 5.28 Kolednik O. and H. P. Stüwe (1982) *Zeitschrift für Metallkunde* **73**, 219.
- 5.29 Kolednik O. and H. P. Stüwe (1985) *Engineering Fracture Mechanics* **21**, 145.
- 5.30 Mecklenburg M.F., J. A. Joyce and P. Albrecht (1989) *ASTM STP* **995**, 594.
- 5.31 Scherer S., J. Stampfl, M. Gruber and O. Kolednik (1996) in *Micro Materials '95, 1. Tagung des DVM-Arbeitskreises Mikrosystemtechnik* (edited by B. Michel and T. Winkler). DVM, Berlin, pp. 671-676.
- 5.32 Stampfl J., S. Scherer, M. Gruber and O. Kolednik (1996) *Applied Physics A* **63**, 341.
- 5.33 Kolednik O. (1981) *Practical Metallography* **18**, 562.
- 5.34 Stampfl J., S. Scherer, H.P. Stüwe and O. Kolednik (1996) in *Mechanisms and Mechanics of Damage and Failure, Proc. of ECF 11* (edited by J. Petit). EMAS, UK, Vol.3, pp. 1271-1276.
- 5.35 Stampfl J., S. Scherer, M. Berchthaler, M. Gruber and O. Kolednik (1996) *International Journal of Fracture* **78**, 35.
- 5.36 ESIS P2-92 (1992) European Structural Integrity Society, Delft, The Netherlands.
- 5.37 ASTM E1152-87 (1993) Annual Book of ASTM Standards, Vol. 03.01.
- 5.38 Kolednik O. (1991) *Engineering Fracture Mechanics* **38**, 403.
- 5.39 Atkins A.G. (1995) *Fatigue and Fracture of Engineering Materials and Structures* **18** 1007.
- 5.40 Cotterell B. and A. G. Atkins (1996) *International Journal of Fracture* **81**, 357.
- 5.41 Stampfl J. (1996) PhD thesis, University of Mining and Metallurgy, Leoben.
- 5.42 Kolednik O., M. Albrecht, M. Berchthaler, H. Germ, R. Pippan, F. Riemelmoser, J. Stampfl and J. Wei (1996) *Acta Metallurgica et Materialia* **44**, 3307.
- 5.43 Krasowsky A.J. and V. A. Stepanenko (1979) *International Journal of Fracture* **15**, 203.
- 5.44 Bauer B. and A. Haller (1981) *Practical Metallography* **18**, 327.
- 5.45 Exner H.E. and M. Fripan (1985) *Journal of Microscopy* **139**, 161.
- 5.46 Kobayashi T. and J. H. Giovanola (1989) *Journal of Mechanics and Physics of Solids* **37**, 759.
- 5.47 Gruber M. and O. Kolednik (1992) in *International Archives of Photogrammetry and Remote Sensing, Proc. of ISPRS XVII* (edited by L. W. Fritz and J. R. Lucas). Vol. 29, Part B5, Commission V, pp. 305-310.

- 5.48 Bryant D. (1986) *Micron Microscopy Acta* **17**, 237.
- 5.49 Kobayashi T. and D. A. Shockey (1987) *Metallurgical Transactions* **18A**, 1941.
- 5.50 Gruber M. and W. Walcher (1994) in *International Archives of Photogrammetry and Remote Sensing, Proc. of ISPRS XVIII* . Vol. 30, Part 3/1, pp. 311–315.
- 5.51 Gerberich W. W. and E. Kurman (1985) *Scripta metallurgica* **19**, 295.
- 5.52 Kolednik O. and P. Kutleša, *Engineering Fracture Mechanics* **33**, 215.
- 5.53 Shan G. X. , O. Kolednik, F. D. Fischer and H. P. Stüwe (1993) *Engineering Fracture Mechanics* **45**, 99.
- 5.54 Dawicke D.S., R. S. Piascik and J. C. Newman, Jr. (1997) *ASTM STP* **1321**, 309.
- 5.55 Yan W.-Y. , G.X. Shan, O. Kolednik and F. D. Fischer (1998) *Key Engineering Materials* **145-149**, 179 .
- 5.56 Kolednik O. and H. P. Stüwe (1989) *International Journal of Fracture* **33**, R63 (1987).

## 5.9 Some Remarks on the Reversibility of Fracture Energies

In a fracture experiment external energy which is provided by the testing machine, is transformed into elastic and plastic strain energy of the specimen and into surface energy. Most of the plastic strain energy is dissipated; only a small fraction, say 5%, is used to enhance the dislocation density in the plastic zone. This fraction of plastic energy could be recovered by annealing, thus it is strictly speaking a reversible energy. However, we have to treat it as a non-reversible energy when considering the energy balance in a usual fracture experiment, unless the specimen is broken at such high temperatures that the material may recover.

When plastic flow occurs at the crack tip some portion of the elastic strain energy becomes non-reversible on unloading but remains as residual elastic energy,  $W_{el,nr}$ , in the specimen. If the specimen bursted into thousands of tiny pieces during fracture this energy would be reversible and would act as an additional driving force for fracture.

## 5.10 The Relation between R and COA

The relation between the total crack growth resistance,  $R_{tot}$ , and the slope of the  $J-\Delta a$  curve was presented already in [5.8, 5.38]. The derivation shall be repeated here briefly.

Differentiation of the  $J$ -evaluation formula, Eq.(5.7), with respect to the crack extension leads to

$$\frac{dJ}{d(\Delta a)} = \frac{\eta}{bB} \frac{dU}{d(\Delta a)} \quad (5.15)$$

For small  $\Delta a$  the error made by assuming that  $b$  and  $\eta$  remain constant is negligible. After the plastic limit load has been reached the elastic strain energy remains approximately constant, and  $dU = dW_{el} + dW_{pl,tot} \approx dW_{pl,tot}$ . Thus, Eq.(5.15) can be extended to

$$\frac{dJ}{d(\Delta a)} \approx \frac{\eta}{bB} \frac{dW_{pl,tot}}{d(\Delta a)} = \frac{\eta}{b} R_{tot}, \quad (5.16)$$

This relation holds for deeply notched bend and CT specimens.

To derive the relation between  $R_{tot}$  and the crack-opening angle we need the relationship between the  $J$ -integral and the crack opening displacement,

$$J = m\sigma_y COD. \quad (5.17)$$

It shall be remarked that in Eq.(5.17)  $COD$  denotes the crack opening displacement at the position of the fatigue pre-crack (in contrary to the crack-tip opening displacement,  $CTOD$ , at the current crack tip position). The factor  $m$  depends primarily on the strain-hardening exponent of the material. For many materials, e.g. medium-strength steels,  $m = 2$  is a quite good approximation, but usually not for low-strength materials with high strain-hardening exponent. It was demonstrated, [5.56], that Stüwe's estimate of the mean flow stress, Eq.(5.12), can be used to evaluate  $m$  from the tensile test data,

$$m = \frac{\sigma_u}{\sigma_y} \frac{\exp(n)}{(1+n)n^n}. \quad (5.18)$$

By differentiating Eq.(5.17) with respect to  $\Delta a$  and substituting Eq.(5.16) we get

$$COA = \frac{dCOD}{d\Delta a} \approx \frac{\eta}{m\sigma_y b} R_{tot}. \quad (5.19)$$

$COA$  is the crack opening angle measured at the initial tip position (in contrary to the current tip value,  $CTOA$ ).



---

# ELECTRO-DISCHARGE MACHINING OF MESOSCOPIC PARTS WITH ELECTROPLATED COPPER AND HOT-PRESSED SILVER TUNGSTEN ELECTRODES

**J.Stampfl, R.Leitgeb, Y.-L. Cheng, F.B. Prinz**

*Journal of Micromechanics and Microengineering*, 10:1-6, 2000

**Abstract.** Recent advances in the development of plasma etchers for silicon brought machines to the market which are able to etch silicon with high etch rates ( $> 5\mu\text{m}$  per min) at high anisotropy (taper of sidewalls  $< 1.5^\circ$ ). Micromachined silicon is therefore not only suitable for applications in micromechanics but it can also fill the gap which exists between conventional macro-machining (milling, turning) with feature sizes usually  $> 1\text{mm}$  and micro electro-mechanical systems (MEMS) with feature sizes  $< 100\mu\text{m}$ .

In this work micromachined silicon is used as a mold for electroplating copper and for hot-pressing silver tungsten. After removing the silicon, the copper or silver-tungsten is used as electrode for electro discharge machining (EDM). Using these process steps nearly any conductive material can be shaped, especially magnetic materials like amorphous metal which are difficult or impossible to machine otherwise. The fabrication of the electrodes is described as well as the influence of the electrode material on the achieved quality of the final part.

## 6.1 Introduction

---

Electro discharge machining (EDM) is a widely used method for shaping conductive materials. EDM removes material by creating controlled sparks between a shaped electrode and an electrically conductive work piece. As part material is eroded, the electrode is slowly lowered into the work piece, until the resulting cavity has the inverse shape of the electrode. Dielectric fluid is flushed into the gap between electrode

and work piece to remove small particles created by the process and to avoid excessive oxidation of part surface and electrode.

The applications of EDM lie mainly in the tooling industry where it is applied on materials which are too hard to be machined with conventional techniques like milling or turning. The parts for these applications are usually larger than 1 mm, therefore conventional methods can be applied for fabricating the electrodes. Due to the fact that EDM can achieve very fine surface finishes, it has been tried to apply it for micromachining of conductive materials. For this purpose, copper electrodes obtained by LIGA (Lithographie Galvanoformung Abformung) have been used as die-sinking electrodes [6.1]. A related technique, wire electrodischarge grinding (WEDG) is also capable of fabricating parts with feature sizes below  $100\mu\text{m}$  [6.2, 6.3].

A few alternative methods exist for creating fine patterns in engineering materials. Wire EDM moves a fine wire, which is used as electrode, through a sheet of part material and moves it along a programmed path. It can reach excellent surface finish, however, it is limited to parts with straight side walls. It can not create blind holes, and requires highly accurate positioning equipment.

Laser cutting (ablation) has been adapted for micro machining. Instead of electrical sparks, short laser pulses are used to selectively vaporize part material. This method does not require shaped electrodes, but, just like wire EDM relies upon highly accurate actuators to move the laser over the part surface. The laser pulse rate is substantially lower than the spark pulse rate of micro-EDM machines, which makes the process much slower.

The aim of this work is to show that the application of silicon micromachining in combination with EDM can extend the range of feasible sizes of parts manufactured with Shape Deposition Manufacturing (SDM) [6.4, 6.5] by at least one order of magnitude into the mesoscopic range (part or feature size between  $100\mu\text{m}$  and 1mm). For most applications of SDM silicon itself is not a suitable material due to its low fracture toughness and poor electrical and magnetic properties. In order to be able to use engineering materials, silicon therefore serves as a mold for the following processing, in this case as mold for EDM electrodes. The EDM electrodes are then used to shape amorphous metal, a soft-magnetic material which is sufficiently conductive for being shaped with EDM. Amorphous metal is delivered in the form of thin sheets (thickness  $25\mu\text{m}$ ) and it is difficult to process with conventional techniques.

Two ways to obtain EDM electrodes for mesoscopic structures are described in the following sections. In Figure 6.1 the process steps necessary to get the final part are depicted schematically. By electroplating copper into plasma-etched silicon with sufficient conductivity, one can get a copper electrode which replicates the silicon mold. The second way to fabricate mesoscopic electrodes is by hot-pressing of metal powder into the silicon mold. Both alternatives are described.

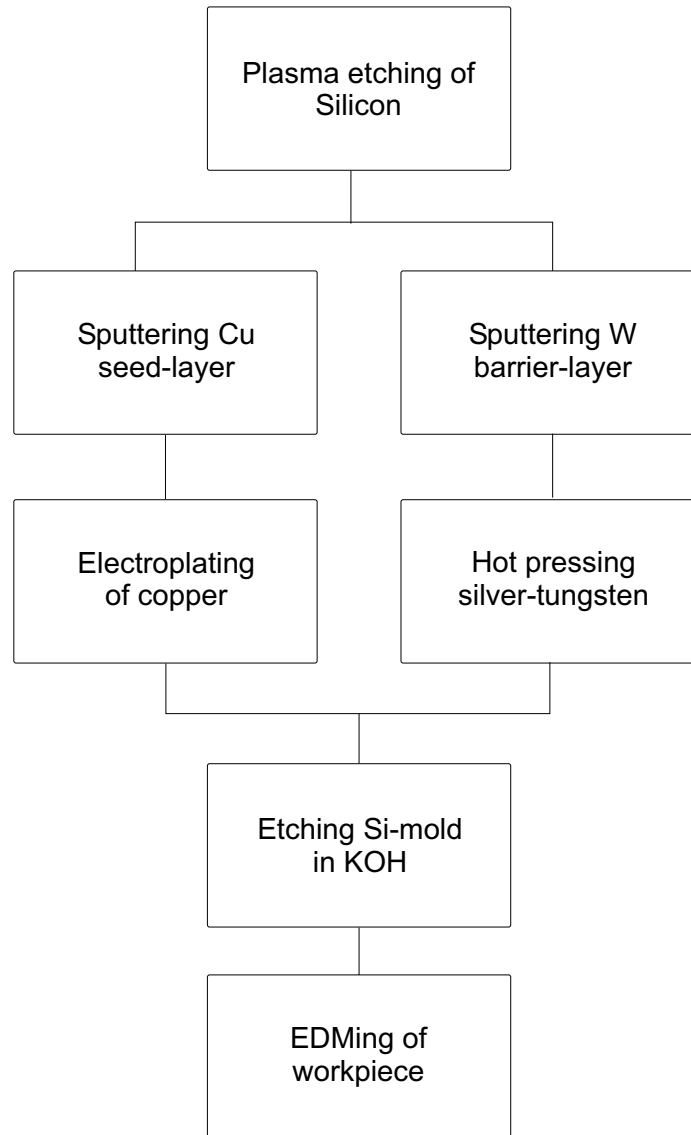


**Figure 6.1:** Process steps for the fabrication of plated and hot-pressed electrodes

## 6.2 Preparation of silicon molds

To keep the software interface for the fabrication of mesoscopic parts compatible with the CAD (Computer Aided Design) software used in SDM, a software package was developed to slice CAD models and translate the layer information into CIF (Caltech Interchange Format) format, a widely used standard for the description of photolithography masks. Using these photomasks the Si-wafer (thickness between  $100\mu\text{m}$  and  $500\mu\text{m}$ , and diameter  $100\text{mm}$ ) was patterned with photoresist ( $7\mu\text{m}$  thickness). Highly-doped silicon in the (100) orientation with a resistivity of  $0.001\ \Omega\text{cm}$  was used in order to have a conductivity high enough for the following electroplating. The wafer then was etched in a reactive ion etcher (STS Multiplex ICP Deep RIE) with  $\text{C}_4\text{F}_8$  as etch gas and  $\text{SF}_6$  as passivation gas for the sidewalls. The etch rate was  $4\mu\text{m}/\text{min}$

and the etch selectivity between resist and silicon better than 80:1. With these etching parameters the taper of the sidewalls was less than  $1.5^\circ$ . After dicing the wafer into square pieces (20mm by 20mm), a thin layer of copper was sputtered as seed layer for electroplating (see the next section) and a tungsten layer was sputtered as diffusion barrier onto the wafer-pieces which were used for hot pressing. To promote the adhesion between silicon and copper or tungsten, respectively, the silicon was first coated with a thin (300nm) titanium layer. In Figure 6.2 a scanning electron micrograph of a plasma etched silicon mold is shown.

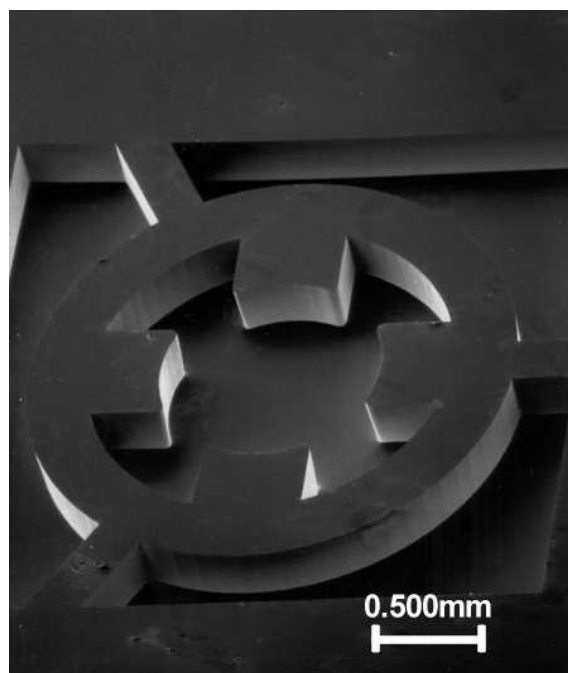


**Figure 6.2:** Scanning electron micrograph of plasma-etched Si-mold.

## 6.3 Electroplating

---

Electroplating of microstructures is widely used in combination with optically or X-ray patterned thick resist. In combination with silicon, electroplating has been used to fabricate tools for injection molding and hot embossing [6.6]. For this work, copper has been plated onto silicon molds in order to fabricate EDM electrodes. Due to its high thermal conductivity, copper is widely used for spark erosion. Furthermore, it is one of the materials which are relatively easy to electroplate.

After sputtering the seed layer onto the plasma-etched silicon-mold (Figure 6.2) and removing a residual oxide layer with Metex-9268, these molds were put into an acid copper electroplating solution. A pulse-reverse current source delivered the plating current at a current density of  $30\text{mA}/\text{cm}^2$ . With these settings a deposition rate of  $25\mu\text{m}/\text{hr}$  has been achieved.

After electroplating, the silicon was etched away in an aqueous solution of potassium hydroxide at temperatures between  $85^\circ\text{C}$  and  $100^\circ\text{C}$ . In Figure 6.3 the final electro-

plated part, obtained from the mold in Figure 6.2, is shown. The height of the structure in Figure 6.3 is  $250\mu\text{m}$ .

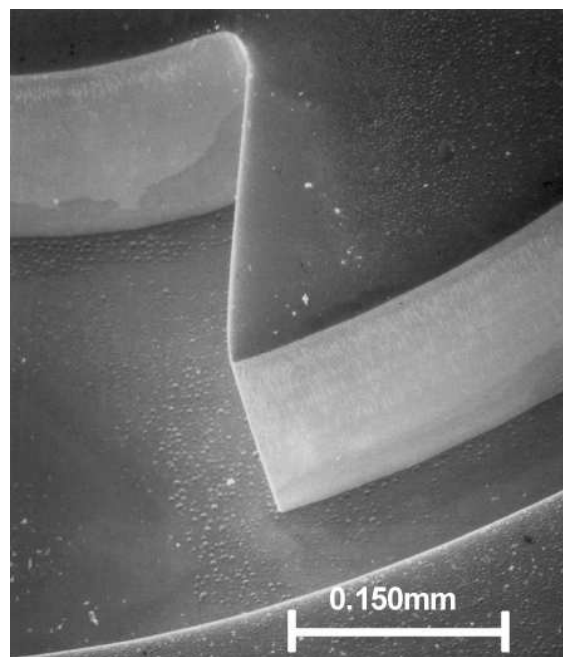
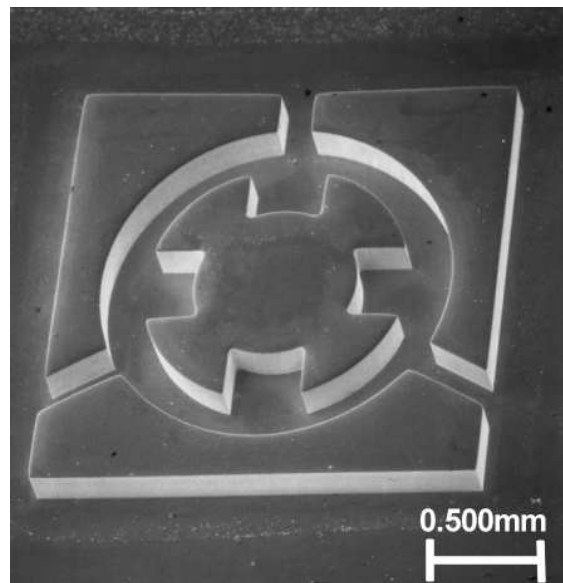


**Figure 6.3:** Scanning electron micrograph (full and detailed view) of electroplated copper electrode.

## 6.4 Hot-pressing of metal powder

---

The ideal material for EDM electrodes are high melting-point materials like graphite or tungsten. Both of them cannot be used in combination with silicon because their

processing temperature lies above the melting point of silicon. But tungsten in combination with silver or copper has widely been used as contact material in applications like electrical switches or rocket nozzles. In these materials the high melting point of tungsten is combined with the excellent thermal conductivity of silver and copper. It can therefore be expected to be a suitable material for EDM-electrodes. AgW and CuW can either be processed by hot-pressing blended powder or by infiltrating a green tungsten part with liquid silver or copper [6.7].

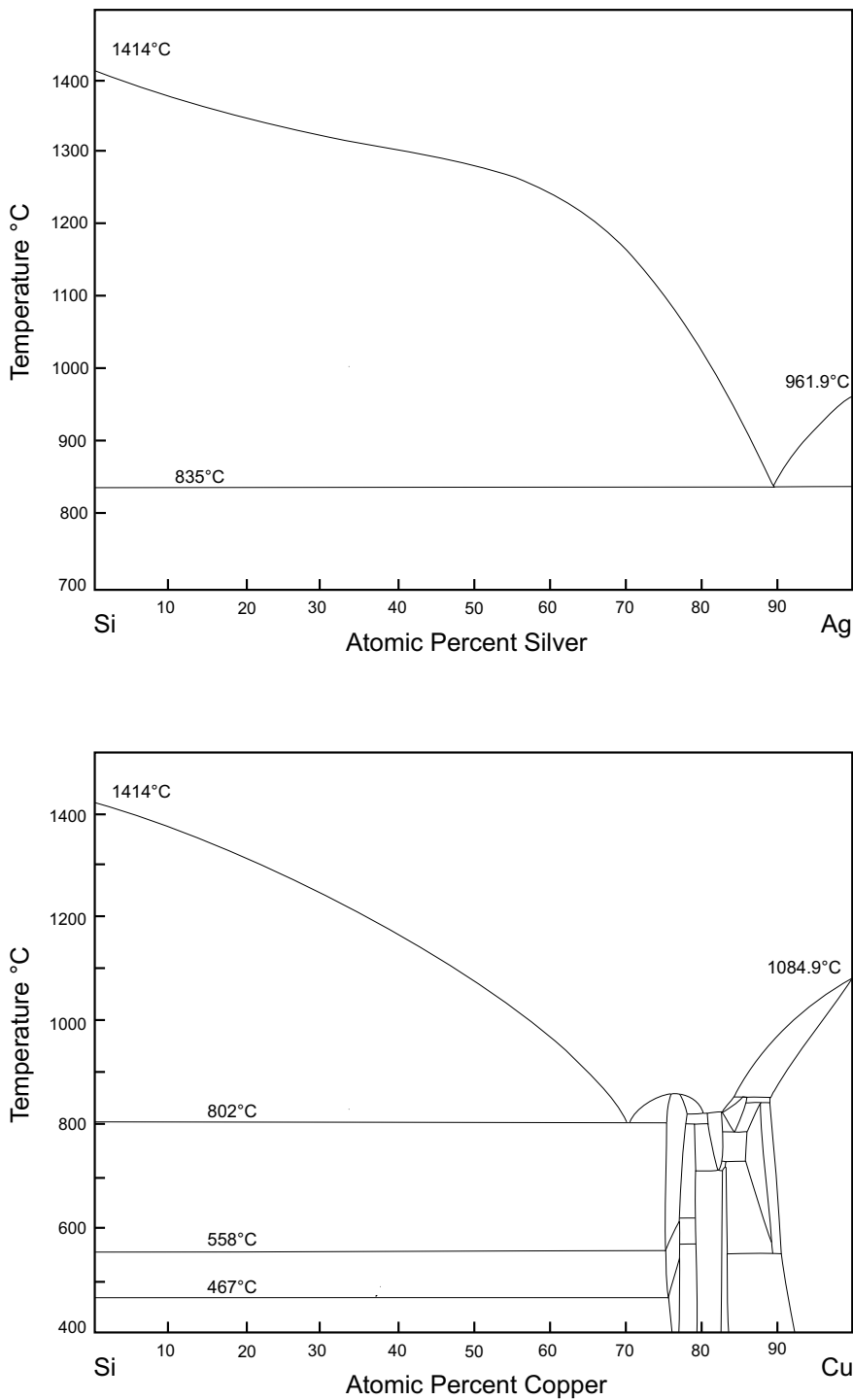
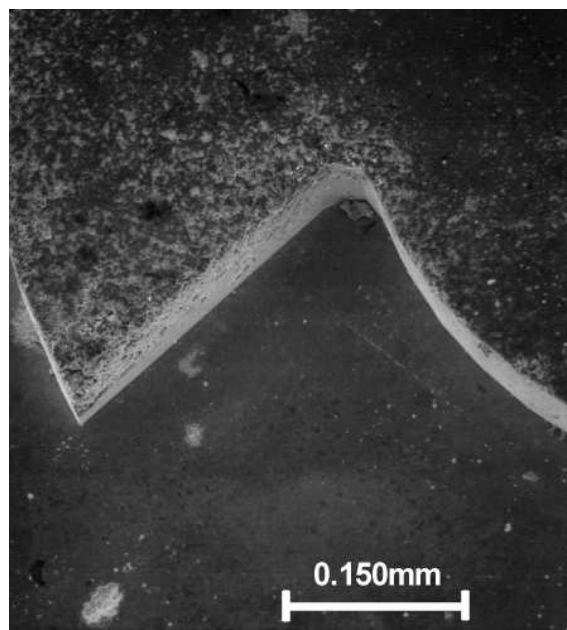
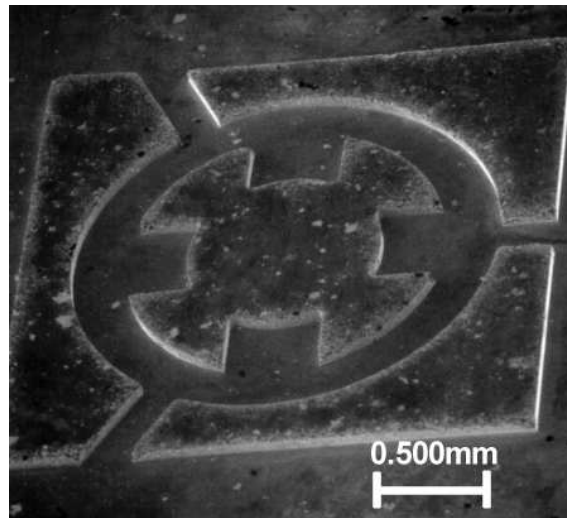


Figure 6.4: Binary phase diagram for Si-Ag and Si-Cu from [6.10].

When using these materials in combination with a silicon-mold, one has to consider the phase diagrams of Si-Ag and Si-Cu, respectively. Silver as well as copper are known to destroy electronic devices by diffusion into the bulk silicon. Recent advances in diffusion barriers [6.8] allow the use of copper in integrated circuits, but especially at elevated temperatures ( $> 750^{\circ}\text{C}$ ) [6.9] these barrier layers tend to fail.



**Figure 6.5:** Scanning electron micrograph (full and detailed view) of hot-pressed AgW electrode.

Since copper as well as silver form a low melting eutecticum [6.10] with silicon (see Figure 6.4), infiltration of the green tungsten part with liquid silver or copper would melt the silicon mold. Therefore only hot-pressing of blended powder is a viable way to sinter EDM-electrodes from metal powders. For two reasons AgW is more suitable

for this application than CuW: First, the eutectic temperature of Ag-Si (835°C) is closer to the melting point of silver (961°C) than the eutectic temperature of Cu-Si (802°C) is to the melting point of copper (1084°C). Hot-pressing of AgW can therefore be done at temperatures significantly closer to the melting point, where silver is already very soft.

Secondly, copper forms various alloys with silicon even at temperatures well below the eutectic temperature (see Figure 6.4). Due to rapid diffusion of copper in silicon, copper tends to form an alloy with the silicon of the mold during sintering and the mold is destroyed. In contrast to copper, silver is nearly insoluble in solid silicon and therefore does not penetrate the mold during hot-pressing.

All hot-pressing experiments were done with a conventional 10 tonne hot-press in a graphite die at a temperature of 750°C and pressures of 30MPa. The pressing time was one hour. The powder was made of 33% (weight percent) tungsten and 67% silver. Prior to pressing the powders were mixed in a steel viable with steel balls. The viable was agitated in a Spex mill. The particle size of the powders used was between 1 $\mu$ m and 5 $\mu$ m. The final density of the AgW part was around 93% of the theoretical full density. The powder replicates the mold sufficiently well, as can be seen from Figure 6.5. The hot-pressing temperature and the applied pressure were low enough to avoid plastic deformation of the silicon, which has been observed at temperatures above 800°C [6.11], [6.12].

## 6.5 Electro discharge machining

---

The above described electrodes were used for EDMing commercially available sheets of amorphous metal. Two different alloys (Metglass 2605Co from Allied Signal and Vitrovac 6025 from VAC) were investigated, both materials yielded similar results. The material was chosen because of its high magnetic permeability and saturation density. It is supposed to be used for the stator of an electromagnetic motor.

For EDMing a Moldmaster M45-B machine was equipped with a current-reducing head to decrease the spark energy. With an energy of 40  $\mu$ J/spark surfaces as shown in Figure 6.6 are obtained.

The discharge energy of the individual sparks determines the resulting surface finish and also the material removal rate. For rough machining of large tools discharge pulse energies up to a few Joule can be used, whereas finishing operations require discharge energies in the lower milli Joule level, with pulse repetition rates of a few kHz. With a special adapter head we could reduce the discharge energy for our setup down to 40 $\mu$ J. With special micro EDM controllers the discharge energy per pulse can be reduced below one  $\mu$ J, and much higher pulse repetition rates (several hundred kHz) can be reached.

The depth of the remolten material (measured by optical microscopy of the EDMed workpiece) is around 3 $\mu$ m. During the solidification of the remolten zone the amorphous structure of the material gets lost and is replaced by a thin crystalline layer. The

surface finish is (depending on the spark energy and the control settings) between  $2\mu\text{m}$  and  $5\mu\text{m}$ . These values can be considered sufficiently low for most applications of mesoscopic devices.

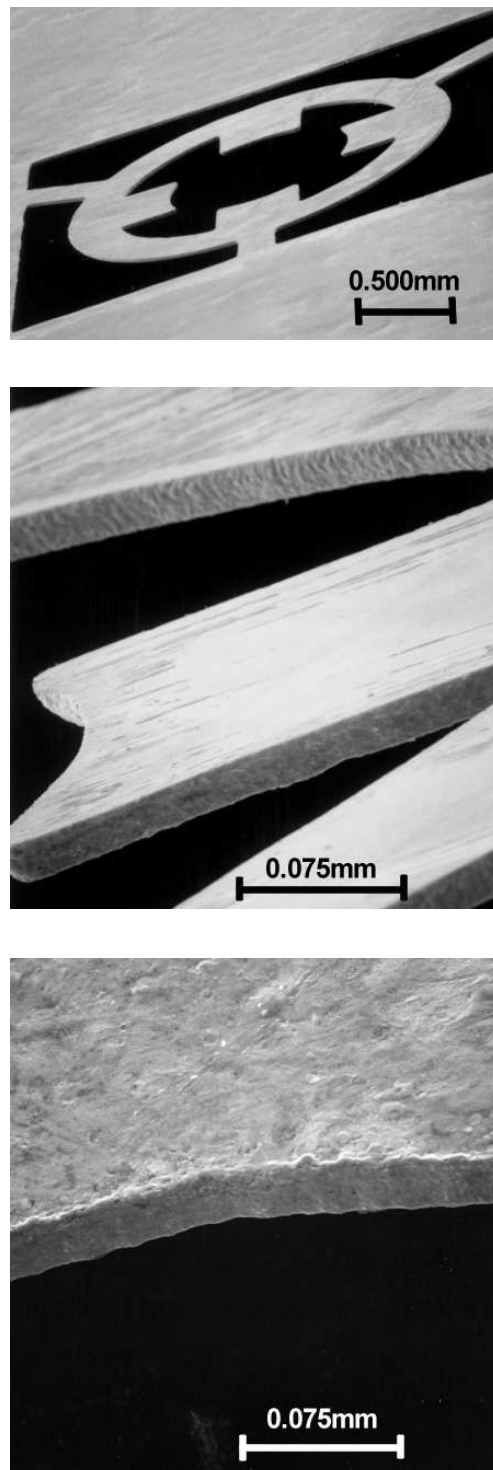


**Figure 6.6:** Scanning electron micrograph (full and detailed view) of amorphous metal EDMed with a plated copper electrode (top and middle). The bottom image shows amorphous metal EDMed with an AgW-electrode

The spark-gap width was found to be  $30 \pm 3\mu\text{m}$ . This value was measured by comparing the dimensions of the original electrode and the final workpiece using optical microscopy. The best tolerances that could be achieved (using the lowest spark energy of  $40\mu\text{J}/\text{spark}$ ) are therefore  $3\mu\text{m}$ . By using an EDM machine especially dedicated to micro-EDM even tighter tolerances could be achieved by decreasing the spark energy. By increasing the spark frequency at the same time, machining times could be kept constant.

The tolerances are slightly higher when using AgW-electrodes since the inhomogeneous distribution of pores leads to a less homogeneous electrode-wear. In contrast, the surface finish of the parts eroded with AgW-electrodes was smoother than when using Cu-electrodes. In Figure 6.6 two sheets of amorphous metal are shown which have been eroded with copper as well as with silver-tungsten electrodes.

## 6.6 Conclusions

---

We have shown two ways to manufacture EDM-electrodes for mesoscopic parts. By using silicon micromachining the feasible part size can be reduced by at least one order of magnitude compared to conventional machining techniques. The electrodes are either made by electroplating of copper or by hot-pressing of silver-tungsten powder. Both methods yield electrodes with comparable properties for spark erosion. The electrodes were used to shape amorphous metal, a material which is hard to machine with conventional techniques.

## Acknowledgments

---

This work was financially supported by the Defense Advanced Research Projects Agency (DARPA) and the National Science Foundation (NSF). Further financial support came from a Schrödinger fellowship (J1486-TEC) of the Austrian Fonds zur Förderung der Wissenschaftlichen Forschung.

We gratefully acknowledge the advice of Joanna Groza and Jung-Man Doh from UC Davis for the preparation of the metal powders. We wish to acknowledge the technical input and support from Claus Goetzl, Katsuhito Sakamoto and Robert DeMattei of Stanford University as well as from Ali Farvid from SLAC .

## 6.7 References

---

- 6.1 W. Ehrfeld, H. Lehr, F. Michel, and A. Wolf. Micro electro discharge machining as a technology in micromachining. In *Micromachining and Microfabrication Process Technology II*, Proceedings of SPIE - The International Society for Optical Engineering v 2879, pages 332–337, 1996.

- 6.2 G. Staufert, A. Dommann, and D. Lauger. Behaviour of a silicon spring fabricated by wire electro-discharge machining. *J. Micromech. Microeng.*, 3:232–235, 1993.
- 6.3 H.H. Langen, T.Masuzawa, and M.Fujino. Self-aligned machining and assembly of high aspect ratio microparts into silicon. In *Proceedings of the 1995 IEEE Micro Electro Mechanical Systems Conference Amsterdam*, pages 250–255, 1995.
- 6.4 R. Merz, F.B. Prinz, K. Ramaswami, M. Terk, and L. Weiss. Shape deposition manufacturing. In H.L. Marcus et al., editor, *Proceedings of the Solid Freeform Fabrication Symposium 1994*, pages 1–8, University of Texas, Austin, August 8-10 1994.
- 6.5 R. Merz and F.B.Prinz. Rapid prototyping of mesoscopic devices. In *Proceedings of the 7th International Conference on Rapid Prototyping, San Francisco*, pages 261–270, 1997.
- 6.6 H. Elderstig and O. Larsson. Polymeric MST - high precision at low cost. *J. Micromech. Microeng.*, 7:89–92, 1997.
- 6.7 C.G. Goetzel. *A treatise on powder metallurgy*. Interscience Publishers, New York, 1949.
- 6.8 S.S. Wong, A.L.S. Loke, J.T. Wetzel, P.H. Townsend, R.N.Vrtis, and M.P. Zussman. Electrical reliability of Cu and low-K dielectric integration. In *Proceedings of the Materials Research Society Spring Meeting San Francisco, CA*, volume 511, pages 317–327, April 1998.
- 6.9 S.S. Wong, C.Ryu, H. Lee, and K-W. Kwon. Barriers for copper interconnections. In *Proceedings of the Materials Research Society Spring Meeting, San Francisco, CA*, volume 514, pages 75–81, April 1998.
- 6.10 T.B. Massalski, editor. *Binary alloy phase diagrams*. ASM International, Materials Park, Ohio, 1990.
- 6.11 J.R. Patel and A.R. Chaudhuri. Macroscopic plastic properties of dislocation-free germanium and other semiconductor crystals. I. Yield behaviour. *J. Appl. Phys.*, 34:2788–2799, 1963.
- 6.12 M.A. Huff, A.D. Nikolich, and M.A. Schmidt. Design of sealed cavity microstructures formed by silicon wafer bonding. *J. Micromech. Microeng.*, 2:74–81, 1993.



---

# RAPID PROTOTYPING AND MANUFACTURING BY GELCASTING OF METALLIC AND CERAMIC SLURRIES

**J. Stampfl H.C. Liu, S.W. Nam, K. Sakamoto, H. Tsuru, S. Kang, A. G. Cooper,  
A. Nickel, F. B. Prinz**

*Materials Science and Engineering A334:187-192, 2002*

**Abstract.** In this work an approach for Rapid Prototyping and Manufacturing of metallic as well as ceramic parts is presented. By using Mold Shape Deposition Manufacturing (Mold SDM) a wax mold is fabricated which is filled with a slurry containing the final part material in powder form. The wax mold is manufactured by first decomposing the desired part geometry into machinable compacts. In a next step the mold is built up in a series of layers by machining either the wax or a sacrificial support material. The surface quality of the final mold is only limited by the abilities of the CNC machine.

After casting a ceramic or metallic slurry, the wax mold is removed and the obtained green part debinded and sintered. In this work the mechanical and microstructural properties of the parts obtained by this method are presented. The materials which have been investigated are silicon nitride and stainless steels.

Due to the high mold quality the process is suitable for a variety of applications in Rapid Prototyping and Manufacturing where parts made of engineering materials are required.

## 7.1 Introduction

---

A wide variety of commercially available systems for Rapid Prototyping (RP) enables the user to fabricate prototypes with almost any shape and in a large range of different sizes. The focus of most of these systems, like stereolithography (SLA) and fused deposition modeling (FDM), is to produce plastic prototypes with a high geometric

quality. Most RP techniques put less emphasis on material issues, and if they do [7.1], [7.2], it is not easy to switch between different materials. In this work we introduce an approach where an RP wax mold is fabricated in a first step. In a second step the wax mold is used to transfer the shape into the final part material. Mold SDM (Mold Shape Deposition Manufacturing) [7.3] is used to fabricate the wax mold which is then filled with a metallic or ceramic gelcasting slurry. The main focus of this investigation is on parts made out of silicon nitride and stainless steel.

## 7.2 Mold SDM

---

Mold SDM [7.3] is an additive-subtractive layered manufacturing process for fabricating fugitive molds which can then be used to make parts using castable materials such as ceramic gelcasting [7.4] [7.5] slurries and thermoset polymers [7.3]. Fig. 7.1 (a) is an example process sequence for the fabrication of a simple part using Mold SDM. Molds are currently fabricated from a variety of waxes. These are deposited by casting and are shaped by either 3- or 5-axis computer numerical control (CNC) milling. The mold is constructed layer by layer in steps 1 through 8. Each step represents one material deposition and shaping cycle. The support material is removed in step 9 and the part material is cast in step 10. After removal of the mold in step 11 finishing operations, such as casting feature removal, are performed leaving the finished part in step 12. Processes such as sintering can be performed at any time after mold removal.

A typical cross section of a wax mold, which was made using Mold SDM, is shown in Fig. 7.1 (b). The water soluble support material has already been etched out.

Two features of the Mold SDM process are advantageous for the fabrication of complex structural ceramic components:

- all surfaces are either machined or replicated from machined surfaces resulting in smooth accurate geometry, and
- the part material is cast monolithically so there will be no layer boundaries, which are potential sources of defects, in the final part.

Both of these advantages are particularly important for flaw sensitive materials where surface roughness and internal defects can significantly reduce the part strength. Defects in the mold can arise from incomplete bonding between wax layers, or foreign particles or voids trapped at the layer boundaries.

## 7.3 Gelcasting

---

Gelcasting [7.4] is a molding technique for ceramic and metallic materials. The gelcasting slurry is obtained by mixing the part material in powder form into a liquid which consists of the following constituents: A solvent (either water or an organic solvent), one or several types of monomers, an initiator and in some cases an accelerator.

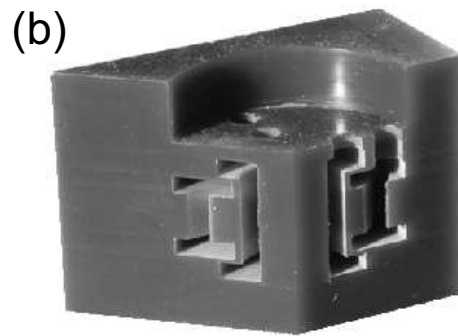
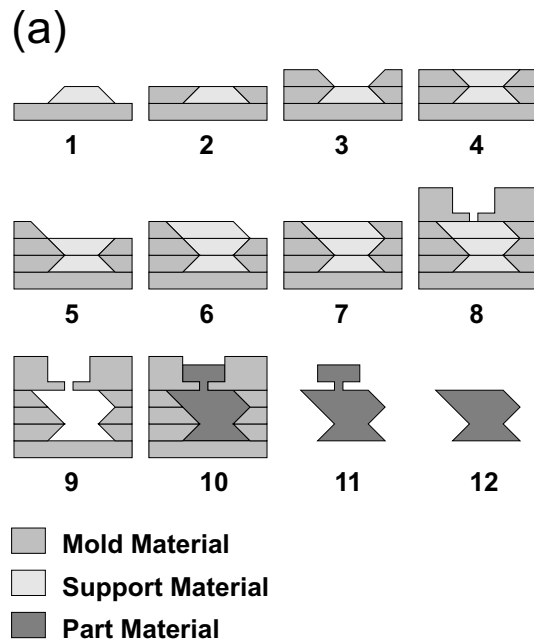


**Figure 7.1:** Processing steps for Mold SDM (a) and section of wax mold (b).

### 7.3.1 Slurries

For this investigation three different base formulations for slurries were used. A water based formulation developed at Oak Ridge National Lab (ORNL) [7.4] and two solvent based formulations from Advanced Ceramics Research (ACR, Tucson, AZ) and SRI International (Menlo Park, CA), respectively. The solvent based formulations are proprietary, whereas the water based formulation from ORNL is patented [7.6] and published [7.7].

The water based formulation was mainly used in combination with metallic powders. It can also be used for gelcasting of ceramics, but the interaction between water and the large surface of the ceramic particles decreases the shelf life of the slurries. For ceramic slurries the organic formulations are easier to use and give more easily reproducible results.

The casting procedures are similar for all types of slurries: After agitating the slurries

for several hours to obtain a homogenous mix, initiator and/or accelerator are added to start the polymerization process. The slurry is then cast into an evacuated wax mold where the polymerization process continues until the liquid slurry is completely solidified. The wax is molten off to obtain the green part which is then debinded and sintered.

Evacuation of the mold helps to avoid voids due to entrapped air and prohibits flaking of the green part surface. Flaking occurs if the slurry gets into contact with oxygen that can inhibit polymerization of the slurry. After drying, unpolymerized, "oxygen contaminated" layers of slurry peel off and leave the green part damaged. Many commercially available waxes contain antioxidants which can inhibit polymerization of the slurry, too. It is therefore necessary to choose a wax without polymerization-inhibiting additives. At the same time the wax must be machinable and the melting point should be between 80°C and 100°C. If the melting point is much lower, the mold can melt during gelling, if it is much higher the green part can be damaged during melting off the wax mold. The waxes used in this work were supplied by Kindt-Collins (Cleveland, OH). For most parts a wax blend which was derived from Kindt-Collin's Master File-a-wax and Master Protowax gave good results. Both wax types were used without antioxidants or coloring agents.

In general the ceramic slurries are less viscous at the same solid loading than the metallic slurries. They are therefore easier to cast. Settling of the powder particles is also more critical in the case of metallic slurries (due to the higher density of most metals). But with the right precautions (correct solid loading, fairly short gelling time) this problem can be avoided, for metals too.

For the metallic slurries, gas atomized powder of a precipitation hardening steel (17-4 PH, composition see Tab. 7.3) was used. Two different types of slurries were prepared: one with -20 micron powder and one with -44 micron powder, respectively. In both cases similar solid loadings of around 50 vol% were achieved.

The ceramic slurries were composed of 88 weight%  $\text{Si}_3\text{N}_4$ , 9 weight%  $\text{Y}_2\text{O}_3$  and 3 weight%  $\text{Al}_2\text{O}_3$ . The fairly high content of oxide ceramics simplifies the sintering process. At the same time the high oxide content will degrade the mechanical properties at elevated temperatures [7.8]. To achieve a higher solid loading, a bimodal silicon nitride powder with  $D_{50}=0,5 \mu\text{m}$  and  $D_{50}=0,7 \mu\text{m}$  was used. The overall solid loading for the silicon nitride slurries was 52 vol%. The linear shrinkage during sintering is around 18% [7.5], and the tolerances due to irregular shrinkage can in most cases be kept at variations lower than 1% of the final dimensions. An example of a green and sintered ceramic turbine is shown in Fig. 7.2.

The metallic parts were debinded under nitrogen and further sintered in a mixture of argon and hydrogen at temperatures up to 1250°C. The ceramic parts were debinded in air and sintered in nitrogen at 1750°C.

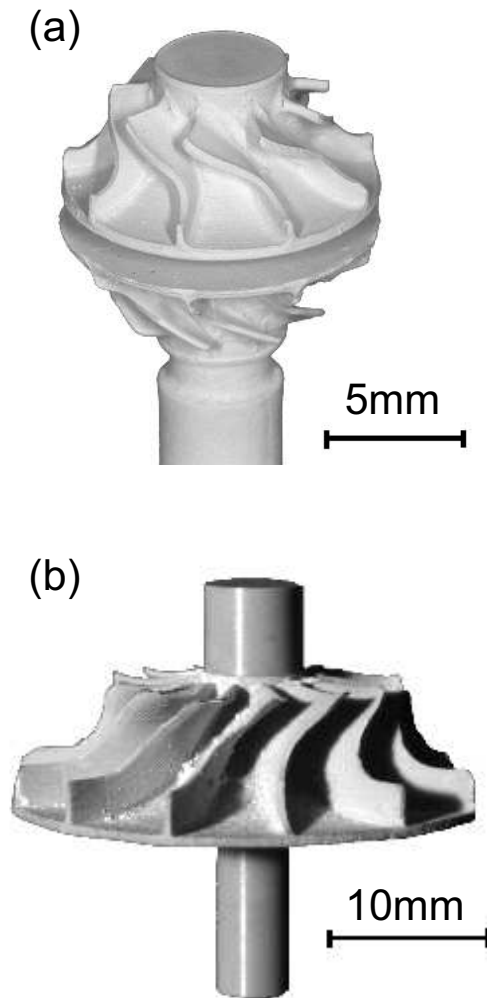


**Figure 7.2:** Green (a) and sintered (b) silicon nitride turbine.

### 7.3.2 Microstructure

Especially in the case of silicon nitride, the control of the microstructure is crucial for the quality of the final part. Since for applications in Rapid Prototyping most surfaces of the sintered part cannot be further machined or ground to get the net-shape, the surface microstructure has to be considered in addition to the bulk microstructure. The final surface roughness of the sintered part is determined by two factors: The original particle size and the amount of grain growth of the  $\beta$ -needles which build up during the  $\alpha - \beta$ -phase transformation. By adjusting the sintering atmosphere in a way that inhibits the grain growth on the surface, the surface roughness can be kept low. At the same time the phase transformation can occur in the bulk material to achieve the needle-like microstructure which determines the mechanical strength and toughness of the material.

In Fig. 7.3 SEM (scanning electron microscopy) micrographs of the bulk and surface microstructure are shown. The bulk microstructure, which was prepared by etching a

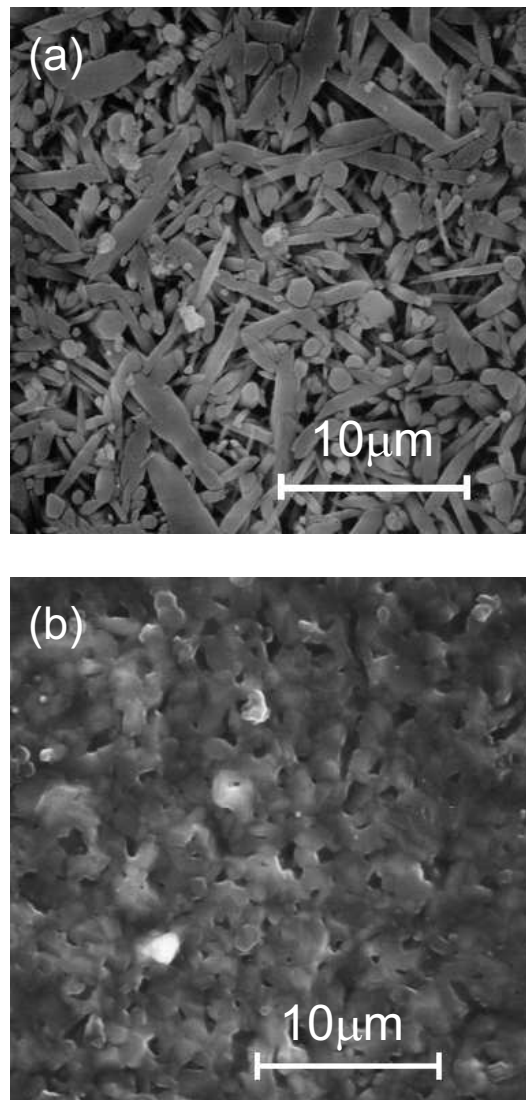


**Figure 7.3:** Microstructure of sintered silicon nitride in the bulk material (a) and on the surface (b).

polished sample in liquid sodium hydroxide (Fig. 7.3(a)) shows the typical  $\beta$ -needles in a glassy matrix. Due to the inhibited grain growth on the surface (Fig. 7.3(b)), the individual powder particles sinter together to form a fairly smooth surface. The root mean square (RMS) surface roughness of the final part is between 0.5  $\mu\text{m}$  and 1.8  $\mu\text{m}$  [7.5].

### 7.3.3 Micromachined molds

Progress in the field of macro-manufacturing (CNC machining, Rapid Prototyping, ..) and micromachining (plasma etching, lithographic techniques) is beginning to close a gap that used to be very large: The macro-world (part or feature size  $>1\text{mm}$ ) usually deals with a wide variety of materials in complex shapes whereas the micromachined parts are made out of a limited number of materials (mostly originating from semicon-

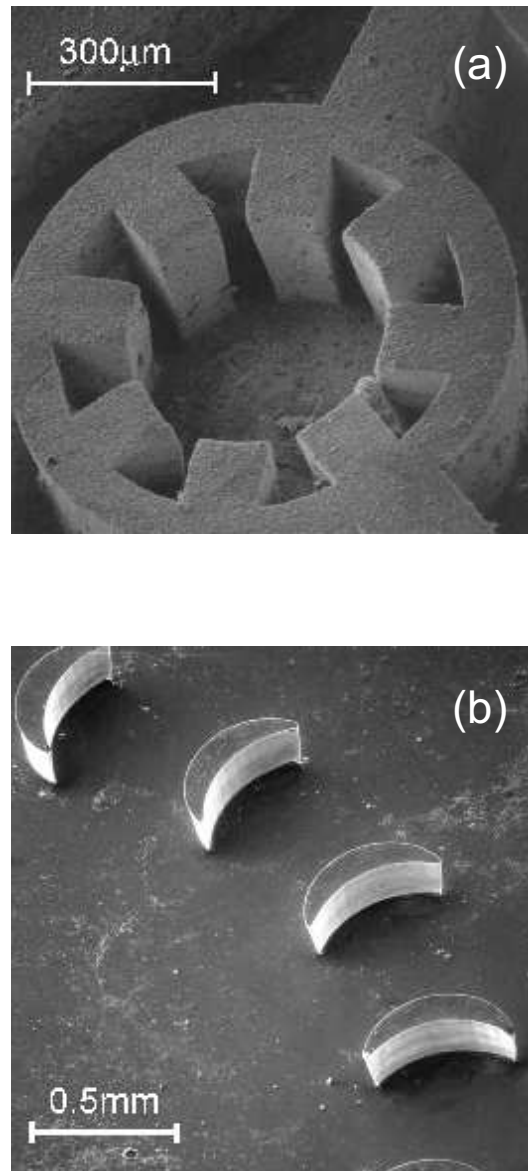


**Figure 7.4:** Sintered test structure (a) and green turbine wheel (b) made out of gel-cast silicon nitride.

ductor processes) in fairly simple shapes. Since gelcasting can be used in combination with macromachined as well as with micromachined molds, it is the ideal method to transfer mold-shapes with a wide size-spectrum into a large number of engineering materials [7.9].

Fig. 7.4 shows two parts obtained by gelcasting into a micro-mold (plasma etched silicon). After the slurry had solidified, the mold was removed chemically. The resulting parts replicate the original patterns very well, and the surface smoothness is only limited by the size of the utilized powder particles (as can be seen in Fig. 7.4 (a)). Compared to most conventional manufacturing techniques used for fabrication of microsystems (lithography, plasma etching, electroplating), gelcasting expands the design space due to its ability to fill molds of arbitrary shape, including undercut and non-prismatic shapes. In this work, only simple molds with prismatic and non-undercut features are

**Tab. 7.1.** Mechanical properties. The values for  $\text{Si}_3\text{N}_4$  were measured in 4-point-bending. The value for stainless steel is the tensile strength.

Material	Strength	Density
	MPa	%
$\text{Si}_3\text{N}_4$ unpolished	414	97
$\text{Si}_3\text{N}_4$ polished	950	97
$\text{Si}_3\text{N}_4$ gas press. sint., polished	983	99
17-4 PH stainless steel	900	95

**Tab. 7.2.** Influence of mold surface quality on the mechanical properties of  $\text{Si}_3\text{N}_4$ .

Sample	slurry	Average Strength	Max. Strength
		MPa	MPa
polished	ACR	930	1020
unpolished parallel scallops	ACR	414	600
unpolished perpend. scallops 0.001mm	ACR	406	500
unpolished perpend. scallops 0.005mm	ACR	416	495
unpolished perpend. scallops 0.01mm	ACR	288	360
unpolished perpend. scallops 0.1mm	ACR	231	257
unpolished parallel scallops	SRI	428	550

presented. To fabricate micro-molds with non-prismatic shapes and undercuts, concepts like using water soluble support material, would need to be addressed in the context of micromachining.

## 7.4 Mechanical properties

Since the slurries utilized for this work contain commercially available powders which are sintered according to standard schedules, it can be expected that parts made by gel-casting [7.10] have similar properties like parts fabricated by powder injection molding [7.11]. Table 7.1 gives a summary of the mechanical properties of 4-point-bend samples ( $\text{Si}_3\text{N}_4$ ) and tensile specimens (stainless steel). Due to the ductility of the metallic samples and the brittleness of ceramic samples, the specific surface condition of the tested sample is less critical for metallic specimens than it is for ceramic samples.

In order to get a more complete description of the behavior of ceramic samples,  $\text{Si}_3\text{N}_4$ -beams were tested in the polished and unpolished state (see Table 7.1). All  $\text{Si}_3\text{N}_4$ -samples were sintered at  $1750^\circ\text{C}$  in nitrogen atmosphere. As expected, the polished and gas pressure sintered samples yield the highest strength. All polished samples, independent of the sintering conditions, are stronger than the unpolished samples. Variations of the surface condition (surface roughness, surface microstructure) are therefore more relevant for the overall strength than variations in the bulk structure.

To quantify the influence of the surface roughness, several samples with defined grooves on the surface have been prepared. By machining scallops of defined height into the wax molds, the surface roughness of the final beam can be adjusted. The scallops

were machined parallel or vertical, respectively, to the load line of the beam. Table 7.2 summarizes these results. The beams with the highest average strength are those with parallel scallops. The perpendicular scallops serve as notch and therefore decrease, as expected, the strength. The larger the scallop height, the more the strength decreases. But even the beams with parallel scallops have a significantly lower strength than polished beams. Two types of gels were used for this test, most beams were fabricated using the ACR gel. A second batch of beams, prepared using SRI gel, showed similar results (Table 7.2).

We can therefore conclude that two parameters in addition to the bulk properties determine the final mechanical properties of silicon nitride samples:

- The surface quality of the mold is transferred into the final part. The higher this surface roughness, the lower the final mechanical strength. The defects in the mold surface can cause notches which lead to stress concentrations in the final part. Depending on the applied load, these stress concentrations decrease the strength.
- Even in the case of a perfectly smooth mold surface, the difference between bulk microstructure and surface microstructure has to be considered when describing the mechanical properties of silicon nitride parts. The highest strength that could be achieved with unpolished samples (Table 7.2) is around 600 MPa, well below the 1020 MPa maximum strength of polished samples.



**Figure 7.5:** Sintered stainless steel impeller (left) and polyurethane impeller (right).

**Tab. 7.3.** Chemical composition of 17-4PH stainless steel.

Element	C	Ni	Cr	Mo	Si	Mn
Weight %	0.04	4.21	16.06	0.01	0.41	0.11
	Cu	S	Nb	O	P	Fe
	3.73	0.01	0.26	0.54	0.01	BAL

## 7.5 Conclusion

Gelcasting in combination with Mold SDM is capable of producing parts with complex shapes and well defined microstructural and mechanical properties. By using gelcasting very small parts with fine features can be fabricated (see Fig. 7.4) as well as fairly large parts (Fig. 7.5). Due to the decomposition into machinable compacts, almost any engineering design can be manufactured using Mold SDM. In combination with gelcasting, a wide variety of materials is available. In this work it could be shown that gelcasting offers viable routes for fabricating stainless steel and silicon nitride parts.

The mechanical and microstructural properties of these parts are comparable to those obtained by conventional manufacturing techniques. The materials used for Mold SDM (waxes, water soluble support material) are fully compatible with gelcasting and the combination of these two techniques opens new routes for the short-term fabrication of prototypes and small-scale production quantities of metallic and ceramic parts.

## 7.6 References

- 7.1 N. Harlan, S.-M. Park, D.L. Bourell, and J.J. Beaman. Selective Laser Sintering of zirconia with micro-scale features. In D.L. Bourell, editor, *Solid Freeform Fabrication Symposium 1999*, pages 297–302, University of Texas, Austin, August 9-11 1999.
- 7.2 E. Sachs, S. Allen, C. Hadjiloucas, J. Yoo, and M. Cima. Low shrinkage metal skeletons by three dimensional printing. In D.L. Bourell, editor, *Solid Freeform Fabrication Symposium 1999*, pages 411–426, University of Texas, Austin, August 9-11 1999.
- 7.3 A.G. Cooper, S. Kang, J.W. Kietzman, F.B. Prinz, J.L. Lombardi, and L.E. Weiss. Automated fabrication of complex molded parts using Mold Shape Deposition Manufacturing. *Materials and Design*, 20(2/3):83–89, 1999.
- 7.4 A.C. Young, O.O. Omatete, M.A. Janney, and P.A. Menchhofer. Gelcasting of alumina. *J. Am. Ceram. Soc.*, 74(3):612–618, 1991.
- 7.5 S. Kang, A. G. Cooper, J. Stampfl, F. Prinz, J. Lombardi, L. Weiss, and J. Sherbeck. Fabrication of high quality ceramic parts using Mold SDM. In D.L. Bourell, editor, *Solid Freeform Fabrication Symposium 1999*, pages 427–434, University of Texas, Austin, August 9-11 1999.

- 7.6 M.A. Janney and O.O. Omatete. Method for molding ceramic powders using a water-based gel casting. U.S. patent 5,028,362, 1991.
- 7.7 M.A. Janney. Gelcasting superalloy powders. In *Int. conf. on powder metallurgy in aerospace, defense and demanding applications*, pages 139–146, 1995.
- 7.8 L. Michalowsky. *Neue keramische Werkstoffe*. Deutscher Verlag für Grundstoffindustrie, Leipzig, 1994.
- 7.9 J. Stampfl, H.-C. Liu, S. W. Nam, S. Kang, and F. B. Prinz. Rapid prototyping of mesoscopic devices. In B. Michel, T. Winkler, M. Werner, and H. Fecht, editors, *3rd International Conference on Micro Materials, MicroMat 2000*, Berlin, pages 1073–1078. Verlag ddp goldenbogen, Dresden, 2000.
- 7.10 S. W. Nam, H.-C. Liu, J. Stampfl, S. Kang, and F. Prinz.  $\mu$ Mold Shape Deposition Manufacturing. In S.C. Danforth, D.B. Dimos, and F.B. Prinz, editors, *MRS Spring Meeting, San Francisco*, volume 625 of *MRS Symposium Proceedings*, pages 187–192, April 2000.
- 7.11 R.M. German. *Sintering theory and practice*. John Wiley & Sons, New York, 1996.



---

# CELLULAR SOLIDS BEYOND THE APPARENT DENSITY - AN EXPERIMENTAL ASSESSMENT OF MECHANICAL PROPERTIES

A.WöB, J. Stampfl, P. Fratzl

*Advanced Engineering Materials*, 6:134-138, 2004

**Abstract.** Cellular solids are promising low-density materials and many natural material-structures, such as wood or bone, are based on cellular designs. Their microarchitecture is one of the determining factors for the mechanical behaviour, in addition to the apparent density and the properties of the bulk material. To assess the influence of different periodic microarchitectures independently from the other factors, rapid prototyping was used to fabricate solids with identical bulk material properties and apparent density. The structures were designed with a standard computer aided design software and fabricated using selective laser sintering. They were tested under compression to determine the stiffness, the maximum stress and the energy absorption efficiency, as measures for the strength and the defect tolerance of the structures. It is shown that the design of the elementary cell can account for variations by almost a factor of three in strength and, independently, in defect tolerance.

## 8.1 Introduction

---

Cellular materials are an extremely attractive option to produce stiff materials with low weight. Polymeric [8.1], [8.2], ceramic [8.3] [8.4] or metallic [8.1], [8.5], [8.6] foams are used or considered for a variety of applications ranging from light weight structures to packaging, insulation or crash protection. Nature is using cellular materials to build plant bodies or skeletons, where mechanical support has to be achieved with the smallest amount of material to be synthesized. Hence, wood and cancellous bone are typical examples of cellular materials [8.1].

From a mechanical viewpoint, the primary quantity controlling the properties is the apparent density  $\frac{\rho^*}{\rho_S}$  where  $\rho^*$  is the density of the cellular material and  $\rho_S$  the density

of the corresponding bulk. For three-dimensional elastic open-cell foams both the elastic modulus  $E^*$  and the failure stress under compression  $\sigma^*$  scale with the square of the apparent density:  $\frac{E^*}{E_S} = C_1 \cdot \left(\frac{\rho^*}{\rho_S}\right)^2$  with  $C_1 \approx 1$  and  $\frac{\sigma^*}{\sigma_S} = C_4 \cdot \left(\frac{\rho^*}{\rho_S}\right)^2$  with  $C_4 \approx 0.05$

Metallic open cell foams usually fail by plastic bending rather than elastic buckling of the struts. In this case  $\sigma^*$  scales with a different power of the apparent density  $\frac{\sigma_{pl}^*}{\sigma_S} = C_5 \left(\frac{\rho^*}{\rho_S}\right)^{\frac{3}{2}}$  with  $C_5 \approx 0.3$  [8.1] [8.7]. The apparent density is also the quantity which is primarily considered as a measure to quantify osteoporosis, a wide-spread disease associated with bone loss [8.8], [8.9].

However, for both - medical and engineering applications - it is clear that the apparent density cannot account for all the mechanical effects in cellular materials. The simplest example is the case of the honeycomb structure, where all properties are strongly direction dependent. For instance, the in-plane elastic modulus scales with  $\left(\frac{\rho^*}{\rho_S}\right)^3$  while the out-of-plane stiffness is just linear in  $\frac{\rho^*}{\rho_S}$ . This means that a change in topology at given apparent density can lead to dramatic changes in mechanical properties. This is also clear in the case of osteoporosis where it has long been recognized that the bone density alone cannot fully explain the fracture incidence [8.10], [8.11]. Remarkably, cancellous bone as found, for instance, in the vertebra is far from a random foam structure. As one can see in fig. 8.1, the struts between the pores (called trabeculae) are oriented predominantly horizontally and vertically, that is along the principle stress direction. This effect is sometimes called Wolff-Roux law [8.12], [8.13].

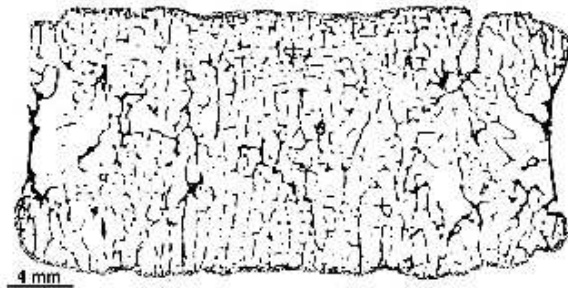


**Figure 8.1:** vertical cross-section through a vertebral body from a 8 years old human. (black = bone, white = bone marrow) [8.14]

A large effort has been devoted in former years to validate the dependency of mechanical parameters on apparent density in a wide range of materials, including technical foams, as well as biological tissues. Nowadays research concentrates on the other parameters of influence, too. The dependency of the compressive properties of open cell aluminium foam on the cell morphology can be found in [8.7], size effects are discussed in [8.15], the effects of the cell wall microstructure is investigated in [8.16] and in [8.17] the influence of wavy imperfections in the cell walls is to be found, just to give some examples.

Moreover, a considerable literature exists on models and computer methods to predict these dependences: Effects of cell irregularity on the elastic properties are modelled in [8.18], metallic foams are compared with soap foams with different unit cells in [8.19],

and in [8.20] the implication of cell face curvature on the stiffness and strength of metal foams is investigated. In [8.21] the topological parameters such as the connectivity of the struts are shown to be important for the stability and the failure mechanism of cellular solids.

## 8.2 Motivation

---

All these arguments point towards the fact that the mechanical properties of cellular materials with a given density can be optimized by changing the internal architecture. There is, however, no systematic experimental investigation on the limits in which variations of mechanical parameters by variation of the internal architecture are possible at given apparent density.

In the present paper we explore this question by an experimental approach in which cellular structures are designed on a computer, built as polymer structures by a rapid prototyping (RP) procedure and finally tested for stiffness and for failure properties. While for small to intermediate deformations the mechanical behaviour can be predicted well, e.g. by finite element methods [8.22], for larger deformations, where nonlinearities play a dominant role, however, computational simulation becomes a quite demanding task [8.23]. Taking the topology of the interior of a vertebra as a starting point, we consider three-dimensional open cellular structures with cubic symmetry modified so as to have struts (or trabeculae) loaded predominantly in compression or in bending. We show that, even at constant apparent density, the failure stress correlates linearly with the stiffness for all structures, while the failure stress and the energy absorption efficiency can be varied independently by about a factor of three just by changing the architecture.

## 8.3 Experimental Method

---

The structures depicted in Fig. 8.2 were designed using the computer aided design (CAD) package ProEngineer. Selective Laser Sintering (SLS) was chosen as manufacturing process for the fabrication of the structures. The SLS process uses a laser beam to selectively sinter polymeric powder particles.

The CAD model is decomposed into thin layers - complying with layers of powder particles in the SLS reaction chamber. Each powder layer is scanned with a laser beam in order to selectively fuse the particles as required by the geometric input. After one layer has been finished, another powder layer is deposited and the process is repeated. After building the structures by the SLS process, the unsintered supporting powder was brushed off to obtain the final part.

Three types of structures were built. The struts of the first one are arranged in a way that leads to bending when loaded, which should result in a high energy absorption efficiency (Gibson-Ashby-structure, compare Fig. 8.2). The second type includes two simple cubic structures (sc and tsc in Fig. 8.2), whose struts are mainly oriented in load-

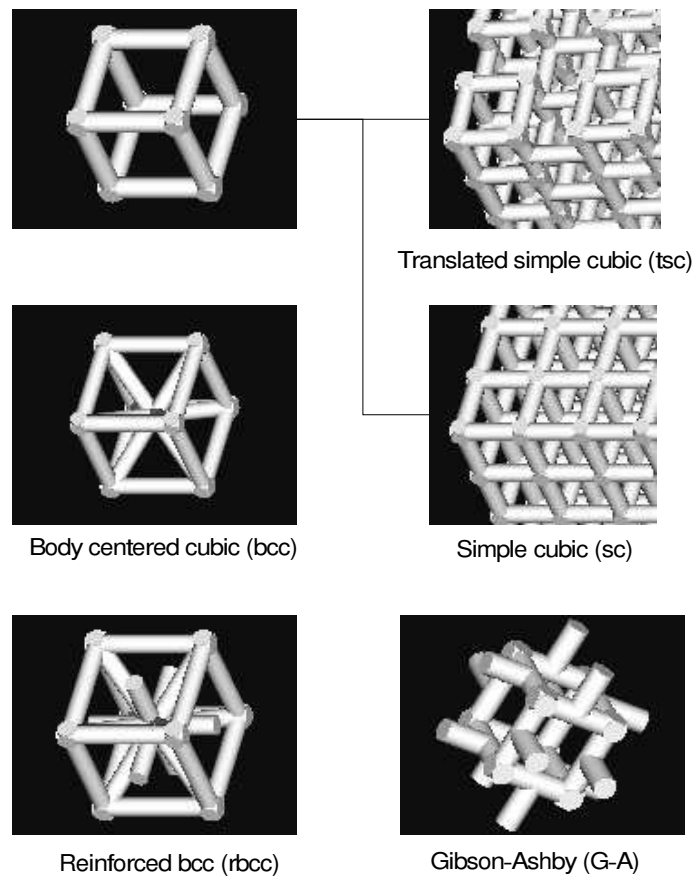


**Figure 8.2:** unit cells of the five structures used for mechanical testing. The translated simple cubic and the simple cubic structure are based on the same unit cell. All other structures (bcc, rbcc, G-A) are just based on the repetition of the unit cell.

ing direction, to provide high stiffness. The third type consists of body centred cubic structures. The high amount of knots and diagonal bracing results in high connectivity and, according to [21] high stiffness and strength (bcc and rbcc in Fig. 8.2).

All structures were built out of the same material (polyamide), they were designed to have the same apparent density ( $\frac{\rho^*}{\rho_S} = 0,175$ ) and outer dimensions ( $5 \times 5 \times 5 \text{ cm}^3$ , corresponding to approximately  $7 \times 7 \times 7$  unit cells for all structures, compare [8.15]). For this reason, we expect to rule out all influences on the mechanical properties except the cellular architecture.

Before compression testing, the RP parts were mounted between two parallel steel plates. Using a Zwick universal tensile test machine, the samples were loaded in compression and stress and strain were recorded. Typically five tests with a strain rate of 5 mm per minute were performed with each type of structure. In order to determine the bulk material properties, individual struts were tested under compression and the value for  $E_S$  was determined to be  $E_S = 2.5 \pm 0.3 \text{ GPa}$ .

The results of the compression tests were analysed to gain three parameters: The maximum stress was defined as the maximum force divided by the footprint of the structures ( $\sigma^*$ ). The stiffness was defined as the slope of the stress-strain-curve in the initial linear range ( $E^*$ ). The energy absorption efficiency ( $EAE^*$ ) was calculated as the

ratio between the rectangle in Fig. 8.3 (sc) and the respective area under the stress-strain-curve. The area of the rectangle corresponds to the energy absorption of an ideal plastic material. The cut-off value for the strain delimiting the above two areas was determined by the complete collapse of one layer and the onset of the collapse of the next layer [8.24].

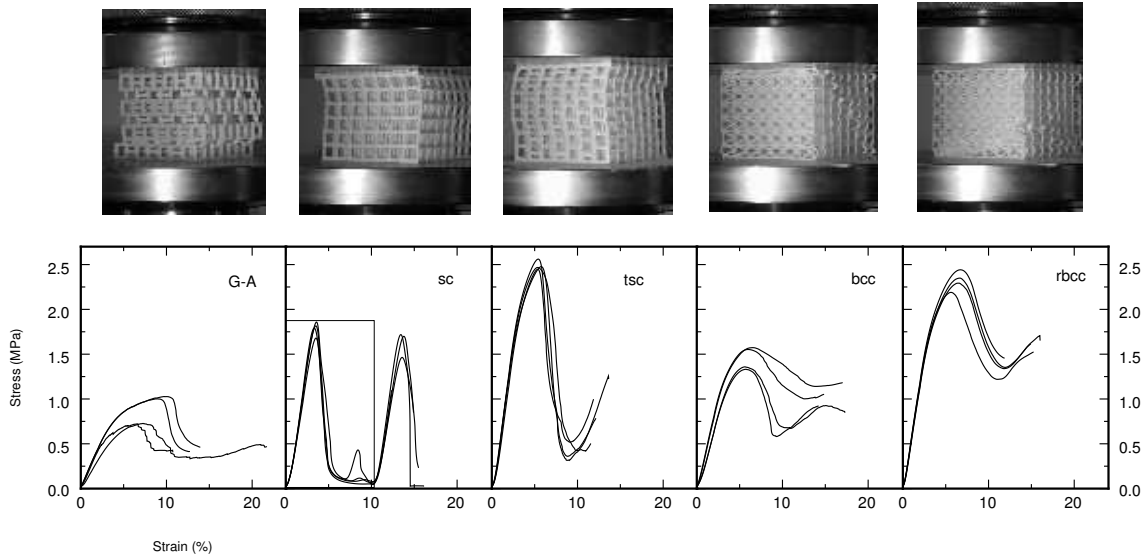


**Figure 8.3:** stress strain curves and pictures of the deformed structures

Fig. 8.3 shows typical stress-strain curves for the five structures. Clearly  $\sigma^*$  and  $E^*$  were smallest for the G-A-structure. The maximum of the curve, that is  $\sigma^*$ , was largest for the tsc and rbcc structures. The maximum stiffness was found for the tsc and the sc structures, followed by the rbcc structure. The  $EAE^*$  is highest, at about 0.75 for the G-A-structure, the bcc and the rbcc structure.

It is no surprise that the G-A-structure has the lowest  $\sigma^*$  and  $E^*$ , since all struts are loaded in bending rather than compression. It fails by the bending and breaking of struts oriented perpendicular to the load direction. At the beginning of failure, individual struts break at random positions within the structure, until the damage is localized within one single "layer".

The simple cubic structure (sc structure) fails by collective buckling of the vertical struts in one layer oriented perpendicular to the load direction. The struts are breaking at the knots (see fig. 8.3). The collapse of one layer reduces the force for further compression to almost zero. After densification of the layer, the force rises again until the struts of another layer start to bend, as already seen in previous work [8.2].

In order to decrease the effective length of the vertical struts, a translated simple cubic structure (tsc structure) was designed. In the tsc structure, the struts in load direction were kept unchanged compared to the simple cubic structure. But neighbouring unit cells were translated vertically by half the "lattice constant". As can be seen from Fig. 8.4, this decreases the localisation of deformation and failure occurs at larger loads.

A body centered cubic structure was obtained by reinforcing the simple cubic structure

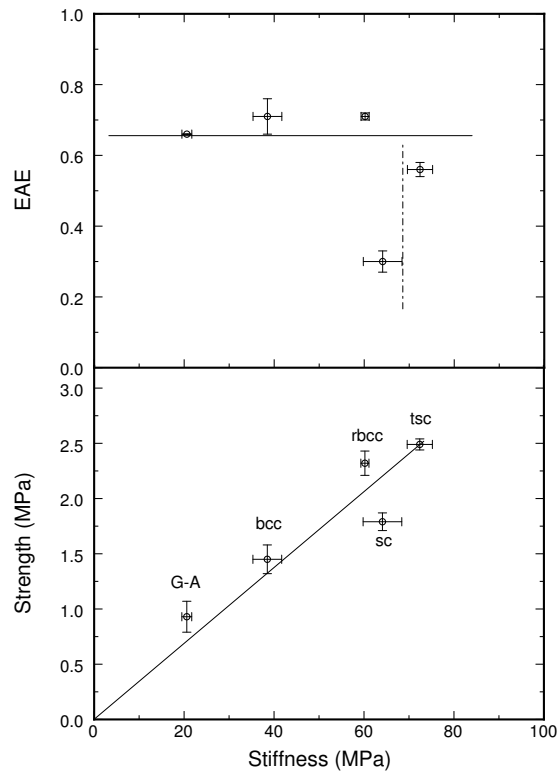


**Figure 8.4:** Energy absorption efficiency and strength versus stiffness. The straight lines in the upper diagram are just guides to the eye, in the lower diagram, the line is a least square fit to the data, forced to go through the origin.

with diagonal struts. In order to keep the apparent density of the structure constant, the diameter of the bcc-struts has to be smaller than the diameter of the tsc- and sc-struts. The decreased cross-section leads to a weakening of the structure, whereas the stabilization through the diagonal bracing strengthens the structure. The bcc structure fails by bending and breaking of struts within a shear plane oriented in  $45^\circ$  to the load direction, which accords to the  $[110]$  plane in cubic crystals.

The reinforced body centered cubic structure (rbcc) has additional vertical and horizontal struts (Fig. 8.2) and a larger overall cross-section of struts aligned with the load direction. However, each individual strut is even thinner than in the bcc structure. This structure fails in a way similar to the bcc structure, within a "shear plane", oriented  $\approx 60^\circ$  to the load direction, in this case.

Fig. 8.4 summarizes the results of mechanical testing. As one can see in the upper part of the figure, it was possible to design structures with more or less constant energy absorption efficiency, whose stiffnesses vary by a factor of three. On the other hand, structures with almost constant stiffness and an  $EAE^*$  ranging between 0.3 and 0.7 were also built. This shows the potential of architectural design and the necessity to take this into account when working with cellular materials, both in engineering and in biomedical research.

From the bottom diagram in Fig. 8.4 it can be seen that there is a roughly linear

correlation between stiffness and strength. This is in agreement with the predictions for open-cell foams mentioned in the introduction, namely that  $\frac{\sigma^*}{E^*} = \frac{C_4}{C_1} = \text{constant}$ . Interestingly, the ratio  $\frac{\sigma^*}{E^*}$  was predicted to be constant for varying apparent densities in random foams. We have shown here, that a similar relation describes the behaviour of a number of structures with the same apparent density but different architectures. The slope of the straight line is  $\approx 0.035$  (rather than 0.05 which corresponds to the ratio  $\frac{\sigma^*}{E^*}$  for the G-A-structure). The largest deviation from this behaviour is observed for the sc structure.

## 8.4 Discussion

Foams and regular lattice structures have been extensively studied in the past to improve the understanding of their mechanical properties. For load-bearing applications, such as a vertebra in the case of the human skeleton for example, two properties are of utmost importance. First, sufficient strength is necessary to prevent collapse of the structure. Second, when the load reaches critical values, catastrophic failure is to be avoided. Hence, some defect tolerance of the structure is required. We use the  $EAE^*$  as a rough measure for the defect tolerance. Indeed, a structure with a plateau in its stress-strain-curve has a high  $EAE^*$ . Such structures have to be relatively defect tolerant, since the formation of defects in the compression process does not lead to significant reduction of the deformation stress. The highest values for both,  $EAE^*$  and strength, are obtained for the rbcc and the tsc structure. Obviously, these two solutions are very different. The rbcc structure with its diagonal struts resembles a typical technical solution, while the tsc structure reminds the interior of vertebra (Fig. 8.1). At this stage, it is not possible to say why nature did not adopt the philosophy to use diagonal struts; this may be due to biological rather than mechanical constraints [8.19].

An important geometric parameter for defining the stiffness (and strength) of a cellular structure with given density is the connectivity [8.21]. This parameter describes the number of struts meeting in each node and it has been shown that all possible modes of deformation of the structure lead to tensile/compressive deformation (rather than bending) of the struts, if the connectivity is greater or equal 12. It is interesting to note that only one of our structures has a connectivity larger than 12 (rbcc with a connectivity of 14). Nevertheless, in our case, the struts are loaded in compression for all structures except the G-A structure, where the struts are deformed by bending. The reason is that column- like struts crossing the whole structure are parallel to the load direction and take up most of the deformation. This suggests that a vertebra does not necessarily need a connectivity larger than 12 in order to reach mostly tensile/compressive deformation in the struts, because of the typical load pattern.

In addition, the stiffness is primarily affected by number and the thickness of the columns in the load direction. Of course, diagonal struts will also contribute though to a minor degree. The total cross-section of vertical columns increases from bcc to rbcc, tsc and sc, which indeed roughly correlates with increasing stiffness of the structures.

Moreover, buckling of these columns will have a major influence on the strength of the structures. This is influenced by the effective length of the columns, that is, the distance

between two nodes. The tsc structure which was derived from the sc by reducing the effective length by a factor 2 showed a considerable increase in strength at almost identical stiffness. Moreover, the localisation of deformation in special shear planes (the horizontal plane for sc and the face diagonal for bcc) further reduces the strength of the structures and - at the same time - their energy absorption efficiency. Indeed, the structures with the best performance (tsc and rbcc) showed the least localization of deformation.

In summary, the present work has shown that strength, stiffness and energy absorption efficiency of structures with constant apparent density can be varied independently by variation of the microarchitecture. Strength and stiffness correlate with each other not only for varying apparent density but also for varying microarchitecture. The potential of microarchitectural design is huge and not nearly tapped.

## Acknowledgements

---

We are grateful to A. Ippavitz, A. Buehrig-Polaczek, D. Fischer (Univ. Leoben) and H. Pettermann, T. Daxner, S. Seidler (TU Vienna) for discussion and help with rapid prototyping technology. We gratefully acknowledge the financial support by the Austrian Science Fund (Project FWF-P15852).

## 8.5 References

---

- 8.1 L.J. Gibson and M.F. Ashby. *Cellular solids*. Cambridge University Press, second edition, 1997.
- 8.2 Y. Yamada, K. Shimojima, M. Mabuchi, M. Nakamura, T. Asahina, T. Muai, and K. Higashi. Effects of load direction on the mechanical properties of open-cellular epoxy with a cubic prism structure. *Phil. Mag. Lett.*, 80:215–220, 2000.
- 8.3 N. Hüsing and U. Schubert. *Angew. Chem. Int. Ed. Engl.*, 37:22–45, 1998.
- 8.4 D. J. Green and P. Colombo. Cellular ceramics: Intriguing structures, novel properties and innovative applications. *MRS Bulletin*, 28(4):296–300, 2003.
- 8.5 M. F. Ashby, A. G. Evans, N. A. Fleck, L. J. Gibson, J. W. Hutchinson, and J. W. Wadley. *Metal Foams: A Design Guide*. Butterworth-Heinemann, 2000.
- 8.6 J. Banhart, M. F. Ashby, and N. A. Fleck. *Cellular Metals and Metal Foaming Technology*. Verl. MIT Publ., 2001.
- 8.7 T.G. Nieh, K. Higashi, and J. Wadsworth. Effect of cell morphology on the compressive properties of open-cell aluminum foams. *Materials Science and Engineering A*, 283(1-2):105–110, 2000.
- 8.8 G. A. Rodan and T. J. Martin. Therapeutic approaches to bone diseases. *Science*, 289:1508–1514, 2000.

- 8.9 J. A. Kanis. Diagnosis of osteoporosis and assessment of fracture risk. *Lancet*, 359:1929–36, 2002.
- 8.10 C. H. Turner. *Osteoporos. Int.*, 13:97–104, 2002.
- 8.11 J.E. Aaron, P.A. Shore, R.C. Shore, M. Beneton, and J.A. Kanis. Trabecular architecture in women and men of similar bone mass with and without vertebral fracture: Ii three-dimensional histology. *Bone*, 27(2):277–282, 2000.
- 8.12 J. Wolff. Über die innere Architektur des Knochens und ihre Bedeutung für das Knochenwachstum. *Archiv patho. Anat. Physio.*, 50:389–453, 1870.
- 8.13 R. Huiskes. If bone is the answer, what is the question. *J. Anatomy*, 197:145–156, 2000.
- 8.14 P. Roschger, B.M. Grabner, S. Rinnerthaler, W. Tesch, M. Kneissel, A. Berzlanovich, K. Klaushofer, and P. Fratzl. Structural development of the mineralized tissue in the human L4 vertebral body. *Journal of Structural Biology*, 136:126–136, 2001.
- 8.15 E. W. Andrews, G. Gioux, P. Onck, and L. J. Gibson. Size effects in ductile cellular solids part ii: Experimental results. *Int. J. Mech. Sci.*, 43:701–713, 2001.
- 8.16 A.E. Markaki and T.W. Clyne. The effect of cell wall microstructure on the deformation and fracture of aluminium-based foams. *Acta Materialia*, 49(9):1677–1686, 2001.
- 8.17 J. L. Grenestedt. Influence of wavy imperfections in cell walls on elastic stiffness of cellular solids. *J. Mech. Phys. Sol.*, 46(1):29–50, 1998.
- 8.18 J H.X. Zhu, J. R. Hobdell, and A.H. Windle. Effects of cell irregularity on the elastic properties of open-cell foams. *Acta Materialia*, 48(20):4893–4900, 2000.
- 8.19 A.M. Kraynik and D.A. Reinelt. Linear elastic behavior of dry soap foams. *J. Colloid Interface Sci.*, 181(2):511–520, 1996.
- 8.20 A.E. Simone and L. J. Gibson. The effects of cell face curvature and corrugations on the stiffness and strength of metallic foams. *Acta Materialia*, 46(11):3929–3935, 1998.
- 8.21 V.S. Deshpande, M.F. Ashby, and N.A. Fleck. Foam topology bending versus stretching dominated architectures. *Acta Materialia*, 49:1035–1040, 2001.
- 8.22 A. P. Roberts and E. J. Garboczi. Elastic properties of model random three-dimensional open-cell solids. *J. Mech. Phys. Sol.*, 50(1):33–55, 2002.
- 8.23 T. Daxner, H. J. Böhm, M. Seitzberger, and F. G. Rammerstorfer. Modelling of cellular materials. In H.-P. Degischer and B. Kriszt, editors, *Handbook of Cellular Metals*, pages 245–280. Wiley-VCH, 2002.
- 8.24 C. Motz, R. Pippan, and B. Kriszt. Mechanical properties and determination. In H.-P. Degischer and B. Kriszt, editors, *Handbook of Cellular Metals*, pages 183–202. Wiley-VCH, 2002.



---

# WATER SOLUBLE, PHOTOCURABLE RESINS FOR RAPID PROTOTYPING APPLICATIONS

**J. Stampfl, A. Wöß, S. Seidler, H. Fouad, A. Pisaipan, F. Schwager, R. Liska**  
Macromolecular Symposia, in print 2004

**Abstract.** Rapid Prototyping (RP) is a suitable manufacturing method for fabricating structures with high geometric complexity and heavily undercut features. A special class of such structures which cannot easily be fabricated with traditional manufacturing methods are cellular materials [9.1].

Rapid prototyping allows the fabrication of cellular materials on a similar size scale like in natural material-structures (e.g. trabecular bone). By using appropriate moulding techniques, these structures can be fabricated out of a wide variety of materials (polymers, ceramics, composites). In this work, several RP techniques are investigated regarding their suitability for the fabrication of cellular solids. The main focus is on using digital light processing (DLP, a variant of stereolithography) in combination with gelcasting [9.2] as a moulding technique. Besides using commercial light-sensitive resins, a class of newly developed water soluble resins has been evaluated regarding its usability as sacrificial mould material. These water soluble resins are compatible with a wide range of moulding techniques and therefore offer new routes for the fabrication of complex shapes out of more advanced materials than it is possible with currently used manufacturing techniques.

## 9.1 Introduction

---

Rapid Prototyping (RP) has become a widely used tool for the fabrication and evaluation of physical prototypes during the product development cycle. RP is used since it can produce prototypes with arbitrary shapes quickly and at lower cost than traditional prototyping techniques. Recently RP has also been investigated regarding its ability to replace traditional mass manufacturing processes in applications where only one or a small number of individually shaped parts is required.

**Tab. 9.1.** Comparison of various RP processes.

	technical principle	build speed	feature resolution	compatibility with moulding techniques	ability to shape undercut features
selective laser sintering	laser sintering of powder particles	++	+	+	+++
fused deposition modelling	extrusion of thermo-plastics	+	-	+	++
wax inkjetting	inkjetting wax droplets	-	++	++	++
stereolithography (digital light projection)	photopolymerization	++	+++	+	++

Especially for biomedical applications parts have to be shaped individually, and RP has for instance been considered for shaping cellular structures which later on serve as scaffolds for tissue engineering [9.3–9.7]. If RP processes are to be used for such an application, several issues have to be considered:

- The process must be able to achieve the necessary feature resolution. In the case of cellular materials for biomedical applications the required cell size will typically range from  $20\mu\text{m}$  to  $500\mu\text{m}$ .
- Since most RP processes cannot shape advanced materials directly, the desired target material has to be moulded from a RP part. The mould material must be chemically compatible with the utilized part material and the mould must be easy to remove in order to obtain the final part.
- Cellular materials exhibit a lot of undercut features and the used RP process must be able to shape such features.

In Table 9.1, several RP processes are compared regarding the above mentioned issues. Selective laser sintering (SLS) works with high build speeds and can easily shape undercut feature, but is somewhat limited regarding the achievable minimum feature size. Fused deposition modeling (FDM) extrudes wires with a thickness of around 0,25mm, smaller features (which might be necessary for the envisaged application) are hard to achieve. Wax inkjetting (e.g. the Modelmaker systems offered by Solidscape) uses wax materials which are compatible with most moulding techniques. If a two material system (support and build material) is used, overhanging structures can easily be built. Furthermore a good feature resolution can be achieved. The main problem with

these systems is the fact, that two-material systems use only one inkjetting-nozzle per material, thus the build time for parts with complex shapes is extremely long. Stereolithography (SLA) offers excellent feature resolution and high build speed.

Most cellular structures (see Figure 9.1) can be shaped without using support structures which have to be removed mechanically. Problems might occur if moulding techniques are to be used which do not allow a thermal removal of the SLA mould, since commercially available SLA-resins are heavily cross-linked and therefore insoluble in most solvents.

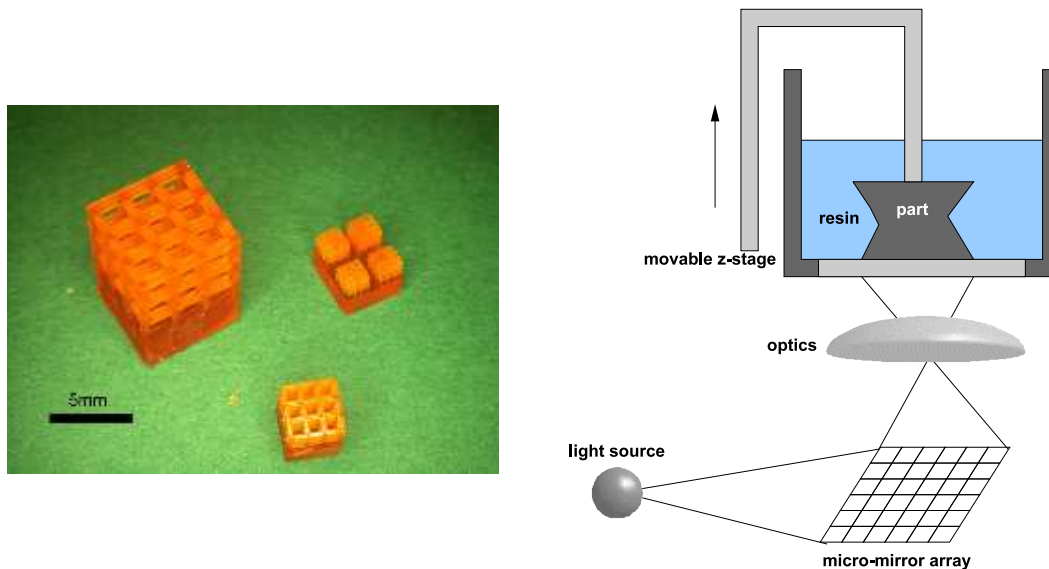


**Figure 9.1:** Cellular structures fabricated by digital light projection (left) and working principle (right) of the utilized machine.

## 9.2 Moulding techniques

Nevertheless, SLA seems to fulfil most of the criteria defined in Table 9.1, and therefore SLA and its variant digital light projection (DLP) are used in the following as primary shaping process (see Figure 9.1). Using the DLP moulds depicted in Figure 2, it is possible to fabricate ceramic parts using gelcasting. For this process the polymeric mould is filled with a ceramic slurry. The slurry contains monomers which start to polymerise after an initiator has been added. The slurry solidifies and the mould can be removed by thermal decomposition in order to obtain a ceramic green/brown part. After sintering, the final ceramic part is obtained (see Figure 9.2, right image). DLP (respectively SLA) is therefore a suitable method for the fabrication of cellular structure out of bioceramic materials. Nevertheless, the hydroxyapatite (HAP) structures shown in Figure 9.2 are not ideal for various biomedical applications due to two reasons:

- The HAP material is very brittle and mechanically weak. Therefore such structures are not suitable in applications where the structure is exposed to mechanical loads.

- During sintering, the HAP bioceramic will loose water and carbon dioxide. This change in chemical composition affects the bioresorbability of the material. Ideally, a fully bioresorbable HAP should not be exposed to temperatures that will lead to changes in the chemical composition.

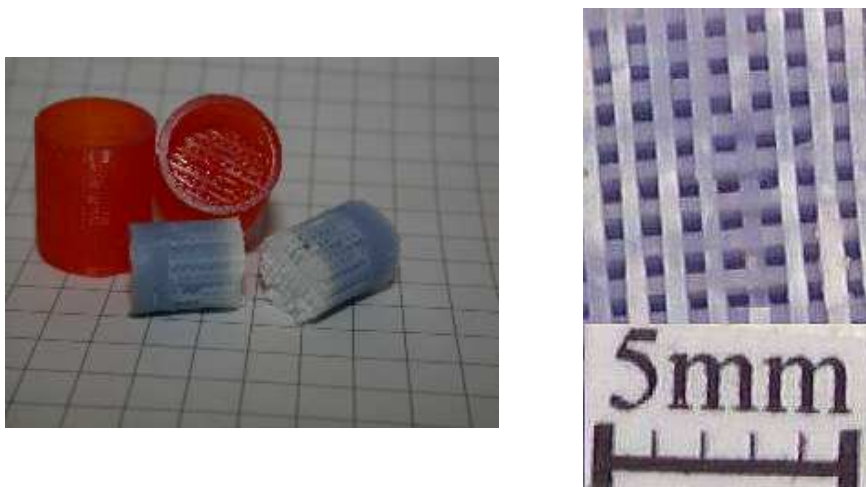


**Figure 9.2:** Mould together with gelcast HAP structures (left). Detail of sintered HAP structure (right).

### 9.3 Sacrificial photopolymers

In order to enable the fabrication of cellular structures out of advanced biomaterials using DLP moulds, a new route is proposed which is based on using soluble photopolymers. The basic principle of this technique is depicted in Figure 9.3: Using SLA (or DLP) a polymeric mould is built out of a sacrificial mould material (steps 1-3). The mould is then filled with the final part material (step 4). After the part material has solidified, the sacrificial mould is dissolved in an appropriate solvent (e.g. water) in order to obtain the final part. This type of process allows the fabrication of polymeric, composite or ceramic cellular materials using widely available lithographic techniques like SLA or DLP. Since commercially available resins are insoluble, this route is only viable if new photosensitive resins can be developed

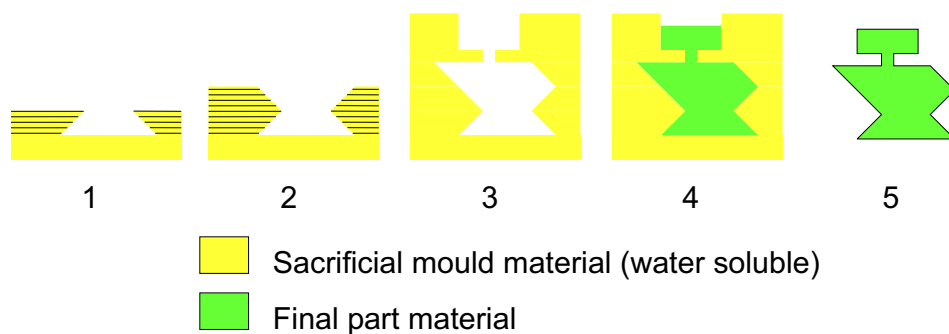


**Figure 9.3:** Proposed strategy for building parts with sacrificial photopolymers.

Water-soluble polymers [9.8] as sacrificial structures are easily accessible by photopolymerization of a wide range of commercially available monomers such as acrylic acid, methacrylic acid, acrylamide, dimethyl-acrylamide, dimethylaminoethyl methacrylate, vinylpyrrolidone etc. Important criteria for the selection of a suitable resin formulation are:

- Physical properties (solubility, viscosity) of the monomer
- Reactivity of the monomer
- Shrinkage during polymerization and
- Mechanical properties and solubility of the polymer.

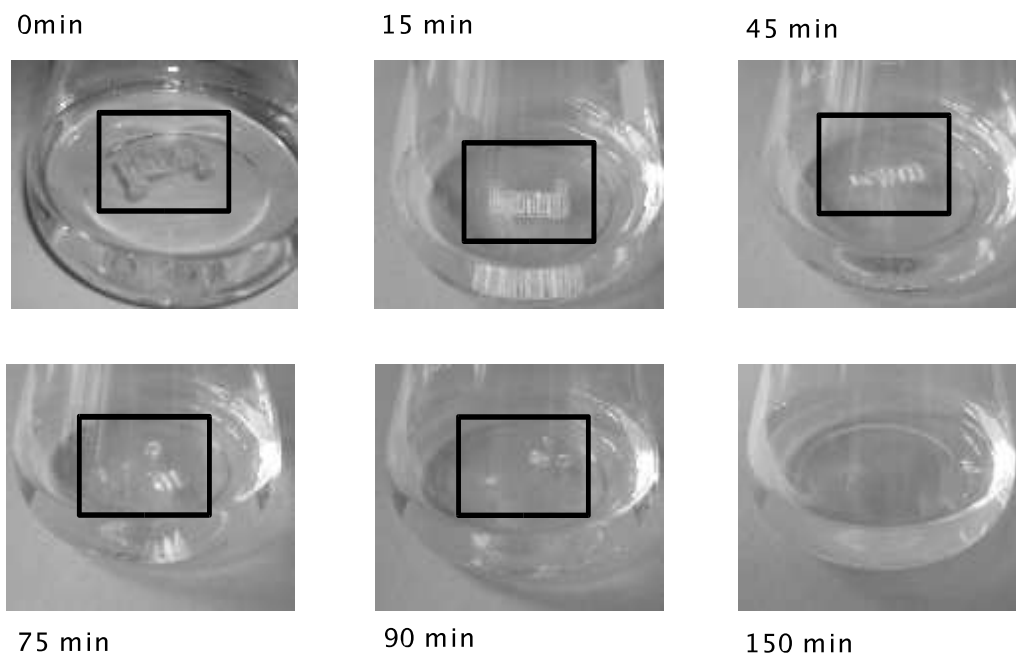


**Figure 9.4:** Dissolution of test structure in alkaline solution (1N NaOH) at 50°C.

The investigated resins were made up by the following constituents in order to fulfill the above requirements:

- Base monomer
- Co-monomer
- Filler
- Photoinitiator and
- Crosslinking agents.

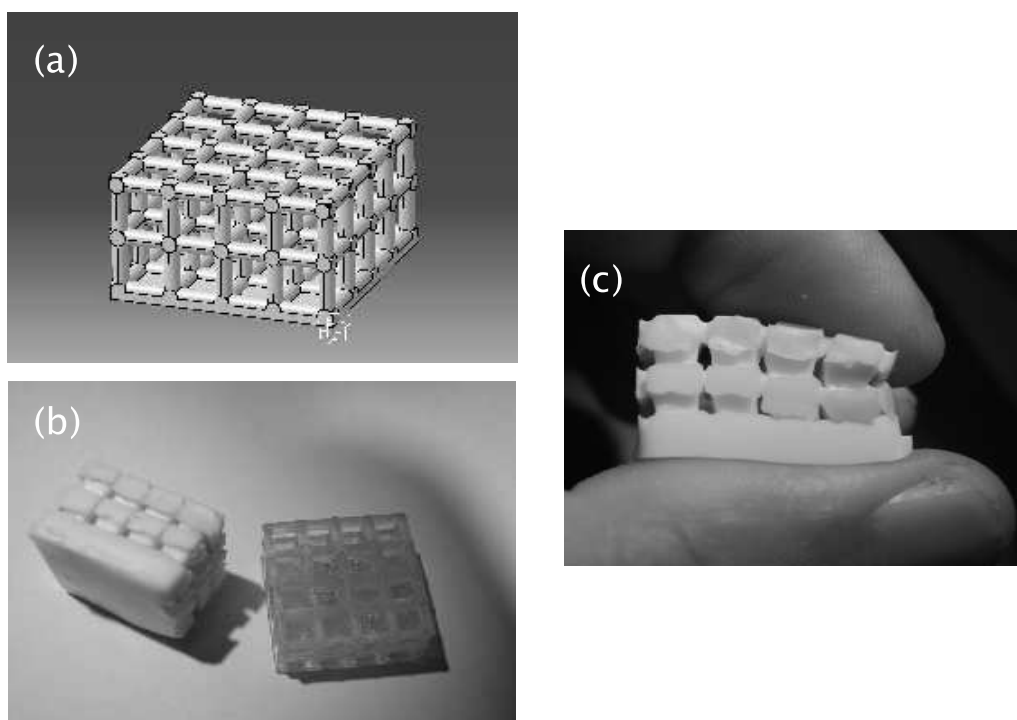


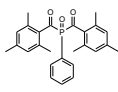
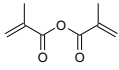
**Figure 9.5:** Cellular test structure made of water soluble photopolymer (left) together with moulded silicone structure (right).

Using these type of formulations, it is possible to fabricate structures with DLP which are soluble enough to be dissolved in alkaline solutions at slightly elevated temperatures (see Figure 9.4).

Several issues (see Table 9.2) have to be considered in order to find the optimal formulation using the above mentioned constituents: The photoinitiator, which is responsible for the initiation of the polymerization process, has to produce radicals with high efficiency and high reactivity towards unsaturated compounds. By photo-DSC experiments, bisacylphosphine oxide (BPO) was found to fulfil these requirements. Besides good solubility, the DLP process requires that the photoinitiator absorbs light in the visible range of the spectrum.

To keep build times as short as possible, the base monomer should be highly reactive as found for acrylate based monomers such as dimethyl-acrylamide (DMAA). In addition, the solubility of the polymer is of prime importance which is varied by the utilized base monomer and the degree of cross-linking. Using anhydride based monomers such as methacrylic acid anhydride (MAA), cross-links can be easily cleaved under alkaline conditions. It has been found that these structural elements are essentially necessary to obtain sufficient feature resolution due to limited radical diffusion. Especially at the beginning of the polymerization process, the same effect is obtained by application of fillers such as polyvinylpyrrolidone (PVP). The higher the viscosity of the resin, the less diffusion of radicals can occur and the more locally confined the photopolymerization will take place. Furthermore, the polymer has to be insoluble in its own monomer. Otherwise exposed features will get dissolved and the accuracy of the process decreases. Suitable comonomers as methacrylic acid (MA) reduce this unwanted

**Tab. 9.2.** Properties of constituents.

	Photoinitiator BPO 	Base monomer DMAA 	Comonomer MA 	Filler NVP 	Crosslinking agent MAA 
Reactivity	++ excellent addition rates to double bonds	++ acrylates show highest reactivity			
Shrinkage				++	
Solubility		++ excellently soluble	++ alkaline conditions	++ excellently soluble	-- alkaline conditions necessary
Mechanical strength			++ hydrogen bonds		++ degree of crosslinking
minimum feature size	++ photo bleaching effect		++ monomer insoluble polymer	++ viscosity of the resin	++ limited radical diffusion

behaviour of base monomers like DMAA. The mechanical strength of the obtained product is defined by the degree of cross-linking and the density of hydrogen bonds in the solid polymer.

By fine-tuning these parameters, compositions can be obtained which allow the fabrication of soluble cellular structures (see Figure 9.5, left images). These structures can serve as sacrificial moulds for various thermosetting polymers (e.g. silicone, Figure 9.5, right image) which can only be obtained by using a soluble mould material. Using this route, it is therefore possible to fabricate parts with severe undercuts by utilizing SLA moulds, and the accessible material spectrum can be expanded significantly.

## 9.4 Conclusion

It could be shown that RP is a suitable method for manufacturing cellular structures with defined internal and external geometries. Using commercially available photopolymers it is possible to shape ceramic cellular structures using stereolithography and appropriate moulding techniques. By developing sacrificial, water soluble photopolymers further materials can be made accessible to fabrication techniques based on stereolithography. The photopolymers developed for this work are suitable for the fabrication of sacrificial cellular structures. By tuning the composition of these photopolymers, solubility, feature resolution and mechanical properties can be varied according to the requirements of the application.

## Acknowledgement

---

We gratefully acknowledge the financial support by the Austrian Science Fund (Project FWF-P15852) and the Hochschuljubiläumsstiftung of the City of Vienna. H.F. would like to thank the Egyptian government for financially supporting him during the progress of this work.

## 9.5 References

---

- 9.1 J. Stampfl, A. Wöß, O. Kolednik, and P. Fratzl. Object reconstruction and object construction: applications in materials science. *Recent Res. Devel. Applied Phys*, 5:89–106, 2002.
- 9.2 J. Stampfl, H.C. Liu, S.W. Nam, K. Sakamoto, H. Tsuru, S. Kang, A. G. Cooper, A. Nickel, and F. B. Prinz. Rapid prototyping and manufacturing by gelcasting of metallic and ceramic slurries. *Materials Science and Engineering A*, 334(1-2):187–192, 2002.
- 9.3 D.W. Hutmacher. Scaffold design and fabrication technologies for engineering tissues - state-of-the-art and future perspectives. *J. Biomaterials Science - polymer edition*, 12(1):107–124, 2001.
- 9.4 S.J. Hollister, R.A. Levy, T-M.G. Chu, and J.W. Halloran. Design and manufacture of an orbital floor scaffold using image processing and rapid prototyping. In *Proceedings of the 1997 Bioengineering Conference, OR*, pages 391–392. American Society of Mechanical Engineers, Bioengineering Division, 1997.
- 9.5 J. Stampfl, R. Cano Vives, S. Seidler, R. Liska, F. Schwager, H. Gruber, A. Wöß, and P. Fratzl. Rapid prototyping - a route for the fabrication of biomimetic cellular materials. In P.J. Bartolo, G. Mitchell, et al., editors, *Advanced Research in Virtual and Rapid Prototyping*, Proceedings VRAP 2003, Leiria, pages 659–666. ESTG, 2003.
- 9.6 T.-M.G. Chu, D.G. Orton, S.J. Hollister, S.E. Feinberg, and J.W. Halloran. Mechanical and in vivo performance of hydroxyapatite implants with controlled architectures. *Biomaterials*, 23(5):1283–1293, 2002.
- 9.7 K.F. Leong, C.M. Cheah, and C.K. Chua. Solid freeform fabrication of three-dimensional scaffolds for engineering replacement of tissues and organs. *Biomaterials*, 24:2363–2378, 2003.
- 9.8 P. Molyneux. *Water-Soluble Synthetic Polymers: Properties and Behaviour*. CRC Press, Boca Raton, Florida, 1983.

3DP	three dimensional printing
ABS	acrylonitrile butadiene styrene
ACR	Advanced Ceramics Research
ASTM	American Society for Testing and Materials
CAD	computer aided design
COA	crack opening angle
COD	crack opening displacemnet
CNC	computer numerical control
CT	compact tension
CTOA	crack tip opening angle
CTOD	crack tip opening displacemnet
DCB	double cantilever beam
DEM	digital elevation model
DLP	digital light processing
DLS	direct laser sintering
DNA	deoxyribonucleic Acid
EBS	electron backscatter diffraction
EDM	electro discharge machining
ESIS	European Structural Integrity Society
FDM	fused deposition modelling
gy	general yielding
HA	hydroxy apatite
LCD	liquid crystal display
LIGA	Lithographie Galvanoformung Abformung
LOM	laminated object manufacturing
lsy	large scale yielding
MEMS	micro electro-mechanical systems
MJM	multi jet modelling
OIM	orientation imaging microscopy
PA	polyamide
PCL	poly( $\epsilon$ -caprolactone)
PDMS	poly(dimethyl siloxane)
PE	polyethylene
PET	poly(ethylene terephthalate)
PLA	polylactic acid

PMMA	poly (methylnathacrylate), plexiglass
PP	polypropylene
PTFE	poly(tetrafluoroethylene)
PVC	poly(vinyl chloride)
RIE	reactive ion etching
RM	rapid manufacturing
RP	rapid prototyping
SDM	shape deposition manufacturing
SEM	scanning electron microscope
SFF	solid freeform fabrication
SL	stereolithography
SLA	stereolithography apparatus
SLM	selective laser melting
SLS	selective laser sintering
SRI	Stanford Research Institute
ssy	small scale yielding
TCP	tricalcium phosphate

# Index

- 3D printing, 30–31, 52
- 3D shaping, 15–41
- 3D-scanning, 2, 7–14
  - in fracture mechanics, 10
- 3DP, *see* 3D printing
- ABS, 32
- absorption, 23
- amorphous metal, 89, 90
- ASTM, 66
- austenite, 65
- batch rate, 40
- biocompatible, 49, 50
- biodegradable, 50
- bioglass, 50
- bioresorbable, 50
- blunting, 59, 64, 68, 69, 73
- bone, 48
  - cancellous, 113
- buckling, 114
- build speed, 39
- capital cost, 41
- cellular materials, 3, 47
- cellular solids, 113
- ceramics, 24, 35, 48–50
  - mechanical properties, 108
- chitin, 50
- chitosan, 50
- chondrocytes, 51
- COA, *see* crack opening angle
- coalescence, 64
- COD, *see* crack opening displacement
- collagene, 50
- compact, 35
- composites, 48
- confocal scanning microscopy, 7
- copper, 92
- cork, 48
- corresponding fracture surfaces, 59, 63
- cost estimate, 40
- crack extension, 64, 66, 73
- crack growth resistance, 59–61, 64, 73, 77
- crack opening angle, 65, 80
- crack opening displacement, 10, 80
- crack tip, 62–64
- crosslinking
  - agent, 129
- CT specimen, 59, 61, 63, 65, 69, 82
- diffusion, 95
- digital elevation model, 9, 76, 77, 79
- digital image analysis, 65
- digital light processing, 19
- digital mirror devices, 19
- digital photogrammetry, 76
- dimensional change, 28
- dimethyl-acrylamide, 129
- dimple, 10, 63, 64, 76
  - cross section, 76
- double cantilever beam, 70
- dynamic mask, 19
- EDM, *see* electro discharge machining
- elastic plastic, 62
- elastomer, 32
- electro discharge machining, 89
- electroplating, 3, 89, 92
- energy absorption efficiency, 118
- energy dissipation rate, 59
- ESIS, 66
- eutecticum, 95
- extrusion, 32
- FDM, *see* fused deposition modeling
- feature resolution, 24, 47
- femtosecond laser, 22
- ferite, 65
- ferrite, 72
- flaking, 104
- flashing, 38
- foam

- open cell, 114
- foaming agent, 47
- fracture energy, 10, 59–87
- fracture initiation, 64, 65, 67
- fracture surface, 59
  - corresponding, 77
- fracture surface analysis, 72
- fracture toughness, 10
- fused deposition modeling, 31–32
- fused deposition modelling, 48
  
- Gaussian intensity profile, 22
- gelcasting, 101–111
- general yielding, 60
- glass transition temperature, 25
- green part, 101
  
- heat tinted, 73
- heat-tinted, 68
- homologue point, 8
- honeycomb, 114
- hot-pressing, 89, 93
- hydroxyapatite, 50
  
- image processing, 2, 8
- imperfection, 114
- infiltration, 28
- injection molding, 38
- inkjet printing, 30
- internal stress, 37
- investment casting, 38
  - with stereolithography, 18
  
- J-integral, 64, 66, 67, 70
  
- laminated object manufacturing, 36
- large-scale yielding, 60
- laser sintering
  - direct, 28
- layered manufacturing, 15
- LIGA, 90
- liquid crystal, 25
- load line displacement, 69
- localisation, 117
  
- magnetic field, 25
- material-structures, 48
- MEMS, 18, 89
- micro-stereolithography, 47
- microstructure, 65
  - ceramic, 105
- MJM, *see* multi jet modeling
- mold
  - micromachined, 106
- Mold SDM, 33, 101–111
- molding, 37
- moulding, 3
- multi-specimen, 68, 71
- multiple hierarchies, 47
  
- optoelectronics, 47
- Orientation image microscopy , 11
- osteoblasts, 51
- osteoporosis, 114
- overhead, 40
  
- PA, *see* polyamide
- parallax, 8
- parting line, 38
- PET, *see* poly(ethylene terephthalate)
- photoinitiator, 129
- photonic crystals, 47
- photopolymer
  - soluble, 129
- photoresist, 91
- PLA, *see* polylactic acid
- plain sided, 72, 74
- plain-sided, 59, 62, 67, 69
- plasma etcher, 89
- plasma etching, 106
- plastic deformation, 10, 62, 77
- plastic strain energy, 64
- plastic zone, 60, 72
- poly(ethylene terephthalate), 49
- poly(p-dioxanone), 50
- poly(tetrafluoroethylene), 49
- polyamide, 49, 116
- polyanhydride, 50
- polycarbonate, 32
- polyglycolide, 50
- polylactic acid, 50
- polymeric binder, 30
- polymerization, 104
  - shrinkage, 129
- polymers, 48
- polypeptide, 50
- powder
  - gas atomized, 104
- PTFE, *see* poly(tetrafluoroethylene)

- QuickCast, 18
- rapid manufacturing, 38, 101  
cost model, 40
- rapid prototyping, 101, 113  
material cost, 39  
of cellular materials, 47  
processes, 3, 16  
system cost, 39  
system selection, 37  
versus injection molding, 40
- reactive ion etching, 91
- resin  
water soluble, 3
- reverse engineering, 7
- RM, *see* rapid manufacturing
- Robocasting, 47
- RP, *see* rapid prototyping
- scaffold, 51
- scallops, 109
- scanning electron microscope, 65, 73, 76
- scanning electron microscopy, 2, 7  
stereoscopic, 7
- scanning probe microscopy, 7
- SDM, *see* shape deposition manufacturing
- selective laser sintering, 25–29, 48, 115  
materials, 27
- SEM, *see* scanning electron microscope
- shape deposition manufacturing, 33
- shear lip, 61, 64, 71–73, 83
- side-grooved, 59, 62, 65, 68
- silicon, 89
- silicon nitride, 101
- silicone, 49
- single specimen test, 66
- sintering, 102
- SLA, *see* stereolithography
- SLS, *see* selective laser sintering
- slurry  
ceramic, 104
- small scale yielding, 62
- solid loading, 24
- specimen thickness, 69
- spongiosa, 51
- stainless steel, 49
- starch, 30
- steel  
bainitic, 63  
duplex, 59, 65, 66, 77, 82  
maraging, 59, 63, 65, 78, 82  
mild, 72  
precipitation hardening, 104  
stainless, 101
- stereolithography, 3, 15–25  
borders, 16  
ceramics, 24  
elastomer, 24  
hatches, 16  
layer thickness, 15  
liquid crystal, 25  
materials, 23  
microsystems, 18  
molding, 17  
pixel arrays, 19  
principle, 17  
secondary processes, 17  
shrinkage, 18  
spot size, 21  
two-photon systems, 22
- stereophotogram, 59, 65
- stereophotogrammetry, 10, 76
- strain hardening, 65
- stretched zone, 72, 77
- striation, 10
- structural component, 60
- support material, 31, 102
- surface finish, 28, 37
- surface quality, 38
- surface roughness, 106
- syringe, 49
- system cost, 39
- system selection, 37
- thermal expansion, 25
- thermo-mechanical properties, 25
- Three-dimensional printing, *see* 3D printing
- titanium, 49, 52
- tolerance range, 38
- tooling, 3
- topography, 2, 10, 61, 65, 76, 77
- topology, 114
- trabecular bone, 51
- transferability, 60, 61, 83

tricalcium phosphate, 50  
turbine, 107  
two-photon lithography, 22, 47  
  
undercut, 47  
  
vertebra, 51, 115  
vertebral body replacement, 52  
viscosity, 30  
void, 64, 72, 77  
void map, 77  
  
wax, 101  
    water soluble, 31  
white-light-interference microscopy, 7  
Wolff-Roux-law, 114  
wood, 48, 113  
  
zirconia, 49